CARRIER-LO PHONON INTERACTIONS IN SI(001)

by

Anca-Monia Constantinescu

BS in Physics, University of Bucharest, Bucharest, 1997

MS, University of Pittsburgh, Pittsburgh, 2007

Submitted to the Graduate Faculty of

Art and sciences in partial fulfillment

of the requirements for the degree of

PhD in Physics

UNIVERSITY OF PITTSBURGH

SCHOOL OF ART AND SCIENCES

This dissertation was presented

by

Anca-Monia Constantinescu

It was defended on

July 29, 2010

and approved by

Hrvoje Petek, Professor, Department of Physics and Astronomy

David Snoke, Professor, Department of Physics and Astronomy

David Jasnow, Professor, Department of Physics and Astronomy

Jeremy Levy, Professor, Department of Physics and Astronomy

Hong Koo Kim, Professor, Department of Electrical Engineering

Dissertation Advisor: Hrvoje Petek, Professor, Department of Physics and Astronomy

Carrier-LO phonon interactions in Si(001)

Anca-Monia Constantinescu, PhD

University of Pittsburgh, 2010

We present a study of the interaction between high density photoexcited carriers and coherent LO phonons in Si(001). Through high-density (10^{19}–10^{20} carriers/cm^3) photoexcitation of Si(001) near its E_1 critical point with 10 fs duration, 400 nm laser pulses, the zone-center coherent LO ($q \approx 0$) phonon is excited. The coherent LO phonon gains a complex self-energy (i.e., frequency shift and contribution to decay rate) by interacting with the photogenerated non-equilibrium electron-hole plasma through the deformation potential interaction mechanism. We measure the time dependent renormalization of the LO phonon frequency and dephasing time by analyzing the anisotropic transient reflectivity of variously doped Si samples over a delay time of 6 ps between pump and probe pulses. We study how both these quantities depend on the initial photoexcited carrier density, and the level and type of doping. We further study the LO phonon excitation and detection mechanism monitoring the LO phonon amplitude change with the pump and probe polarizations orientations with respect to Si sample crystalline axes. The phonon amplitude exhibits a $\sin(2\theta)$ dependence on either the pump or the probe polarization angular rotation, where θ is the angles between the pulse electric field polarization and the [110] axis of the sample in both cases. This result is consistent both with the $\Gamma_{25'}$ symmetry and the deformation potential mechanism excitation of the LO phonon of Si. We also measure the dependence of the coherent LO phonon on the excitation light wavelength. We find that the phase does not fit into the theoretical picture developed to date for the coherent LO phonon

generation. Moreover, the Fourier Transforms of the time-domain signals show Fano-like profiles for the LO phonon peak, with the asymmetry strongly dependent on the excitation wavelength. The wavelength dependence of both the phase and the LO phonon lineshape suggest that the mechanism for the LO coherent phonon generation should be described by a model where the generation pathways via the Raman process and the carrier excitation are coupled through the deformation potential interaction.

TABLE OF CONTENTS

LIST OF TABLES

LIST OF FIGURES

PREFACE

The road I walked during completion of this work was neither smooth, nor straightforward. It was a unique journey, and now, two weeks after my defense seminar, I believe it was worth having…. Many people crossed my path during my studies and I learned lots from everyone about both physics and human nature.

I was lucky to have in my graduate committee thoroughly professional and knowledgeable professors, all ready to help when I needed rescuing. I thank them all and wish them all the best!

My admiration and respect for my adviser Dr. Hrvoje Petek, for his incredible passion for science and effectiveness. I wish I had the time and wisdom to learn from him even more than I did. I acknowledge and appreciate the extent of his efforts and I thank him for all the help.

A special place in my life as a grad student is reserved to Dr. David Snoke, who not only took the time to co-advise me while Dr. Petek was in his sabbatical year, but was always available to read my drafts and discuss any problem I encountered, with patience and insight. That was a great help when I needed it the most, and I will never forget it.

I thank a great deal Dr. David Jasnow for the thorough examination of the theoretical part of my thesis, and the time he spent on the whole thesis at the end of my journey. My heartfelt appreciation to him!

One person I hold dear to me is our graduate secretary, Leyla Hirschfeld, for her goodwill, inexhaustible energy, and ability to disentangle one from trouble efficiently and fast.

The postdocs passing through our lab... Hase-san with his limitless patience while explaining concepts or doing experiments, and his “Please, Monia, take a break” each time I started fidgeting around the set-up! Atsushi and Aimo with their upbeat presence, helpful and precise like no others. Jin and Min, for whom I have no words to describe how luminous they are. My school time would have missed salt and pepper without them all.

My fellow grad students… I enjoyed meeting them all, and I reserve the most appreciation for (Dr.) Bin Zhang, for helping me with the programming and being a great friend.

My friends and people outside the school… it would be too long of a list. Well… They say people come into (and go from) one’s life for a reason or a season. I am awfully grateful to all my friends that were there for me while the rain was pouring down, and I wish the others all the best, for I appreciate the value of friendship regardless of being given for whatever reason, plain goodwill, a season or forever.

The last, but the most, I thank my mother for the great amount of time and energy she always invested in me, and especially during my PhD saga. She is the first on my list, as my father was as well, and all the good in me is primarily the result of their love. To them I dedicate this work,

Monia

Success in life consists of going from one mistake to the next without losing your enthusiasm.

Winston Churchill

1.0 INTRODUCTION

1.1 MOTIVATION

In this thesis we study the coupling between photoexcited high carrier densities and coherent longitudinal-optical (LO) zone-center ($q \approx 0$) phonons of Si(001) in an ultrafast regime. The coupling between electronic and ionic motions is referred to as "carrier-phonon interaction". Optical phonon interactions with free carriers mediate the energy redistribution within a solid, affecting the electrical and optical properties of semiconductors. Understanding the interaction between carriers and phonons on very short scale times is therefore motivated, besides by fundamental scientific interest, by the need for faster response, smaller size and lower power consumption of microelectronic devices. These features require solid knowledge of dynamics associated with the interactions of carriers and lattice vibrations (phonons), especially when devices approach the nanometer-scale range. As the device dimensions shrink to tens of nm, the electronic transit times shorten to tens of femtoseconds, and the effect of phonons is like that of strains on the lattice, modifying the mobility of carriers. Also, at high carrier densities, the coupling between optical phonons and hot electrons is crucial in connection with lattice instabilities including structural phase transitions, chemical reactions, etc.

Silicon is a widely used semiconducting material in electronic and optoelectronic devices (photon detectors, optical waveguides, optical switches, etc.) [1-6]. Recently, silicon lasers and

light emitting diodes based on silicon have been under development. Although Si is one of the most well-known materials with respect to its physical and electronic properties, the change of its optical and electronic properties under intense light excitation on time scales of the fundamental scattering processes has been hardly explored by methods of ultrafast optical spectroscopy.

Ultrafast changes in crystal and molecular structures are events that happen on femtosecond (10^{-15} sec) to picosecond (10^{-12} sec) time scales. Therefore, to create and access non-equilibrium states of the matter one needs extremely fast time resolution, and ultrashort pulses to stimulate electronic excitations. For example, to generate LO coherent phonons of Si one needs a light pulse with duration shorter than its 64 fs oscillation period [7].

Sub-10 fs laser sources are now available to both excite coherent vibrations of solids or molecules, and to investigate their relaxation with fs time resolution. On femtosecond time scale one has to resort to pump-and-probe techniques for stroboscopic measurements of light induced processes through selected optical properties of the sample [8]. This method requires two pulses of the same or different color; the "pump" pulse prepares a non-equilibrium state of the system and the delayed "probe" pulse monitors its change in time. The pulses can be in the optical regime[9], or laser pulses can be combined with and trigger THz [10-13], coherent or incoherent X-ray [14, 15], electron[16], etc. pulses. The probe pulse emerges from the sample by reflection, transmission, diffraction, or it can be converted to the second harmonic frequency, with its intensity changed according to the modifications in the optical properties of the sample induced by the pump. The change in the probe intensity is measured using various light detectors.

A sequence of pump-probe pulses for a series of delay times can be used to map out the temporal evolution of various processes such as atomic motion, phase transitions, expansion of

hot plasmas, and chemical reactions. They give a glimpse of the state of the system at each chosen delay time, much like a series of images comprise a movie.

The experiments involved in this work are performed using the pump-and-probe technique in reflection geometry, with the pump and probe derived by splitting a single pulse into an intense and a weaker replicas. The intense pulse excites high density carrier population and produces displacements of the adjacent (001) sublatices of Si, which start vibrating against each other as oscillation of the coherent zone-center LO phonon. The LO phonon vibration is selected through the choice of sample surface and exciting light polarization orientations, and light incident direction with respect to the crystalline structure of Si. The ultrafast pump excitation perturbs the lattice modifying its band structure and, therefore, its optical properties. We measure the transient reflectivity of silicon during the first ~6 ps after being electronically excited near its direct band gap. The interaction between the photoexcited carrier populations and the coherent LO phonon modifies the properties of the two subsystems. Through the interaction with the photoexcited carriers through the deformation potential phonons acquire the complex "self-energy", with the real part modifying the phonon frequency and the imaginary part contributing to the phonon dephasing rate. The dynamic changes in the LO phonon self-energy as deduced from the time dependent optical properties of the sample reveal time dependent interactions between the non-equilibrium electron-hole plasma and the crystalline lattice. The previous spectroscopic and dynamics studies related to those changes, done on Si and other materials, both theoretical and experimental, permits us to link the changes we observe in the reflectivity to the changes induced into the lattice structure by the light pulses (Section 1.3).

It has been postulated that electronic excitation with intense fs laser pulses can induce disorder by weakening the lattice bonds through the removal of a critical ~10% of valence electrons. Although the ultrafast optical excitation in our experiments is not sufficiently intense to destabilize the lattice and thereby initiate phase transitions, the conditions we create precede the necessary conditions for inducing non-thermal melting [17, 18].

Through the work presented in this thesis we hope to gain a better insight into the interaction between carriers and zone-center LO phonons of Si in the first few picoseconds after excitation.

1.1.1 Organization of the thesis

In the next section of Chapter 1 are presented succinctly the fundamental structural, mechanical, electronic, and optical properties of Si, i.e. its crystalline structure, phonon dispersion, electronic band structure, and absorption spectra. In Chapter 2 are reviewed the many-body processes occurring in semiconductors during and after short pulse optical excitation. We will introduce the optical phonon of Si in both the context of Raman scattering and coherent LO phonon excitation, explain the interaction mechanism between phonons and hot carriers, and review processes that cause the LO phonon self-energy to change. In Chapter 3, we will describe the experimental set-up, the transient reflectivity pump-and-probe measurements and data analysis procedures. In Chapter 4 are presented the experiments performed during the course of this research and the results obtained. In order to explain the results of Chapter 4, the coupled carrier and heat diffusion equations are described and numerically solved in the specific case pertaining to our

measurements. The equations used and our numerical results are presented in Chapter 5. Finally, Chapter 6 comprises the summary and conclusions of this work.

1.2 FUNDAMENTALS OF SI

1.2.1 Si crystalline structure

Si is a group IV semiconductor belonging to the cubic system. It crystallizes in the diamond structure, which is a degenerate form of zinc-blende with identical atoms at both sites in its primitive unit cell. The diamond structure is obtained by superimposing two fcc structures shifted with respect to each other by $1/4$ of the principal diagonal [111] of the cube. The primitive unit cell of Si contains 2 atoms at positions $(0,0,0)$ and $(a/4, a/4, a/4)$, where the lattice constant $a = 5.43$ Å represents the dimension of the symmetric unit cell of the lattice. Each atom has a tetrahedral covalent bond arrangement with 4 nearest neighbors, sharing 4 valence electrons in sp^3 hybridized orbitals. The diamond structure possesses inversion symmetry, unlike the zinc-blende structure (GaAs, group III-V) which does not.

To relate the motion of delocalized electrons to their possible energies in the crystal, a reciprocal space defined by quasimomentum $k = 2\pi/\lambda$, λ being the electron wavelength, is more suitable than the coordinate space. The electrons move in the periodic potential of the crystal and their allowed energies vary periodically in *k*-space; therefore, in order to describe the energy-momentum dispersion of electrons, it is sufficient to consider the band-structure corresponding to the first Brillouin zone.

In Fig. 1.1 is presented the energy-momentum dispersion for the low energy occupied (valence) and unoccupied (conduction) bands of Si.

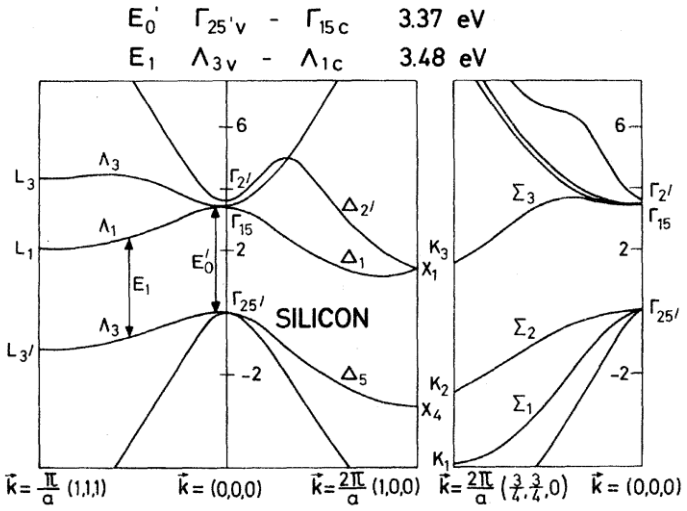

Figure 1: Band structure of Si, showing the first Brillouine zone, from Ref. [19]. Note the direct E_1 and $E_{0'}$ band gaps.

The valence bands, which are bonding in nature, are separated from the anti-bonding conduction bands by the band-gap energy. Because the conduction band minimum (CBM) and valance band maximum (VBM) possess different crystal momentum, an optical transition (electron hole pair generation or recombination) involving absorption or emission of a photon does not conserve momentum in the dipole approximation, unless is joined by a simultaneous absorption or emission of a phonon to conserve momentum; therefore Si is an indirect band gap semiconductor. In terms of perturbation theory, this transition is a second-order process and therefore has a smaller probability than an allowed first-order process such as in a direct band gap semiconductor. The VBM is located at the Γ point, i.e. center of the Brillouin Zone. The valence band (VB) is composed of degenerate heavy- and light-hole bands (*hh*, respectively *lh*) and a split-off (*so*) band. The *so* band is lowered with respect to *hh* and *lh* bands due to spin-orbit

interactions. The CB has six fold degenerate minima that are located along Γ- X lines, i.e. the [100] and the equivalent crystallographic directions, at about $k = 0.85(2\pi/a)$ from the Γ point.

1.2.2 The basics of phonons

Atoms inside a crystalline lattice do not have fixed positions in space; rather they continuously vibrate around their equilibrium positions with amplitudes that increase as the lattice temperature increases. As demanded by QM, zero-point oscillations persist even at $T = 0$ K. The vibrational motion of atoms can be seen as the motion of a system of coupled harmonic oscillators. This motion propagates in a wave-like fashion through a crystal, as a collective quasi-particle called a "phonon", which represents a quantum of the crystalline lattice vibration. Much like the electrons, the phonons are defined by their energy (E_{ph}) and quasi-momentum ($\vec{q}$), which are related to each other by the dispersion relations $E_{ph}(q)$. For example, for a 1D monoatomic chain of *N* atoms with lattice constant "*a"* the phonon dispersion relation has the simple form of Eq.1.1, where ω is the natural frequency of the harmonic potential of the lattice and *k* is the phonon wavenumber ($k = \frac{2n\pi}{N a}$, where $n = \pm 0, \pm 1, \pm 2, ..., \pm N$):

$$\omega_k = \sqrt{2\omega^2(1-\cos(k a))}\,. \qquad \text{Eq. 1.1}$$

In a 3D lattice, the atoms have 3 vibrational degrees-of-freedom, and the amplitude and quasi-momentum of phonons become vectorial quantities. Therefore, a polarization vector also characterizes phonons. If *N* is the number of atoms per unit cell, than there are 3*N* different vibration modes, of which 3 are acoustic and 3*N*-3 are optical. The optical modes are excited when ions from adjacent lattice sites are forced into an oscillatory motion against each other, and

can be infrared (odd parity) or Raman active (even-parity). In a crystal with inversion symmetry such as Si, the Raman tensor (defined in Section 2.2) should be invariant under the inversion operation. For the odd parity phonons both the atomic displacement and Raman tensor change sign under this transformation, and the Raman tensor vanishes when the phonon wavevector approaches zero. Therefore the odd-parity phonons are IR-active, while the even-parity ones are IR-inactive [20]. Depending on the propagation direction of the mode with respect to its polarization, phonons can be longitudinal or transverse. Longitudinal phonons have atomic displacements along the propagation of the wave, while transverse phonons have perpendicular atomic displacements. The phonons are bosons and obey the Bose-Einstein statistics. The probability of finding a phonon of angular frequency ω_k in a given state at thermal equilibrium is given by its occupation number

$$n(\omega_k) = \frac{1}{\exp\left(\frac{\hbar\omega_k}{k_B T}\right) - 1}, \qquad \text{Eq. 1.2}$$

where $\hbar$ is the reduced Planck's constant, k_B is the Boltzmann constant, and T is the lattice temperature.

1.2.3 Phonons of Si

The dispersion relation of phonons in real semiconductors is much more complicated than the relation given by Eq. 1.1. The phonon dispersion curves of Si, illustrated in Fig. 2, show the triply degenerate Raman active phonons at Γ point ($\vec{k} = 0$), with frequency $\omega_0 = 520$ cm^{-1} (i.e., 15.6 THz). They do not split into the LO (one branch) and TO (two) branches as for the polar GaAs, because in homopolar diamond-like semiconductors the long-range dipole interactions are

absent due to their cubic symmetry. By contrast, for the polar GaAs, these types of interactions lead to a splitting of the branches.

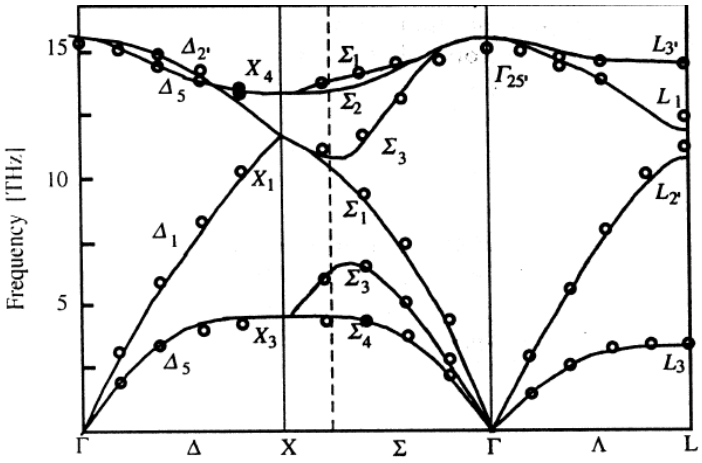

Figure 2: Phonon dispersion curves for Si, from [20].

In Si, only the presence of a strain that destroys its cubic symmetry partially lifts the degeneracy of the optical phonon (see Chapter 2). Depending on the strain symmetry, the phonon frequency can split into a singlet and a doublet with different frequencies than the Raman frequency in the absence of any perturbation.

1.2.4 Absorption in Si

For a low intensity source, incident light on a semiconductor surface is absorbed in the bulk, to the first-order, according to:

$$I(x) = I_0 \exp(-\alpha x). \qquad \text{Eq. 1.3}$$

However, for an intense laser beam absorbed in a semiconductor bulk, the intensity attenuation does not follow Eq. 1.3, but rather the more general law of attenuation:

$$\frac{dI}{dx} = -\alpha I - \beta I^2 - \gamma I^3 - ...., \qquad \text{Eq. 1.4}$$

where α is the one-photon absorption coefficient, β the two-photon absorption coefficient, γ the three-photon absorption coefficient, etc. The absorption coefficient α is defined as the ratio between energy absorbed per unit volume and time and incident energy per unit area and time. An absorption spectrum gives insight onto the strength of possible transitions for different absorbed photon energies, showing resonance peaks at what are known as critical points (i.e., regions in k-space for which the valence and conduction bands are nearly parallel, which means that many pairs of states of nearly equal *k* have a nearly equal energy difference and contribute together to the same absorption peak, i.e., regions with high joint density-of-states).

Si absorption spectra have a structure punctuated by three main features: E_0, E_1 and E_2 peaks. Those features are common to group IV and III-V semiconductors, differing mainly by the relative intensity, shape, and peak wavelength.

In Fig. 3 are shown the absorption spectra of Si measured and calculated by Cardona [21] for several temperatures (note that the absorption is measured above 2.5 eV, i.e., the E_0 feature is not shown). The 300 K spectrum is most pertinent for our experiments. Being an indirect band-gap semiconductor, the light absorption of Si below its direct band-gap of ~3.3 eV [22] occurs as a second-order process, involving emission or absorption of phonons since momentum cannot be conserved otherwise. Therefore, the absorption cross-section of Si is some orders of magnitude weaker than for a direct band-gap semiconductor (e.g., GaAs), where photons of or above the band-gap energy cause direct excitation of electrons from the VBM to CBM. The absorption coefficient is very small at the onset of the indirect band-gap at ~1.1 eV ($\Gamma_{25'} \rightarrow \Delta_1$). The feature corresponding to this energy in the absorption spectra is labeled E_0 (or E_g) and represents the fundamental absorption edge (i.e., below which there is no absorption by interband transitions). For Si, absorption occurs at E_0 only if thermal vibrations are present.

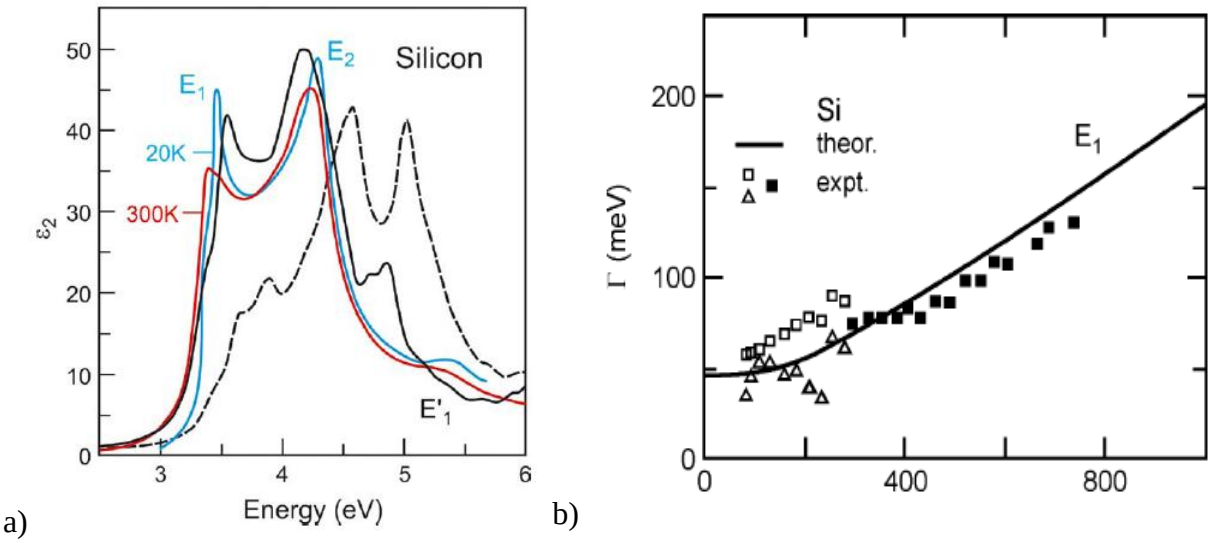

Figure 3: a) Absorption $\varepsilon_2(\omega)$ spectra of Si measured at 20 K (red) and 300 K (blue), and calculated with (continuous black) and without (dashed black) including the electron-phonon interaction; b) broadening of E_1 peak vs. lattice temperature. From [21].

As the photon energy approaches the direct band-gap value of ~3.3 eV the absorption coefficient increases and a shoulder in the absorption spectra appear. It is labeled usually by E_1, but it actually has contributions from nearly degenerate E_1 and $E_0^{'}$ (shoulder) transitions (~100 meV separation [22]; $E_1 = 3.36$ eV, $E_0^{'} = 3.41$ eV experimentally determined at 80 K [23]). E_1 corresponds to direct transitions between the near parallel VB and CB along the Γ-Λ direction (L valley), $\Lambda_1 \rightarrow \Lambda_3$ (or $L_1 \rightarrow L_{3'}$ in the notations of [24]), while the weaker $E_0^{'}$ corresponds to the $\Gamma_{25'} \rightarrow \Gamma_{15}$ transitions at Γ point. A sharp increase of absorption at 4.3 eV, labeled as E_2, corresponds to the $X_4 \rightarrow X_1$ transitions (see Fig. 2.). The last peak (not labeled in the absorption spectra), occurring at ~5.55 eV, corresponds to the $L_{3'} \rightarrow L_3$ critical point. For the photon energy of ~3.1 eV we use in our experiments we have nearly resonant transitions with E_1. Because the band structure of Si changes when there is any modification in its crystalline structure, its absorption spectra changes accordingly. The change in band structure arising from different

factors is discussed in detail in Chapter 2; presently, we just list some of those factors. It has been both measured and calculated that the absorption spectrum of Si is influenced by applied electric fields or by addition of free carriers by impurity or electrical doping [25]. The absorption coefficient is also temperature dependent. As the temperature increases, the band gap narrows and the photon energy needed for exciting electrons over the indirect band-gap decreases [26]. In Fig. 3a the absorption obtained by Cardona [21] show its change with temperature. Note that both peak position and peak broadening (Fig. 3b) are influenced by the lattice temperature. Because of the finite width and shift of the critical points with temperature, the ~3.1 eV excitation used here can be considered to involve the direct band gap excitation.

1.3 THE CONTEXT OF RESEARCH ON ULTRAFAST DYNAMICS OF SILICON

There has been substantial research on the carrier dynamics and carrier-phonon interactions in groups IV (Si, Ge) and III-V (GaAs) semiconductors. The ultrafast excitations in semiconductors are reviewed in comprehensive papers as, for example, [27]. The present work concerns the response of zone-center LO phonon to nonequilibrium photoexcited carriers as observed through its frequency and decay time, i.e. the complex self-energy associated with dressing of the phonon by electronic excitations.

Significant advances in the studies of carrier-LO phonon interaction pertaining to our research has been made through efforts of Cardona, van Driel, Dai, Riffe, and their coworkers.

During the 70's Cardona and coworkers carried out Raman spectroscopic studies of the softening of semiconductor lattice due to external and internal factors, such as the doping of carriers, applied positive uniaxial stress, and sample temperature. Simply stated, the presence of

free carriers at appropriate *k*-space sites, the positive deformation of the unit cell (tensile stress) or an increase in temperature, all produce a renormalization of the appropriate band edge energy which will affect the elastic constants by "softening" the lattice, i.e, all produce weakening of the atomic bonds and therefore a decrease of the phonon frequency. By contrast, a compressive (negative) stress produces a blue shift of the LO phonon frequency. Cerdeira and Cardona [28] measured the frequency change of both optical and acoustic phonons of Si through doping with free carriers, and found that the lattice softening is proportional to the doping density and the hole density has a greater effect than electron density on the LO zone-center phonon renormalization. Their work was supported by the finding of the same effects in other studies, including work done for space charge layers on Si [29], in which applying of a positive gate voltage to a MOS capacitor sample did not induce any observable change in the Raman spectrum, while a negative gate voltage (creating a hole space charge layer) broadened the Raman linewidth.

van Driel [30] described the dynamics of high-density plasmas (10^{21} cm^{-3}) generated by ps laser pulses of 1.17 and 2.34 eV photon energy in Si and Ge. With a model based on Boltzmann transport equations, the time-space evolutions of the carrier density *N*, carrier temperature T_{carr} and lattice temperature T_L were modeled for times up to 300 ps after excitation.

Sabbah and Riffe [31] performed time-resolved isotropic reflectivity measurements of Si with 28 fs, 800 nm pulses exciting e-h pairs across the indirect band gap of Si. They reported a momentum relaxation time of 32 fs and a carrier energy relaxation time of 269 fs. Their transient reflectivity curves show evidence of coherent phonon generation through modulation of the transient reflectivity signal at the frequency of the zone-center phonon LO. The momentum relaxation time was previously measured by Meyer et al. using a 616 nm laser pulse, who

reported a 10.6 fs momentum relaxation time constant for n-Si, whereas for the intrinsic and p-Si, a time constant of 26.5 fs [32].

In our case the initially photoexcited carrier density profile changes dynamically with the time delay, and we are able to record and measure the change in phonon self-energy for ~6 ps after the excitation. These changes show a complex interplay between the lattice softening in the presence of excited carriers at different *k*-space sites, lattice softening due to lattice temperature increase by energy transfer from the hot electrons to the lattice in their attempt to reach thermal equilibrium, and lattice electronic hardening due to electron relaxation to CBM [33].

2.0 ELECTRON-PHONON INTERACTIONS IN SEMICONDUCTORS

To provide a basis for interpretation of the results presented in Chapter 4, in this chapter we review the processes that occur in a semiconductor during and after excitation with an ultrashort laser pulse, both from a general point of view and with respect to their relevance to our particular case. The pathways of energy transfer from the laser pulse to the lattice through different channels is summarized in Fig. 4.

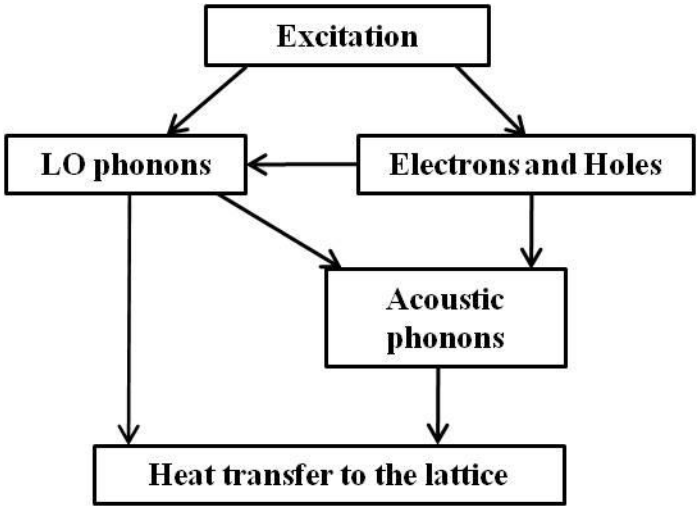

Figure 4: A schematic diagram of energy transfer pathways from photons to the carriers and lattice.

An ultrafast laser pulse impinging on a semiconductor creates high-density non-equilibrium distributions of hot carriers that perturb its lattice. By hot carriers, we refer to electrons and holes with kinetic energy much higher than lattice thermal energy $\frac{3}{2}k_B T_L$, where k_B is Boltzmann's constant and T_L is the lattice temperature. Carrier-lattice equilibrium is

restored through carrier-phonon scattering, diffusion and recombination. All of the relaxation processes start simultaneously, but their relevance is given by the time constants that define them.

Concomitantly with carrier excitation, a laser pulse can also generate coherent vibrations (i.e. in-phase motion of ions, described in Section 2.2.3) in a material, if its duration is shorter than the period of the vibration. Phonons mediate the transfer of energy between carriers and lattice, influencing the material's optical and electrical properties, as deduced in our case from the change of the frequency and decay time of the coherent LO phonons.

We therefore discuss in detail the photogeneration and subsequent dynamics of carriers and coherent phonons and review the effect of different factors (photoexcited carrier density, lattice temperature, strain, etc.) on the properties of lattice.

2.1 PHOTOEXCITATION AND RECOMBINATION OF CARRIERS

In this section the photoexcitation of carriers and their subsequent relaxation mechanisms are presented according to their time scales of occurrence (schematically illustrated in Fig. 5).

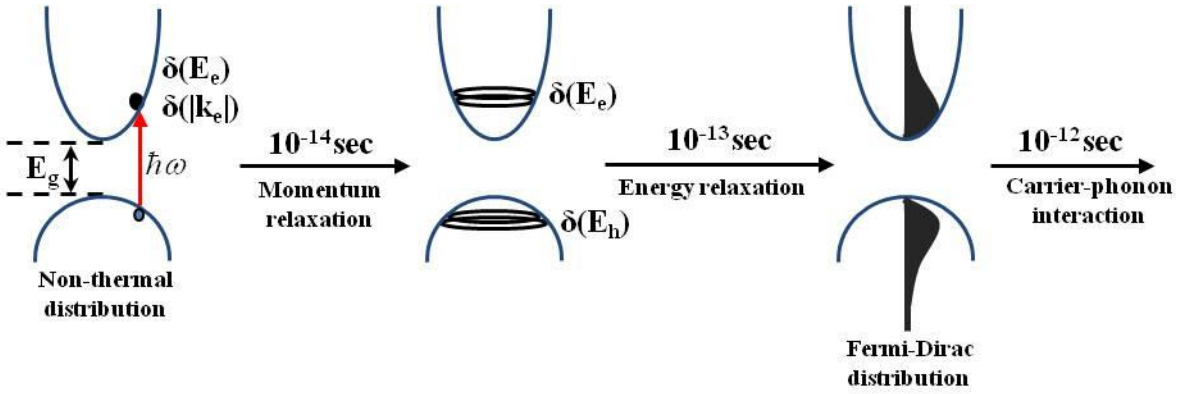

Figure 5: Photogeneration and evolution of carriers in semiconductors, after [27].

2.1.1 Carrier excitation

A laser pulse incident on a semiconductor creates a population of hot carriers within its skin-depth. If the energy of the exciting photon exceeds the band gap of the material, it can excite electronic transitions. Electron-hole pairs can be excited by first-order effects such as interband one-photon absorption, by second-order effects such as phonon-mediated indirect band gap excitation, or by intraband absorption by existent free-carriers. In all cases the overall energy and momentum must be conserved.

Single-photon absorption is a "vertical" process in which the initial and final states of the electron have nearly the same momentum, the photon momentum at optical frequencies being negligible. A photon is absorbed by an electron from VB, which is thus promoted to an excited state of CB (Fig. 6a). Vertical excitation can occur in indirect band gap semiconductors as well, for photon energies that can generate k-conserving transitions across the "direct" band gaps. In the case of indirect band-gap transitions the excitation is non-vertical, with phonons acting as a source of momentum (Fig. 6b).

Free carrier absorption occurs when an electron from CB absorbs a photon and is promoted to a higher energy level within the same band. This type of transitions increases the average energy of the hot carrier population, rather than its density. Because the excitation photon energy for the experiments reported here is near the direct band gap resonance, the free carrier absorption does not significantly affect our results.

Immediately after excitation the hot carriers form separate non-thermal distributions for electrons and holes, peaked in specific regions in the energy and momentum space. Their initial distributions depend on the laser pulse wavelength, laser polarization with respect to the crystalline axes of the sample, and the optical properties of the excited material.

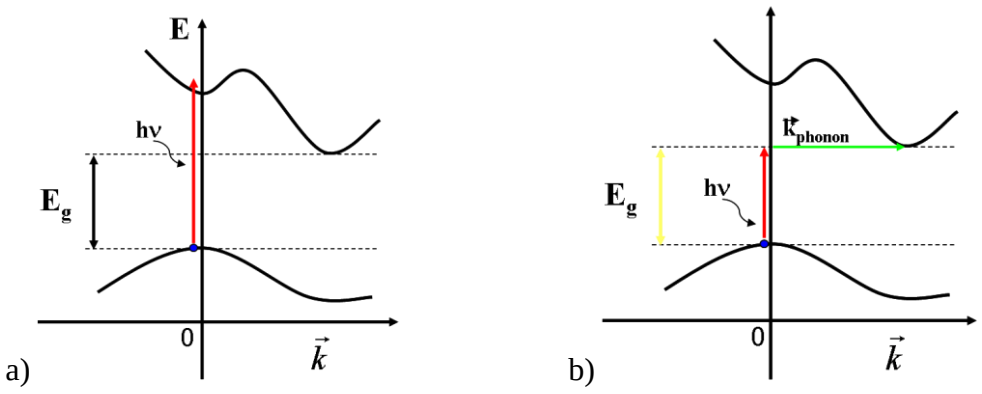

Figure 6: Schematic representation of possible photoinduced transitions in an indirect band-gap semiconductor: a) direct transition, and b) indirect transition.

In general, for a semiconductor with parabolic energy bands, the excess energy gained by a photoexcited electron-hole pair is given by the difference between the energy of the photon and the energy of the direct band gap, $\Delta E_{e-h} = h\nu_0 - E_g$. The excess energy $\Delta E_{carrier}$ gained by each type of carrier depends on its effective mass [34]. A part of the excess energy belongs to electron and is given by:

$$\Delta E_e = \frac{h\nu_0 - E_g}{\left(1 + \frac{m_e^*}{m_h^*}\right)}, \qquad \text{Eq. 2.1}$$

while the rest, $\Delta E_h = h\nu_0 - E_g - \Delta E_e$, belongs to the hole.

In the case of Si, such simple formulae are inadequate to represent the energy deposition in the electronic subsystems. The VBs of Si are warped, and the CBs have multiple valleys where the minima are along the Γ- X or Γ- L directions. Moreover, below the direct band-gap the transitions are phonon induced. Therefore, any calculation of energy deposition in the subsytems has to consider the specific band structure of Si.

2.1.2 Scattering events

The photoexcited electrons and holes relax from the non-thermal distributions through carrier-carrier and carrier-phonon scattering. On a timescale of tens of fs (~100 fs, [35]) after the excitation, carrier-carrier inelastic and elastic scattering events randomize the momentum and redistribute the energy of carriers between themselves. The carrier-carrier scattering processes involve electron-electron, hole-hole and electron-hole Coulomb interactions. Note that the energy and number of carriers do not change, but their energy and momentum are redistributed over the bands to form a thermal distribution. As an example of time scales for such events, the thermalization rate was calculated to be about 10 fs for Ge [36] for a carrier density of 10^{20} cm^{-3}, 60 fs for InP bulk samples, and 40 fs for GaAs in the range of 10^{16}-10^{18} cm^{-3} [37]. Through carrier-carrier scattering both the electron and hole systems evolve toward Maxwell-Boltzmann or Fermi-Dirac distributions, depending on the degree of excitation. Those distributions are initially characterized by different temperatures $T_e \neq T_h$ which, in the case of Maxwell-Boltzmann distributions (and at equilibrium), are given by the excess energy of the electron above CBM, $E_{excess} = \frac{3}{2} k_B T$, where T is the temperature of the distribution. Although the energy of each of the systems is assumed to be conserved during momentum and energy randomization, there is, however, exchange of energy in between the systems themselves and/or with the lattice. The energy lost to the lattice is small in comparison to the average energy of the systems, and it can be neglected [38].

The electron-hole scattering thermalizes the electrons and hole distributions, equilibrating their temperatures, i.e., $T_e = T_h$.

The rate at which a hot electron loses energy through scattering with the rest of $N-1 \approx N$ electrons is given by:

$$\left.\frac{dE}{dt}\right|_{carrier} \approx -4\pi N \frac{e^4}{\varepsilon_0^2}(2m^* E_{excess})^{-\frac{1}{2}}, \qquad \text{Eq. 2.2}$$

where e is the electronic charge, m^* is the electron effective mass, and ε_0 is the bulk dielectric constant. The hole relaxation through hole-hole scattering is governed by the corresponding equation [38].

After momentum randomization and energy redistribution, the photoexcited carriers lose their excess energy, i.e., energy above the band gap, to the lattice mainly by interaction with incoherent phonons until thermal equilibrium ($T_e = T_h = T_L$) is achieved. The scattering can be intra- or/and inter-valley. The inter-valley scattering requires large momentum exchange and has a longer time constant than the intra-valley scattering, but both of them occur on the order of hundred of femtoseconds. Each time an electron scatters with the lattice to emit a phonon, it loses energy equal to one quantum of phonon excitation, and the temperature of the lattice thereby increases by an equivalent amount.

The carrier-phonon scattering is governed by momentum and energy conservation. There are two mechanisms involved in electron-phonon coupling: the Frölich interaction of polar semiconductors and the deformation potential interaction present in both polar and non-polar materials, described in Chapter 2. The generated phonons can decay further by emitting two or more lower energy phonons such that energy and momentum are conserved.

2.1.3 Photoexcitation and scattering processes in our work

Our experiments involve pulses with ~400 nm central wavelength. The corresponding energy of the photon is ~3.1 eV, which is near the ≈3.4 eV energy of the $E_1 + E_0'$ direct band-gaps of Si, as shown in Fig. 7. Therefore our excitation photon is near the resonance for electronic transitions at E_1 and E_0' critical points. Even though our laser is not resonant with these transitions, we believe that these critical points describe the excitation with 3.1 eV light because of the lifetime broadening of the involved transitions at 300 K (see Section 2.4.1).

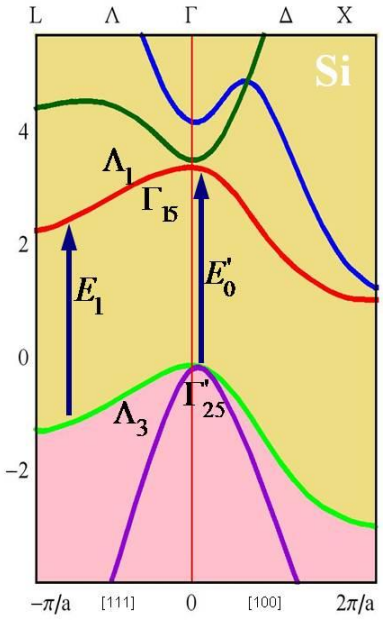

Figure 7: Transitions photoinduced in Si with ~ 3.1 eV photons. Photoabsorption occurs near the E_0' and E_1 critical points, corresponding to transitions near the Brillouin zone center (Γ point; minor) and a range of momenta along the line (L-valleys; major).

When the polarization of the exciting light is chosen to be parallel to [110] crystalline axis (Fig. 8), the excitation of the dominant E_1 critical point selects transitions along four out of the eight equivalent L-valleys of Si. The carriers are excited mainly into an energy band of

conduction states from about $\vec{k}_{el} \approx 0.8\frac{\pi}{a}(1,1,1)$ to the L symmetry point zone boundary ($L_{3'} \rightarrow L_1$ transitions, [34]). Note that lthough $E_0^{'}$ transitions close to the Γ point are possible, the small joint density-of-states renders this contribution smaller compared to the $L_{3'} \rightarrow L_1$ transitions (E_1 critical point; Section 1.2.4). At Γ point transitions can originate both from the *h*- and *l*-hole VBs, which is significant because of the influence of the hole density and their redistribution in between the *h*- and *l*-hole bands on the renormalization of the phonon self-energy (Subchapter 4.1). Considering that the excitation is dominated by the E_1 critical point, however, initially the photogenerated electrons and holes form distinct anisotropic non-thermal distributions with excess energies deposited in the CB and VB. The momentum distributions are defined by the joint density-of-states of the transition.

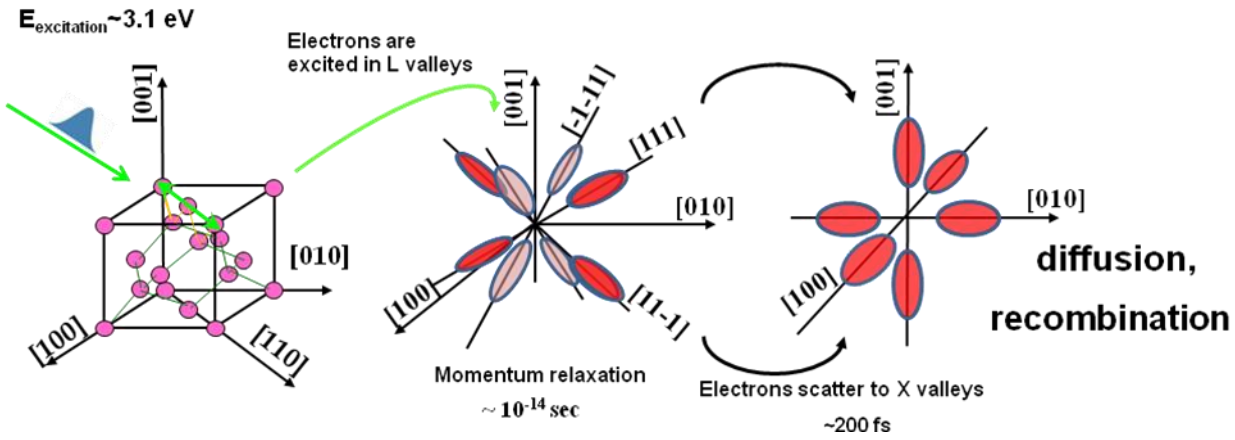

Figure 8: Dynamics of electrons after excitation of Si with ~3.1 eV light polarized along the [110] crystalline direction.

The sequence of processes governing the dynamics of photoexcited electrons after excitation is shown in Fig. 8. Depending on the laser polarization the carriers are excited selectively in 4 out of 8 L-valleys. On a time scale of tens of femtoseconds after excitation the carriers scatter among the 4 excited valleys and also to the other 4 unexcited valleys,

randomizing the momentum of the distributions, and eventually thermalizing them. With a time constant of ~300 fs [39], the carriers scatter from the L-valleys to the X-valleys, after which diffuse into the bulk and recombine.

There are three types of carrier scattering by phonons relevant to our experiments: inter- and intra-valley scattering by incoherent phonons, and scattering of carriers by the LO coherent phonon. They are listed below:

1. *Inter-valley scattering*: electrons excited anisotropically above the CB (through $L_{3'} \rightarrow L_1$ transitions) in 4 out of 8 L-valleys scatter by large wavevector incoherent phonons between those valleys and to the other 4 equivalent unexcited valleys, until their momentum is randomized. From the L-valleys, electrons can also scatter, on the same time scale, by large wavevector phonons to the X-valleys. Electrons excited above the CB through $\Gamma_{25'} \rightarrow \Gamma_{15}$ transitions scatter by large wavevector incoherent phonons to side valleys (either X or L);
2. *Intra-valley scattering* by incoherent phonons facilitates the relaxation of electrons to the CBM in both L- and X-valleys, transferring their excess energy to the lattice as thermal energy. The holes also relax toward the VBM by scattering with incoherent phonons.
3. *Carrier scattering by coherent LO phonons*. The zone-center LO phonons ($q = 0$) will produce changes into the energy band structure by successively compressing and dilating the crystalline lattice. In return, the changes in the band structure force the photoexcited free carriers to redistribute inside and in between the energy bands [28, 40] producing a "softening" of the lattice with respect to the LO phonon. Because of this softening, the energy of LO phonons acquire "self-energy" by being "dressed" with free carriers.

To summarize, in this section we described the scattering processes relevant to our experiments. In the next section we revise succinctly the recombination and diffusion processes. Recall that scattering, diffusion and recombination are competing processes, occurring simultaneously after excitation.

2.1.4 Diffusion and Recombination

Simultaneously with the onset of many-body interactions (i.e., carrier momentum and energy scattering) during and after photoexcitation, two other processes occur: diffusion and recombination. Diffusion starts as soon as the excitation generates in the semiconductor a gradient of excess carriers within the absorption depth of the excitation light. The gradient is steepest towards the bulk. Thus, diffusion causes the free carrier density to decreases from the more populated surface region into the less populated bulk.

The excess electrons and holes can recombine through various mechanisms including radiative, trap-assisted, surface [41] and Auger recombinations. The first two recombination processes have much longer characteristic time scales [42-45] than the time constants of various scattering processes described in the previous sections, and also than the time scale of our measurements. For native oxide covered Si the surface recombination and the effects of the band bending can be neglected, as has been shown by the experiments of Li et al. [46], which concluded that the diffusivity measurements results overlap for bulk and surface measurements rendering the surface recombination negligible for the transport calculations presented in Chapter 5. For our particular experimental conditions, the main recombination mechanism to take into account remains Auger recombination [38, 47-49]. In Auger (band-to-band) recombination an electron recombines with a hole and the energy released is transferred to another carrier. The

time constant depends on the carrier density, because Auger recombination is a two body process; the Auger time constant saturates at 6 ps at a carrier density of about 10^{20} cm^{-3} [38, 48].

In Table 1 are summarized some of the processes and time constants that define the photoexcited carrier energy, momentum, and distribution after photoexcitation. Because its time scale is longer than coherent LO phonon dephasing time, and diffusion is much more effective in decreasing the near-surface carrier density, the Auger recombination does not necessarily needs to be considered further in interpretation of the experimental data. For our experimental conditions the dominant channel for the surface carrier depletion is the ambipolar diffusion, which will be discussed at length in Chapter 5.

Table 1: Characteristic times for ultrafast carrier dynamics.

Process	Time scale (sec)
Carrier-carrier scattering	10^{-15}-10^{-2} [50]; 10^{-4} [27]
Intervalley scattering	10^{-4} [50]
Intravalley scattering	10^{-3} [50]
Carrier-optical phonon thermalization	10^{-12} [50]
Optical phonon-Acoustic phonon interaction	10^{-11} [50]
Lattice heat diffusion	~ 10^{-8} [50]

Summarizing, in this section we have reviewed the many-body processes that occur during and after electron-hole plasma is created by photoexcitation with an ultrafast pulse. Next we describe the generation of coherent LO phonon by the same pulse.

2.2 COHERENT LO PHONON GENERATION

In this section we will first succinctly review the nonlinear polarization arising from coupling of high intensity light with matter, to provide a basis for the phonon excitation during a Raman process. Then we will separately define the incoherent and coherent phonons and discuss their generation mechanisms.

2.2.1 Nonlinear polarization

Describing light-matter interaction phenomena [51, 52] starts with Maxwell's equations, which govern the linear and nonlinear propagation of electromagnetic fields in matter. Maxwell's equations in a dielectric medium are given by:

$$\nabla \times \vec{H} = \vec{J} + \frac{\partial \vec{D}}{\partial t}, \quad \nabla \times \vec{E} = -\mu_0 \frac{\partial \vec{H}}{\partial t},$$

$$\nabla \vec{D} = \rho \quad \nabla \cdot \vec{D} = \rho, \; \nabla \cdot \vec{B} = 0. \qquad \text{Eq. 2.3}$$

Within the material, the constituent equations are:

$$\vec{D} = \varepsilon_0 \vec{E} + \vec{P}, \; \vec{J} = \sigma \vec{E}. \qquad \text{Eq. 2.4}$$

The response of any material to an electromagnetic wave is described by the frequency dependent dielectric permittivity $\varepsilon(\omega)$ and magnetic permeability $\mu(\omega)$. For a weak incident field the response of the material is linear and described by the index of refraction $n(\omega) = \sqrt{\varepsilon(\omega)\mu(\omega)}$. The magnetic permeability is nearly independent of frequency at optical frequencies, i.e., $\mu(\omega) \approx 1$, therefore the index of refraction becomes $\tilde{n}(\omega) = \sqrt{\varepsilon(\omega)} = n + i\kappa$,

with the real part n describing the wave propagation and the imaginary part κ describing the absorption of light.

The propagation of the electric field is described by the plane-wave

$$E(x,t) = E_0\, e^{i(kx-wt)}. \qquad \text{Eq. 2.5}$$

The relationship between the field's wavevector *k* and frequency, $\omega = \frac{c}{n}k$, permits rewriting the wave equation in a form that includes both the propagation and absorption of light:

$$E(x,t) = E_0\, e^{i(\frac{\omega\tilde{n}}{c}x-\omega t)} = E_0\, e^{i(\frac{\omega\tilde{n}}{c}x-\omega t)} = E_0\, e^{-\frac{\omega\kappa}{c}x}\, e^{i(\frac{\omega n}{c}x-\omega t)}. \qquad \text{Eq. 2.6}$$

The absorbed electric field gives rise to a macroscopic polarization *P* in a material.

In the case of linear optics, the relationship between the applied field and induced polarization is linear:

$$P(t) = \varepsilon_0 \chi^{(1)} E(t), \qquad \text{Eq. 2.7}$$

where the complex dielectric constant $\varepsilon = \varepsilon_1 + i\,\varepsilon_2$ is related to the linear susceptibility:

$$\varepsilon = 1 + \chi^{(1)}. \qquad \text{Eq. 2.8}$$

The response of a nonlinear material to an intense field with components $\vec{E}_j(t)$ is described along crystalline direction i by [53, 54]

$$\vec{P}_i = \varepsilon_0 \chi_{ij}^{(1)} \vec{E}_j(t) + \vec{P}_i^{NL}, \qquad \text{Eq. 2.9}$$

where the i^{th} component of the nonlinear polarization is expressed as

$$\vec{P}_i^{NL}(E(t)) = \chi_{ijk}^{(2)} E_j(t) E_k(t) + \chi_{ijkl}^{(3)} E_j(t) E_k(t) E_l(t) + \ldots., \qquad \text{Eq. 2.10}$$

and $\chi^{(n)}$ is the n-th order susceptibility. The first term in the Eq. 2.9 represents the linear polarization, which is proportional to the applied electric field through the susceptibility $\chi^{(1)}$. The higher order terms in Eq. 2.10 are components of the nonlinear polarization, the higher-order

susceptibilities being tensorial quantities. To measure the nonlinear response, the excitation field has to be very intense, as the strength of the nonlinearity depends on the quadratic and higher terms in the applied field.

Combining the Maxwell's equations the nonlinear wave equation takes the form

$$\nabla^2 \vec{E} = \mu_0 \sigma \frac{\partial \vec{E}}{\partial t} + \mu_0 \varepsilon_0 \varepsilon \frac{\partial^2 \vec{E}}{\partial t^2} + \mu_0 \frac{\partial^2 \vec{P}^{NL}}{\partial t^2}. \qquad \text{Eq. 2.11}$$

If the incident fields propagate normal to the material, the nonlinear polarization $\vec{P}^{NL}$ drives the generation of waves $E(z,t) = \frac{1}{2} E_i e^{i(\omega_i t + k_i z)} + c.c.$ oscillating at frequency $\omega_i = \sum_{j=1}^{n} \pm \omega_j$ and having momentum $k_i = \sum_{j=1}^{n} \pm k_j$, where n is the number of the waves that mix inside the nonlinear crystal and the *z*-axis is normal to the material. The nonlinear phenomena occurring in a nonlinear crystal include Sum Frequency Generation, Kerr effect, electro-optic effect, etc. [53-55]. Some of those effects are important for this work, and will be discussed in Chapter 3.

2.2.2 Incoherent Raman scattering study of phonons

Conventional Raman spectroscopy is a general method for probing $q = 0$ phonon structure of matter [56]. Phonons excited by spontaneous Raman scattering are incoherent, i.e., the Raman process occurs stochastically so that there is no phase relationship between excited phonons. The mechanism of scattering involves energy exchange between a photon filed incident on a material and the atoms or molecules of the material under investigation, through absorption or emission of phonons. After illumination of the sample, the effect is shown in the inelastic component of

the scattered light, which appears as weak sidebands separated by the phonon frequency from the elastic component. A phonon vibrating at a frequency ω_{ph} introduces a displacement of an atom from its equilibrium position, which deforms the lattice and induces a change in the polarizability of the material. The polarization P is proportional to the product between susceptibility χ and the incident electric field E, and will comprise two components oscillating with the difference and the sum between the incident field frequency and phonon frequency; the fields radiated at those two frequencies are referred to as Stokes and anti-Stokes components of the scattered field. In the linear optics case, the polarization induces a sinusoidal modulation of the first order susceptibility, through the relation $\chi_{\alpha\beta} = \frac{\partial P_\alpha}{\partial E_\beta}$, where α, β are Cartesian coordinates. The ratio of the Stokes to the anti-Stokes intensities is $\frac{I_S}{I_{a-S}} = \frac{1+N}{N}$, where is the Bose occupancy factor of the phonon mode defined by Eq. 1.2. For Si the Stokes to anti-Stokes ratio was measured to be $\frac{1+N}{N} = 0.1$ at room temperature [57].

The Raman intensity is related to the vibration-induced polarizability change, to each vibrational mode of amplitude q_i being assigned a Raman tensor [58],

$$R^i = \frac{\partial \alpha_{mn}}{\partial q_i}, \qquad \text{Eq. 2.12}$$

defined as the nonzero first derivative of the polarization with respect to the amplitude of the vibration (vibrational normal coordinate). In Eq. 2.12 i is the index of the phonon branch, m and n are Cartesian coordinates x, y, z, and $\alpha_{mn} = \frac{\partial^2 U}{\partial E_m \partial E_n}$ is the polarizability tensor, with U being the total energy of the system and $E_{m,n}$ the components of the incident electric field. The derivative of energy U with respect to the displacement of the ions from their equilibrium

position gives the forces acting on the ions. The Raman tensor has the same symmetry as the mode that defines it. First-order Raman lines were observed and intensively studied in Si and diamond compounds by different methods [59].

As introduced in Chapter 1, there are three degenerate branches of the optical phonon in Si at the Brillouin zone center. Their polarizations are mutually perpendicular and their directions are usually chosen to be along [100] for TO_1, [010] for TO_2, and [001] for LO [58, 60]. Normally those modes are Raman active, but infrared inactive. In the presence of an applied static electric field or stress, however, they can become infrared active, their frequencies shift and the degeneracy is lifted [61].

The light couples with the optical phonons through by the second-order Raman coupling tensors which are usually denoted by R_1, R_2, R_3, [60]

$$R_1 = \begin{pmatrix} 0 & 0 & 0 \\ 0 & 0 & d \\ 0 & d & 0 \end{pmatrix}, \; R_2 = \begin{pmatrix} 0 & 0 & d \\ 0 & 0 & 0 \\ d & 0 & 0 \end{pmatrix}, \; R_3 = \begin{pmatrix} 0 & d & 0 \\ d & 0 & 0 \\ 0 & 0 & 0 \end{pmatrix}, \qquad \text{Eq. 2.13}$$

where d is a nonzero number which gives the strength of the Raman scattering efficiency [62]. These tensors correspond to a reference plane in which the z-direction is perpendicular to the surface of the Si sample. An incident light with its electric field polarized along the (110) crystalline plane and wavevector nearly parallel to crystalline direction [001], as it is in our experiments, will couple only with the zone-center LO phonon, and the light-matter coupling will be determined by the R_3 tensor.

2.2.3 Coherent Phonons and their generation mechanisms

"Coherent optical phonons" refers to vibrations of the lattice in which the ions are forced to move *in-phase* with each other through coupling of the lattice with the exciting light. However, a more appropriate label for coherently generated vibrations by ultrafast laser pulses would rather be "coherent states" of a single phonon mode [7]. These coherent states are defined by the eigenstates of the annihilator operator [51, 63], which are obtained through acting on a harmonic oscillator ground state with the displacement operator. The expectation values of the position and momentum operators for coherent states are non-zero.

With ultrafast light pulses, coherent phonons of various frequencies, both acoustic and optic, can be probed in time domain by pump-probe experiments or other techniques [64]; the requirement for coherent phonon generation and detection is that the duration of the exciting pulse must be shorter than the oscillation period of the target phonon. Otherwise, the coherent phonon generation follows the same symmetry rules as the incoherent phonon excitation. By optical methods, surface generation and detection of phonons was probed first for acoustic phonons [65]. Coherent optical phonons were first observed in n-GaAs by transient reflectivity electro-optic sampling (EOS) technique [8]. During late 1980's [66] and early 1990s the excitation of coherent longitudinal optical LO phonons in bulk semiconductors, semimetals, and insulators and their detection by time-resolved experiments was demonstrated using femtosecond laser pulses [8, 67-69].

By contrast to the incoherent phonons, which are generated by energy transfer from the photo-excited carriers to the lattice or by incoherent Raman scattering as we have seen in the previous section, coherent optical phonons are created during the laser pulse illumination. Both pump and probe pulses can be regarded as delta-functions in comparison to the phonon's period.

The laser pulses launch the in-phase collective vibration of the lattice by creating a driving force which forces the displacement coordinates to evolve as a non-zero ensemble average described by the harmonic oscillator equation of motion (Eq. 2.14). The driving force is different for different coherent excitation mechanisms. It can be classified into Raman or non-Raman type [70]. Coherent phonon excitation and measurement has also been observed with X-ray diffraction [71, 72].

The mechanisms proposed for excitation of Raman active coherent LO phonons in semiconductors include ultrafast screening of the surface space-charge fields, displacive excitation of coherent phonons (DECP) and impulsive stimulated Raman scattering (ISRS). ISRS primarily occurs in transparent media, while DECP is prevalent in opaque materials.

The generation of LO coherent phonon by ultrafast screening of surface space-charged fields is based on the photoexcited carriers at the surface of the semiconductor screening the surface macroscopic electric field set-up due Fermi-level pinning at the surface. The ionic displacements couple with the electric field and the LO coherent phonons are launched inside the region containing the surface-space-charge electric field. This mechanism is operative in polar semiconductors of III-V group, such as GaAs, and is covered in literature by extended discussions (for example, [67]).

Displacive excitation of coherent phonons (DECP) was introduced by Zeiger et al. in 1992 [68] to explain coherent phonon excitation in semimetals and semiconductors. In their case, the sudden excitation of the sample with 1.98 eV light across the band gap of Bi, Sb, Te and Ti^2O^3 causes a shift in the excited state nuclear potential from the ground state minimum at position $Q_0(t<0)$ and, thus, launching the coherent oscillation of the lattice. In other words, the photo-excitation creates a new electron-hole pair distribution $N(t)$, which imposes a

displacement of the atoms' equilibrium positions. The atoms experience a force proportional to the excited carrier density, $f(N)$, which drives the nuclei to move coherently towards the new minimum $Q_0(t) \propto N(t)$ and start vibrating following a cosine-like oscillation with amplitude $Q(t) \propto N(t)$. Zeiger et al. give the equation of phonon motion as:

$$\frac{\partial^2 Q(t)}{\partial^2 t} + 2\gamma \frac{\partial Q(t)}{\partial t} + \omega_0^2 Q(t) = \omega_0^2 Q_0(t) \; (= f(N)), \qquad \text{Eq. 2.14}$$

where γ is the phenomenological damping rate of the coherent phonon and ω_0 is its oscillation frequency.

Kuznetsov and Stanton [7] constructed a QM description of the DECP mechanism starting from the phenomenological model introduced by Zeiger et al. [68]. They wrote the Hamiltonian of the system as

$$H = \sum_{k,n} \varepsilon_{nk} c_{nk}^{+} c_{nk} + \sum_{q} \hbar \omega_q b_q^{+} b_q + \sum_{k,n,q} M_{kq}^{n} (b_q + b_{-q}^{+}) c_{nk}^{+} c_{nk+q}. \qquad \text{Eq. 2.15}$$

This Hamiltonian contains terms given, in order, by the electron distribution defined by the creation and annihilation operators c_{nk}^{+} and c_{nk}, phonon system defined by operators b_q^{+} and b_q, and electron-phonon interaction defined by the deformation potential matrix element M_{kq}^{n}; $M_{kq}^{n} = C_k^n \sqrt{\frac{\hbar}{2\omega_q \rho V}}$ includes the deformation potential matrix element C_k^n (which gives the change of electronic state $|n,k\rangle$ when a phonon produces a displacement *u* of the lattice), the mass density ρ of the sample, and its volume *V*. In the Hamiltonian expression n is the band index (conduction or valence), k is the electron wavevector, q is the phonon wavevector, and ω_q is the phonon dispersion. With the coherent phonon amplitude defined as the sum of expectation values for creation and annihilation of phonons $D_q = \langle b_q \rangle + \langle b_{-q}^{+} \rangle = B_q + B_{-q}^{+}$, and

the reduced single-particle density matrix related to the spatial charge density of the electrons, $n^{n}_{k,k+q} = \left\langle c^{+}_{nk} c_{nk+q} \right\rangle$, the final expression of the coherent phonon amplitude obtained in [7] is:

$$\frac{\partial^2 (D_q)}{\partial t^2} + \omega_q^2 D_q = -2\omega_q \sum_{n,k} M^{n}_{kq} \left\langle c^{+}_{nk} c_{nk+q} \right\rangle . \qquad \text{Eq. 2.16}$$

Comparing this equation with Eq. 2.14 of Zeiger [68], we observe that the coherent phonons are initiated by the light induced spatial charge density of electrons. The electronic density matrix is diagonal for linear absorption, which is the condition for coherently driving only zone-center ($q = 0$) mode.

The amplitude of the lattice displacement for a $q = 0$ phonon is defined as

$$u_0 = \frac{C^{v} - C^{c}}{\rho \omega_0^2} \frac{N_0}{V} , \qquad \text{Eq. 2.17}$$

and the displacive force dependence on photoexcited carrier density $N(t)$ takes the form:

$$F(t) = 2\omega_0 \sqrt{\frac{\hbar}{2\omega_0 \rho V}} (C^{v} - C^{c}) N(t) . \qquad \text{Eq. 2.18}$$

Thus, according to the Kuznetsov and Stanton model the coherent phonon excitation via the displacive model depends on the difference between the deformation potentials between the optically coupled bands and the charge density excited within them.

Impulsive Stimulated Raman Scattering (ISRS) consists of inducing the coherent vibration directly in the ground state by stimulated Raman processes. This requires the excitation pulse to span a broad spectrum that exceeds the vibrational energy of the Raman active mode. This will always be the case if the laser pulse duration is shorter than the phonon oscillation period. Coherent oscillations studied by ISRS experiments were first observed in transmission

for materials transparent to the incident light [66]. The first application of ISRS technique to study phonons in opaque materials was demonstrated in Bi and Sb by reflection in 1990 [69].

Merlin [70] summarized in a simple way the mechanism of impulsive driving of coherent phonons: the dielectric function, which is proportional to the change in susceptibility χ of the material, is modulated at the phonon frequency through the second order polarization induced by the exciting light. The electromagnetic energy density change in the material is given by $\delta U = \frac{1}{2}\delta\chi\left|E_0(\vec{r},t)^2\right|$ [54], where E_0 is the magnitude of the exciting field, and the change in susceptibility is directly proportional to the phonon amplitude Q through the relation $\delta\chi \approx \frac{\partial\chi}{\partial Q}Q(\vec{r},t)$. The change in energy density is proportional to the amplitude of the phonon and provides a force density that initiates the coherent oscillation. This force is proportional to the laser pulse intensity.

In the harmonic approximation, the ISRS generated coherent phonon motion is expressed by Eq. 2.14 [65, 70], in which the right term is given by the phonon driving force [67, 73]

$$F(t) = \frac{\mu}{2}N\frac{\partial\alpha}{\partial Q}\bigg|_0 : \vec{E}\vec{E}, \qquad \text{Eq. 2.19}$$

where μ is the reduced lattice mass, Q is the amplitude of the phonon (ensemble average of the in-phase displacement coordinates), N the density of oscillators, and α the polarizability tensor. The driving force is proportional therefore to the Raman coupling tensor of Eq. 2.12:

$$F(\vec{r},t) = \sum_{kl}\vec{R}_{kl}E_k(\vec{r},t)E_l(\vec{r},t), \qquad \text{Eq. 2.20}$$

where E_k and E_l are components of light differing through the Raman frequency.

A mechanism combining both the displacive and impulsive contributions and called Coherent Raman Scattering (CRS) was first proposed by Garrett et al. [74], but a more general excitation mechanism that incorporates and bridges these cases was described theoretically and applied to Sb by Stevens [75]. This model was elaborated by Riffe et al. to the case where the displacive force decays with a finite lifetime, and applied to diamond structure materials and, in particular, to Si [76]. Riffe et al. used the coherent phonon initial phase change with the excitation wavelength as a measure of which mechanism dominates the coherent LO phonon generation in Si. We discuss in more detail the difference between the DECP and ISRS mechanisms and the results of the models of Stevens and Riffe in relation to our results in Subchapter 4.4. In short, in our experiments on Si both the impulsive and displacive mechanisms participate in generation of coherent LO phonons. However, the wavelength dependence of the phonon generation does not agree with the modeling of Riffe, indicating that the current understanding of the generation mechanisms is incomplete.

To summarize, so far we discussed in this chapter how the photoexcited carrier distribution is generated and evolves with time, what coherent phonons are and how are they excited by light. We also described the carrier photogeneration and LO phonon generation mechanisms relevant to our particular experiments. In the next section we will review the interaction between free carriers and the coherent LO phonons.

2.3 CARRIER-LO PHONON INTERACTION

The electron-phonon interaction is an important process, which affects the optical and transport properties of semiconductor devices. The manner in which the motion of electrons inside the crystal is perturbed by the motion of the lattice ions defines the type of carrier-phonon interaction [51, 52]. The type of interaction depends on whether the lattice is polar or not. In polar materials such as GaAs (III-V), the electrons couple strongly with LO phonons by the Fröhlich interaction mechanism: the atomic displacements of differently charged ions create longitudinal electric fields, which affect the free electron motion through long-range Coulomb interaction. This interaction mechanism involves intra-band electron-phonon scattering. For the non-polar semiconductors, such as Si, there is no charge transfer between the atoms forming the unit cell. Hence, there are no long-range longitudinal fields that could induce the Fröhlich interaction. Rather, electrons interact with the LO phonons through the deformation potential mechanism: the displacement of the atoms from their equilibrium positions due to phonon oscillation has a similar effect on the energy band structure as an externally applied strain (Section 2.3.1). The changes in the band structure give rise to a force that couples the phonons with the free carriers. Likewise, the transmission of electrons through a crystalline lattice distorts the lattice leading to the emission of phonons. Both the action of phonons on the electrons and the opposite action on phonons by electrons via deformation of the crystalline lattice play a part in coherent LO phonon generation and dephasing in Si.

The strength of the carrier-phonon coupling is given by the electron-phonon interaction matrix elements, which are expressed in terms of deformation potentials. The electron-phonon scattering mediated by deformation potential interaction involve both intra- and inter-valley scattering of electrons by phonons with appropriate energies and wave vectors, as required by

conservation laws. The deformation potentials are a measure of the absolute shift in energy of a particular band involved in the transitions. Values of deformation potentials corresponding to different transition types and different phonons were measured by many groups (a comprehensive list adapted from literature is presented in the App. C). The deformation potentials involved in the carrier-phonon coupling are physically the same as the deformation potentials involved in the distortion of lattice by a strain. It should be noted that the deformation potential interaction is present in polar III-V compounds as well, but its effect on the carrier-phonon interaction is weaker in comparison with the Fröhlich interaction. Also, the transfer of hole energy to the lattice occurs primary through optical phonons, again through deformation potential interactions, as the holes scatter between valence band states close to $k \sim 0$ [77].

Through the deformation potential interaction, both carriers and LO phonons gain the associated complex self-energy, which renormalizes the frequencies of the unperturbed system. For both carriers and LO phonon the self-energy is a complex quantity, the real part being proportional to their frequencies and the imaginary part to their broadening; it arises from correction to the carrier/phonon energy of higher order of the perturbation Hamiltonian. Corrections of different order of perturbation can be estimated starting with the unperturbed states and adding the perturbation Hamiltonian to the Schrödinger equation as shown below.

We start with the QM treatment of a perfect semiconductor crystal, which, in the absence of any external perturbation, is described by the following Hamiltonian [78]:

$$H_0 = \sum_i \frac{p_i^2}{2m_i} + \frac{1}{2}\sum_{\substack{i',i \\ i'\neq i}} \frac{e^2}{4\pi\varepsilon_0 |r_i - r_{i'}|} + \sum_j \frac{P_j^2}{2M_j} + \frac{1}{2}\sum_{\substack{j',j \\ j'\neq j}} \frac{Z_j Z_{j'} e^2}{4\pi\varepsilon_0 |R_j - R_{j'}|} - \frac{1}{2}\sum_{j,i} \frac{Z_j e^2}{4\pi\varepsilon_0 |r_i - R_j|}. \qquad \text{Eq. 2.21}$$

The Hamiltonian includes, in this order, the contributions of the electrons, ions and electron-ion (phonon) interactions; p_i, r_i, m_i are the momentum operator, position and mass of the i^{th} electron, P_j, R_j, M_j are the momentum operator, position and mass of the j^{th} ion, Z is the atomic number of

the nucleus, ε_0 is the permittivity of vacuum, and *e* is the electron charge. With the assumptions that only the valence electrons contribute to the electronic term of the Hamiltonian while the core electrons and nuclei are considered together as "ion cores", the ions are almost stationary and, rather than following the motion of the electrons, they "see" only a time averaged adiabatic electronic potential (adiabatic approximation), and that every electron moves in the same average potential V(r) (mean-field approximation), the electronic contribution to the Hamiltonian takes the form:

$$H_e = \sum_i \frac{p_i^2}{2m_i} + \frac{1}{2}\sum_{\substack{i,i' \\ i \neq i'}} \frac{e^2}{4\pi\varepsilon_0 \left|\vec{r}_i - \vec{r}_{i'}\right|}. \qquad \text{Eq. 2.22}$$

The eigenstates of the electronic system are the Bloch wavefunctions $\left\langle \vec{r} \middle| n, \vec{k} \right\rangle = u_{n,k}(\vec{r}) e^{i\vec{k}\cdot\vec{r}}$, while the eigenvalues $E_n(k)$ represent the possible energies electrons can have in the crystal. A plot of the eigenvalues against the momentum *k* gives the band energy structure of a semiconductor. In the wavefunctions' expression *n* is the band index, *k* is the crystal momentum, and $u_{n,k}(\vec{r})$ is a periodic function with the periodicity of the average potential V(r). To the first approximation, the ions (nucleus + core electrons) interacting through a potential $V(R_j - R_{j'})$ contribute to the total Hamiltonian by

$$H_{ion} = \sum_j \frac{P_j^2}{2M_j} + \frac{1}{2}\sum_{\substack{j',j \\ j' \neq j}} \frac{Z_j Z_{j'} e^2}{4\pi\varepsilon_0 \left|R_j - R_{j'}\right|}, \qquad \text{Eq. 2.23}$$

where $R_j - R_{j'}$ is the distance between ions j and j'.

The interaction between electrons and ions is represented by

$$H_{e-ph} = \frac{1}{2}\sum_{i,j} \frac{Z_j e^2}{4\pi\varepsilon_0 \left|\vec{r}_i - \vec{R}_{j0}\right|}. \qquad \text{Eq. 2.24}$$

When the system is subject to even a weak perturbation $H' << H_0$ its electronic eigenstates and eigenvalues are altered. The new eigenstates and eigenvalues can be written as Taylor expansions in terms of the unperturbed eigenvalues E_n^0 and eigenvectors $|n^0\rangle$,

$$E_n = E_n^0 + \lambda E_n^1 + \lambda^2 E_n^2 + ... \quad \text{Eq. 2.25}$$

$$|n\rangle = |n^0\rangle + \lambda |n^1\rangle + \lambda^2 |n^2\rangle + ...$$

where λ is a dimensionless parameter used for keeping track of the order of the corrections. To express the contribution of each order to the new energy, the Schrödinger equation for the perturbed Hamiltonian is written as:

$$(H_0 + H')|n\rangle = E_n|n\rangle. \quad \text{Eq. 2.26}$$

Expanding Eq. 2.26 and matching the left and the right side coefficients for each power of λ, one can compute the corrections to the energy and wavefunctions [51].

The lattice vibration acts like a perturbation of the system, interacting with the electrons and renormalizing their electronic energies by the higher order corrections in Eq. 2.25. The result of the interaction is that the phonon has its energies renormalized as well [28, 79], by the higher terms of perturbation. The effect of the carrier-phonon interactions relevant to LO phonons in Si has been studied extensively. The particularly relevant work of Cerdeira and Cardona [28] is presented in the next section.

2.3.1 Previous work relevant to our case

Recall that, in the particular case of excitation of Si by ~ 3.1 eV photons, electrons excited in the L-valleys and coherent LO phonons are generated at time zero through coupling through the deformation potential interaction. The effect of free carriers and LO phonons on each other is

resumed in the next sections of this Chapter, in the context of previous work done on this subject.

LO phonon interaction with L-valley electrons has been studied in the doped indirect band-gap Ge [28]. Some of the aspects of Ge are applicable to the L-valley excitation of Si. The LO phonon produces dynamic changes in the energy band structure; it lowers the energy of some L-valleys and raises the energy of others causing the free electrons to redistribute among the L-valleys dynamically as that lattice vibrates, as shown in Fig. 9.

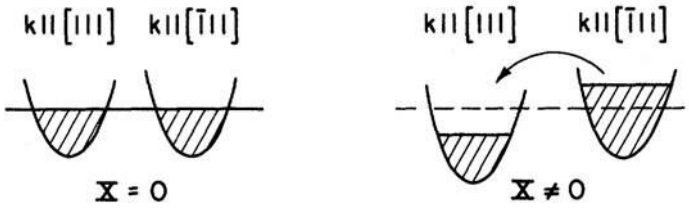

Figure 9: Lowering of the L-valley due to optical phonon is followed by redistribution of electrons between the valleys; from [28];

The charge redistribution depends on the phonon frequency and the intervalley scattering rate. In the case of Ge, the LO phonon frequency is sufficiently slow for this to occur, but in the case of Si, with an LO phonon frequency of 64 fs, it is not known whether the redistribution is sufficiently fast for this mechanism for LO phonon-carrier interaction in the L-valleys. In the case of Si under the equilibrium conditions relevant to incoherent Raman spectroscopy, we need to consider the CBM carrier in the X-valleys. When free electrons are present in the X-valleys, the LO phonon oscillation lowers the CBM (see Fig. 10a). The LO phonons influence also free holes, splitting the degenerate (at Γ point) heavy- and light-hole bands, and shifting upwards the VBM (see Fig. 10b). The change in carrier' energy produces weakening of the Si bonds, and the LO phonon frequency is renormalized as well. The order of the carrier-phonon interaction is different for electrons and holes, as seen through the doped carrier induced softening of the LO

phonon frequency, the hole-phonon interaction being considerably stronger than the electron-phonon interaction. Cerdeira and Cardona showed that the LO phonon frequency decreases with an increase in free carrier density in both cases, and its dephasing rate changes linearly with the carrier density, negligibly in the case of free electrons.

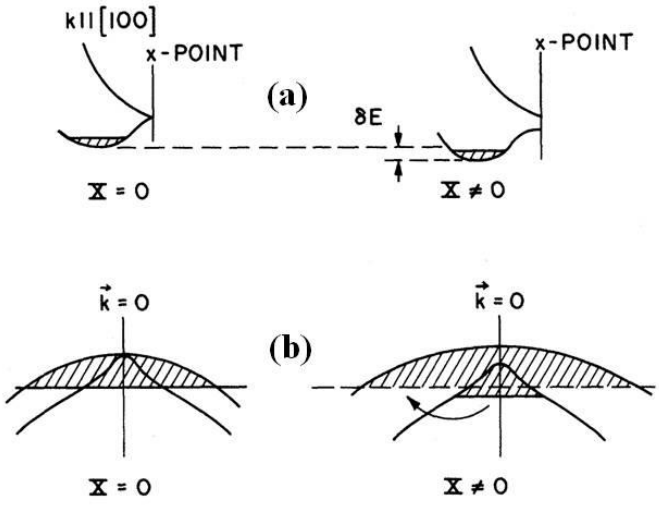

Figure 10: Splitting and shifting of the CBM (a) and VBM (b) due to optical phonon, from [28].

Regarding our experimental results, we can clearly see the effects described in Ref. [28, 79] as a red shift of LO phonon frequency and as an increase of the dephasing rate with carrier density (see Subchapter 4.1). However, in our case the situation is much more complicated than the static case of cold doping free carriers studied by Raman scattering. The dynamic nature of the high density photoexcited carrier population, the population of both the L- and X-valleys, as well as the simultaneous presence in the system of both holes and electrons, render the attempt to separate and quantitatively evaluate their contributions to the LO phonon frequency change quite challenging. Moreover, beside the changes due to the interaction with free carriers, there are also other factors inducing changes as well, as we shall see in the next section.

2.4 BAND-GAP RENORMALIZATION

"Band gap renormalization" refers to the change of band gap energy with respect to the unperturbed material in the presence of an external force or doping by carriers. The changes in the material are not restricted only to the band gap, but also affect the band structure in general. They can be induced by doping with impurities (free carriers), optically injected free carriers, pressure, temperature, coherent lattice vibrations, etc. All those perturbations have a similar effect, i.e., they distort and/or strain the lattice. To stress the importance of those changes, I just mention that, when a semiconductor's dimension approaches the nanoscale regime, any built-in or induced strain affects greatly its properties. Engineered strain in Si devices is already being used to increase the performances of microelectronic devices, i.e., transistor gates with lengths of 65 nm and less [80].

This renormalization is an important issue in our work, since any change in the energy band structure influences the absorption of light in Si. At the photon energy of ~ 3.1 eV we use for excitation, we are near-resonance with the critical point E_1. A decrease of the E_1 energy brings our exciting photon even closer to resonance, and therefore influences the LO phonon generation and its interaction with free carriers, an argument we use in Subchapter 4.4. We also consider the renormalization of the indirect band-gap of Si due to carrier density and lattice temperature in the model of diffusion described in Chapter 5, which we use to retrieve the carrier density and lattice temperature curves needed for data analyzing (Subchapter 4.1).

The change in band energy influences, in its turn, the LO phonon, as we mentioned in the last section. Therefore we will review next the factors affecting the band-gap energy: initial

doping type and amount, photoexcited carriers in both CB and VB, the effect of lattice temperature, effects of LO phonons on the CB and VB, and 5) applied pressure.

2.4.1 Doping effect on the band-gap

Bound and free carriers interact among themselves through Coulomb potential, producing a shift in the crystal's energy eigenstates. The shift happens because Coulomb interaction acts like a perturbation on the single electron (hole) states. This perturbation has contributions from the screening of the ions by the free carriers, the interaction of each carrier with the field created by the other carriers, the reduction of carrier energy following the Pauli exclusion, and electron-hole correlation mediated by Coulomb interaction. The perturbation adds to the effective electronic part of the Hamiltonian and produces broadening of the energy bands and narrowing of the energy gaps.

The presence of free carriers in the CB and VB (state filling) through either n- and p-type doping induces band gap shrinkage due to the correlations and exchange processes between charged carriers [81]. Both doped and photoexcited free carriers contribute to this effect. The renormalization of the band gap is therefore due to many-body interactions between free carriers (electrons or holes) and their environment, which give rise to a correction to the carriers' energy. This correction, the carrier self-energy, is a complex quantity of which the real part reflects the shift of the single particle energies due to many-body interactions, and the imaginary part reflects the broadening of the energy states, i.e. inverse of the decay time, arising from the finite lifetime of the carriers on these states.

The various interactions and their effect on the band gap are reviewed in this section, and their combined effect is schematically presented in Fig. 11.

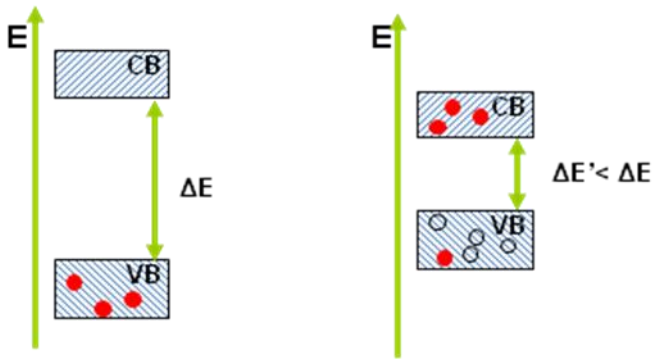

Figure 11: Illustration of band-gap shrinkage due to doping. CB stands for conduction band and VB for valence band; red filled circles represent the electrons and grey shallow circles the holes.

Si can be doped with both electron donors or acceptors. A pentavalent (donor) atom replacing a Si atom will have four of its valence electrons forming four bonds with the Si atoms around, and one extra electron which will be weakly bound to the positively charged impurity ion by Coulomb forces. For low density doping, the attractive potential seen by the extra electron is simply given by $V(r) = \frac{-e^2}{4\pi\varepsilon r}$, where $\varepsilon = \varepsilon_0\,\varepsilon_r$ is the dielectric constant of the semiconductor. In the same manner, for a trivalent (acceptor) atom replacing a Si atom and low density doping, the hole left free will "see" a repulsive potential of the same type.

When the doping level increases, an electron (hole) will "see" this bare potential essentially modified by the onset of screening by the other free carriers. This screening consists in the fact that free carriers change their local density in response to the bare potential and therefore the effect of the ionized impurity is reduced by a factor of $e^{-\lambda r}$, where $\lambda = \frac{e^2(n+p)}{\varepsilon_B T}$ [82], where n and p are the free carrier densities, k_B is Boltzmann's constant and T is the absolute temperature. The electron-donor interaction causes the donor level to shift towards the conduction band, but the band gap energy remains unchanged. The shift of the CB is due to the presence of free electrons. The free electrons present in the conduction band interact strongly

with each other, their momentum spreading so that, in accordance with the Pauli exclusion principle, their wavefunctions overlap is minimized. Therefore the total energy of the system will have a contribution from the average Coulomb repulsion energy between electrons, which cancel out with the positive background of the impurities, and another from an exchange term between electrons. The exchange energy lowers the total energy of the system, i.e. the band gap is reduced (or "renormalized").

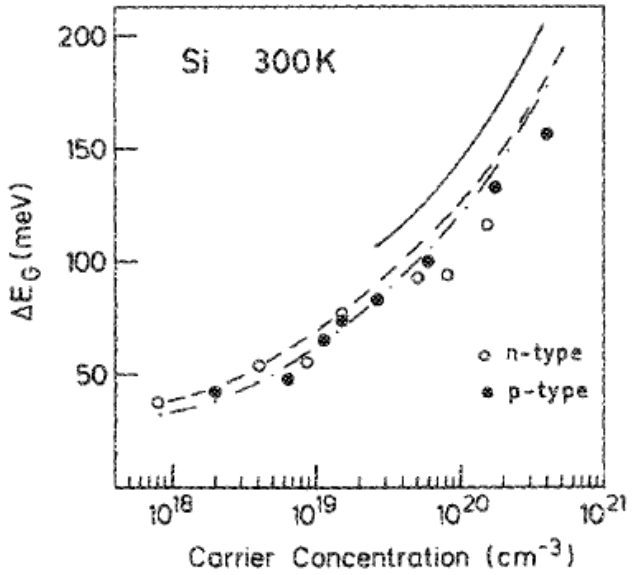

Figure 12: Bandgap shrinkage $\Delta E_g = E_{g(0)} - E_g$ as a function of carrier concentration. The band gap for intrinsic Si is $E_{g(0)} = 1.1\,eV$; open and filled circles are experimental results, lines are theoretical results by different groups (from Wagner and Alamo [83]).

Because of its influence on the material properties, the band gap narrowing of Si due to donor (acceptor) doping was experimentally and theoretically investigated by many authors. For example, Wagner and Alamo [83] compiled experimental and theoretical data for the absorption edge of Si, for both n- and p-type doping (Fig. 12), and Oschilies et al. calculated the electron induced bad-gap renormalization as a function of doping carrier concentration in Si [84].

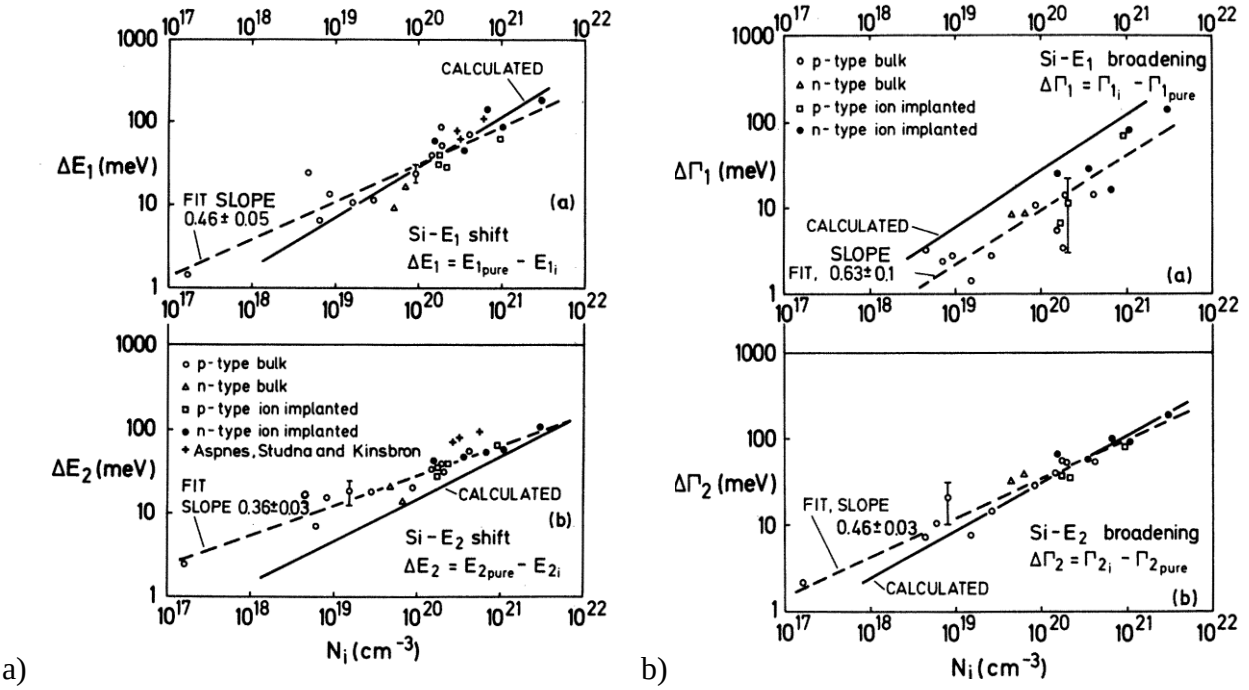

Figure 13: The influence of doping on the critical points of Si: a) both critical points E_1 and E_2 are red shifted for doped samples, with respect to an undoped sample (pure); b) broadening parameter for both critical points increases as the carrier density increases. From Ref. [34]

Viña and Cardona [34] also measured and calculated the shift of critical points and their broadening in the case of Si (see Fig. 13). Their results show that not only the band-gap, but other critical points are influenced by doping, which is also in accordance to the measurements of the absorption spectra of Si as a function of free carrier density by Jellison [85].

2.4.2 Photoexcited carriers effect on the band-gap

The presence of optically injected carriers influences the indirect band gap of Si much like the free charge carriers introduced through doping. In this case both electrons and holes affect the band gap simultaneously. The band gap renormalization is sensitive to the carrier distribution

and it renormalizes by an amount proportional to the total carrier density given by doping and photoexcitation at each instant of time after excitation, until the system returns to equilibrium.

2.4.3 Lattice temperature effect on the band-gap

It has been established that the increase of lattice temperature (T_L) produces shifts and broadenings of the band edges and critical points in the energy bands of a semiconductor [86-88]. The influence of lattice temperature on the energy bands arises from contributions of the thermally induced volume expansion, which modifies the bond lengths and distorts the electronic cloud, and the interaction of the lattice vibrations with the carriers, which produces shifts of the band structure [89]. An increased interatomic spacing results from the anharmonicity of the interatomic potential. Thermal expansion of the lattice decreases the potential seen by the electrons in the material, which in turn reduces the band-gap energy. The scattering of an electron (or hole) by a phonon, i.e. the electron-phonon interaction, affects the energies of both electron and phonon. Each of the quasiparticles will gain a correction of the energy, the self-energy, arising from higher order terms of the Hamiltonian. The thermal expansion has a much smaller contribution on the band gap renormalization than the carrier-phonon interaction. Note that temperature also affects the intrinsic carrier concentration, the effective conduction, the valence band densities of states, and the effective masses of the density of states [90].

An expression that relates the band gap energy E_g with the lattice temperature T_L has been empirically deduced by Varshni [91]:

$$E_g(T_L) = E_{g_0} - \frac{\alpha T_L^2}{\beta + T_L}, \qquad \text{Eq. 2.27}$$

where E_{g_0} is the band gap energy at 0 K, and α, β are fitting constants for the experimental data. Varshni found this expression to describe fairly well the data (E_g vs T), acquired for both direct and indirect band gap semiconductors, only at higher temperatures. For the particular case of Si and for $E_0 = 1.1557\,\text{eV}$, the following fitting constants were determined: $\alpha = 7.021\times10^{-4}\,\text{K}^{-1}$, $\beta = 1108\,\text{K}$. An excellent fit for $E_g(T)$ was obtained for Si by Cardona [92], with the empirical formula

$$E_g(T_L) = E_{g_0} - \frac{\alpha\Theta}{2}\left[\sqrt[p]{1+\left(\frac{2T_L}{\Theta}\right)^2} - 1\right], \qquad \text{Eq. 2.28}$$

where the fitting coefficients were found to be $p = 2.33$, $\theta = 405.6\,\text{K}$, $\alpha = 0.3176\,\text{meV/K}$. Note that the critical points E_1 and E_2 are also affected by the lattice temperature. Tao et al. [93] calculated both their energy and broadening as a function of temperature. Their results show the band gap energy decreasing and the peak broadening parameter increasing for both critical points. In the case of photoexcitation, however, the temperature dependence of the critical points does not affect the light absorption because the laser pulse is much shorter than the time scale for energy transfer from the electronic system to the lattice.

2.4.4 LO phonon effect on the band-gap

The splitting and shiftings of the energy bands of Si due to zone-center LO phonon were summarized at the end of Subchapter 2.3. The LO phonon acts like a sheer strain [28] applied in [111] direction. In other words, in the same way as for static stress, the displacements of atoms associated with lattice vibrations create a strain field which locally modifies the energy band structure. The effect of strain on the energy bands is presented in the next section.

2.4.5 Strain effect on the band gap

The band gap energy depends on the applied pressure because of the change in the bonds lengths and the consequent change in the elastic constants of the material, which implies a redistribution of electronic energies [94]. Applied stress induces a static displacement in the positions of atoms which will change the electronic energies at different points in the Brillouin zone. In other words, a deformation of the crystal induces a shift δE_{nk} of the known energy of a non-degenerate band E_{nk} of band index n and wave-vector k. The shift of a particular energy band is proportional to the appropriate deformation potential constant D of the crystal through the relation $\delta E_{nk} = D\frac{u}{a}$, where u is the displacement of the atom and a is the lattice constant [20]. The effect of the strain on the band-gap depends on the type of the stress and its direction, as it will be detailed in App. C. As an example only, the split of the *hh* and *lh* for a uniaxial compressive stress applied parallel to [001] axis in Si determined by Hensel and Feher [95] is shown in Fig. 14.

Built-in stress is induced, for example, by doping or/and impurity atoms (i.e. Carbon, in the case of Si samples) [96]. Boron (B) atoms are smaller than Si atoms, and any B atom inserted exerts an atomically localized tensile strain in the lattice. For high B atom concentrations these atomic strains add to form a region of strain which is resisted by the intrinsic Si regions resulting in a contraction of the lattice and a decrease in the lattice constant [96]. For phosphorus-doped Si the observed lattice contraction is smaller, which is attributed to the similar atomic sizes of P and Si [97].

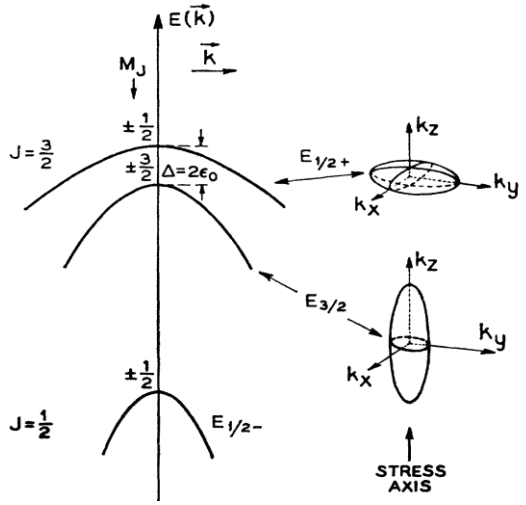

Figure 14: Under a compressive static stress parallel to [001] axis the valence bands of Si split and shift. For a tensile stress on the same direction the ordering of the bands would be reversed. The energy surfaces shown are a prolate and an oblate ellipsoids with [001] as symmetry axis. From [95].

To summarize, we learned from this section that the energy band structure of semiconductors is affected by temperature, free carrier density and stress and lattice vibrations. All those factors contribute to the band-gap renormalization at different critical points by inducing strain in the lattice, and in our case of particular importance are the reducing of critical point E_1 energy, which can bring our excitation with ~3.1 eV closer to resonance with the direct band-gap of Si, and the CBM, which will affect the mobility of carriers and therefore their diffusion, as explained in Chapter 5.

2.5 LO PHONON SELF-ENERGY

Raman spectra are characterized by their peak frequency, half-width and intensity. The half-width is proportional to dephasing rate of the phonon, and inversely proportional to its decay time. We are interested in how the frequency and dephasing rate of the LO phonon of Si behave when the lattice is subjected to different external factors. Both the phonon frequency and decay time change under the influence of the same factors that affect the band energy structure summarized in Subchapter 2.4. In Chapter 4, we will explain in the context of the experimental findings how the stress induced by the phonon itself and by both the dilation due to lattice temperature increase and the compression the lattice undergoes after excitation affect the phonon frequency and decay time. Recall that any strain applied to the lattice either weakens or stiffens the Si-Si bonds, depending on its nature. The change of the bonds length influence the frequency of the phonon, i.e., the atoms vibrate, respectively, at a lower or a higher frequency than if they were in an unstrained lattice. In this Subsection we review literature experimental results illustrating the influence of lattice temperature, strain and acoustic phonons on the LO phonon of Si.

2.5.1 Influence of lattice temperature on the LO phonon self-energy

The Raman spectral line shift and broadening with increasing lattice temperature were extensively investigated by many authors including Balkanski et al. [98], whose results are presented in Fig 15.

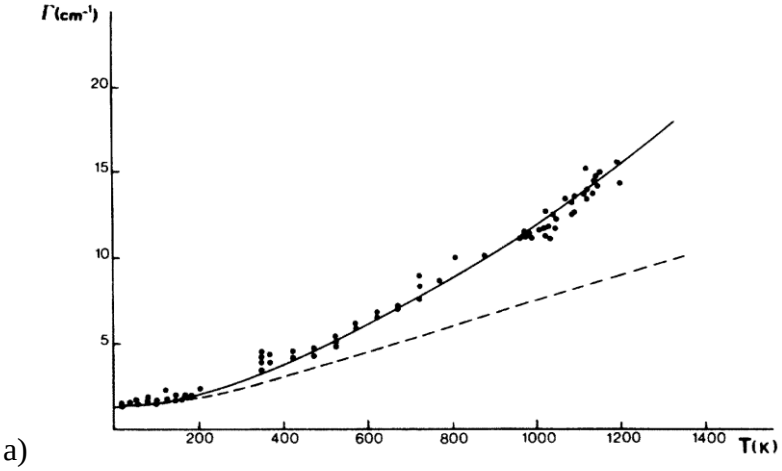

a)

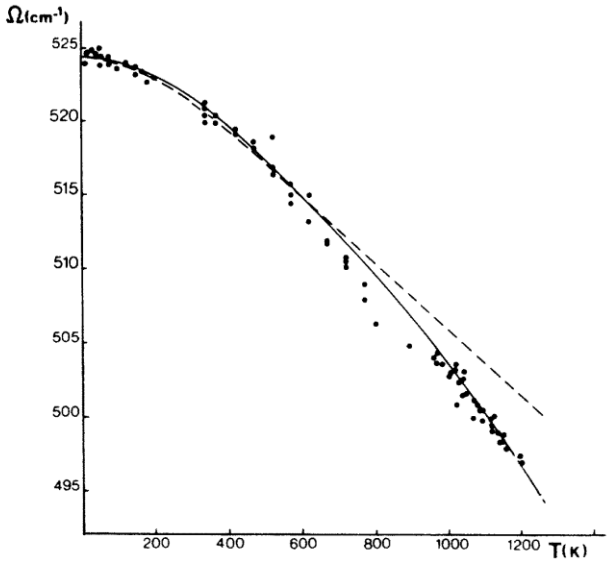

b)

Figure 15: Temperature dependence of the LO phonon a) dephasing rate, and b) frequency, for Si; fitting lines include 3-phonon (dashed) or 3- and 4-phonon interactions (solid). From [98].

The dashed curve in the Fig.15a is obtained from the equation

$$\Gamma(T) = \Gamma(0)\left[1 + \frac{2}{e^{x} - 1}\right], \qquad \text{Eq. 2.29}$$

where $x = \hbar\omega_0 / 2k_B T$ and $\Gamma(0) = 1.4\,\text{cm}^{-1}$, and only the decay of the LO phonon into two phonons is taken into account.

When the decay of phonon due to 3- and 4-phonon processes (one phonon decays into 2, respectively 3 phonons) is included, the equation Eq. 2.29 is modified as:

$$\Gamma(T) = A\left[1+\frac{2}{e^{x}-1}\right] + B\left[1+\frac{3}{e^{y}-1}+\frac{3}{(e^{y}-1)^{2}}\right], \qquad \text{Eq. 2.30}$$

where $y = \hbar\omega_0 / 3k_B T$, and A and B are constants. The solid line curve fit in Fig. 15a is obtained with $A = 1.295$ and $B = 0.105$ cm^{-1}.

In Fig. 15b are presented the experimental shift of Raman frequency with the lattice temperature. The solid line curve is obtained by fitting the experimental data with an expression including both 3- and 4-phonon processes:

$$\Omega(T) = \omega_0 + C\left[1+\frac{2}{e^{x}-1}\right] + D\left[1+\frac{3}{e^{y}-1}+\frac{3}{(e^{y}-1)^{2}}\right], \qquad \text{Eq. 2.31}$$

where $\omega_0 = 528$ cm^{-1}, $C = -2.96$ and $D = -0.174$ cm^{-1}. The dashed line is obtained only including the 3-phonon contribution. In this case the best fit requires $\omega_0 = 529$ cm^{-1} and $C = -4.24$ cm^{-1}, and the line agrees well with the data up to 600 K. It is clear that the solid line fits the data better for a wide range of temperatures, demonstrating the effect of the higher anharmonic decay contributions to both frequency and dephasing time of the phonon.

Recently, the dependence of the LO phonon of Si on temperature between 100 and 600 K was investigated for different doping densities by Huang et al. [99]. Their results show that the frequency varies roughly linearly with increasing temperature, with a doping density dependent slope (Fig. 16).

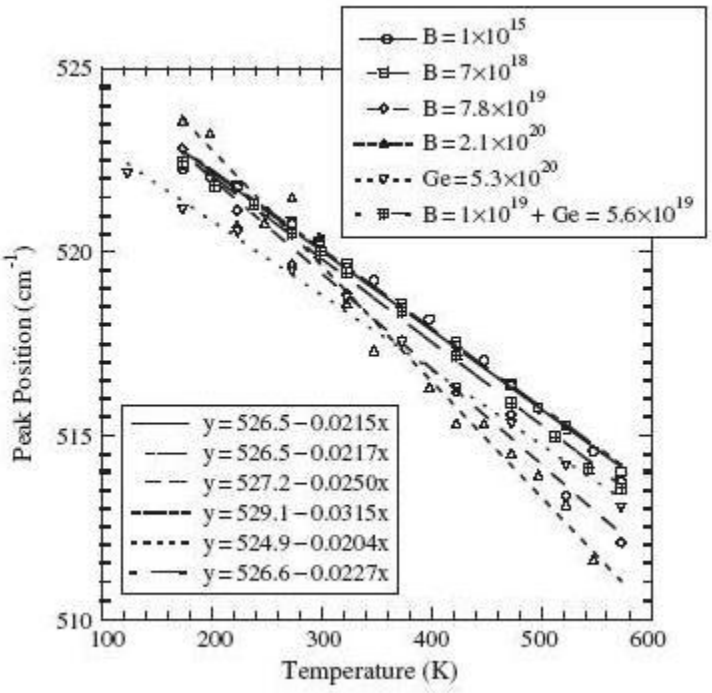

Figure 16: LO phonon frequency as a function of temperature, for different doping densities; from Ref. [99].

2.5.2 Influence of stress on the LO phonon frequency and decay time

If atoms in a lattice are brought closer together by compressive stress (compressive stress is the equivalent of positive pressure and of negative strain), the repulsive forces stiffen the force constant uniting the atoms, and the frequency with which the atoms vibrate increases. Hydrostatic pressure for example will increase the phonon frequency because as the interatomic distances decrease, the interatomic force constant increases ("stiffening"). A hydrostatic stress is the simplest form of stress and consists of isotropically compressing or pulling apart the crystal without changing its symmetry [100], and in the case of Si, the frequency of the zone-center optical phonon is shifted without splitting into components.

In the absence of any strain, the optical phonon branches of the diamond-type crystal at $q \approx 0$ are triply degenerate due to the cubic symmetry. A uniaxial stress reduces the symmetry, and splits and/or shift the Raman peak either into a singlet (with the eigenvector parallel to the stress direction) and a doublet (eigenvectors perpendicular to the stress) components [56]. If the stress is applied along [110] direction, the LO phonon splits into three components [101]. The shift in frequency is due to both the shear and hydrostatic components of the stress. The observed splitting and shifting of phonon lines that are determined by the choice of incident light polarization orientation with respect to the crystalline lattice, i.e., the effect can be analyzed using the polarization selection rules. Results for pressure applied in [100] or [111] in Si were reported by Cardona [102]. The frequency shift measured at various pressures for the doublet and the singlet peaks are presented in Fig. 17.

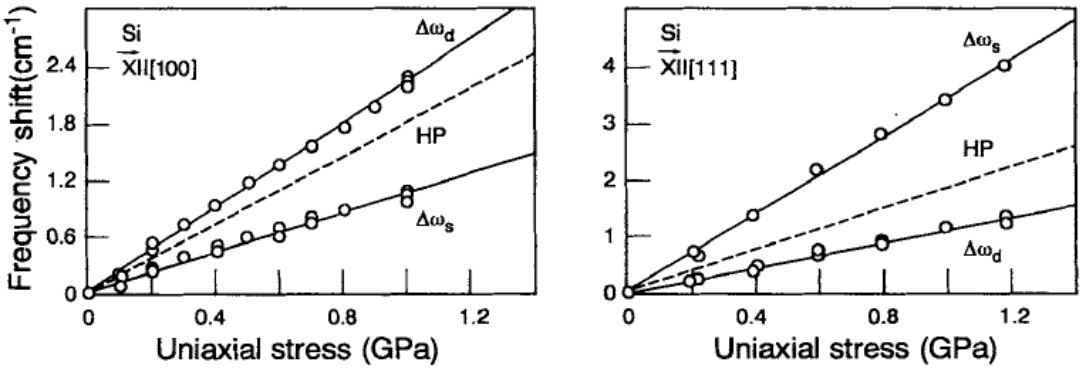

Figure 17: Influence of uniaxial stress on the optical phonons of Si, from [102]. Note that for stress along [100] direction the doublet (d) and the singlet (s) are shifted oppositely than for stress along [111]. HP denotes the shift induced by the hydrostatic component of the stress.

Cradona [102] pointed out the interesting observation that the frequency of the singlet decreases under compression along [100], although it is expected to increase, as it does in the case of stress along [111]. This was explained by the fact that the stress does not change the bond lengths, but rather changes the angle of the bonds with respect to the [100] axis.

The information reviewed in this chapter will be relevant to explain the experimental results we present in Section 4.1.2, in which quite few factors act on the excited lattice of Si inducing stress, and renormalizing the coherent LO phonon self-energy. Summarizing, we reviewed the impact of strain on a semiconductor, which is important because of its effects on the band structure and on the phonon modes. We also reviewed the influence of the lattice temperature, which acts like a strain upon the lattice, producing dilation and softening of the bonds. Free carriers influence also the LO phonon frequency, as it was shown in Section 2.3.1. The presence of photoexcited electrons along a bond will screen the repulsion between atoms in the same way as free carriers introduced by doping: the bond softens and the frequency of the atomic vibration decreases.

2.6 PHOTOSTRICTIVE EFFECT

Our experimental results in Section 4.1.2, obtained by measuring the transient reflectivity of Si with electro-optic sampling (EOS) technique, show the changes of the self-energy of the zone-center LO phonon. These changes in phonon frequency and dephasing time display a complicated dependency on the time delay between excitation of the sample and measurement of the reflectivity, being renormalized through carrier-phonon interactions, dilation due to lattice temperature increase, etc. In this Section we discuss another effect relevant to our work on Si: the photostriction.

2.6.1 Photostriction in Si

Stress on semiconductors can also appear by exciting carriers through sudden illumination with an ultrashort pulse [33, 103-106], because the presence of excited carriers changes the total energy of the crystal. In exchange, the crystal volume changes while the energy is minimized. This effect is known as the "electronic volume" ("photostrictive" if the volume contracts) effect, and the strain produced by the carriers as "electronic strain". We review this particular factor of stress because it can lead to the blue shift of the coherent phonon frequency, which we observe 2-3 ps after the samples were excited (Subchapter 4.2). It seems, therefore, that the presence of the optically injected carriers not only induces a red-shift of the LO phonon frequency through electron-phonon coupling, but it can also induce a blue-shift of the phonon by creating a dynamic strain. This strain is usually measured indirectly, by relating it to the acoustic pulse that it generates. Wright and Gusev [103] observed the optically induced surface contraction in Si by ultrafast beam deflection method. They used a 630 nm, 200 fs pulse to photoexcite a carrier density of maximum $6\times10^{18}\,\mathrm{cm}^{-3}$. Their result shows evidence that photoexcitation induces an isotropic compressive stress in Si. Because of the geometry of excitation (light is deposited in a thin surface region over much broader surface area), an acoustic wave that propagates perpendicular to the surface can be generated. The diffusion equation governing the motion of the generated acoustic phonon is given by ref 1 as:

$$\rho\frac{\partial^2 u}{\partial t^2}=\rho v^2\frac{\partial^2 u}{\partial z^2}+B\frac{\partial E_g}{\partial p}\frac{\partial N}{\partial z}+3B\beta\frac{\partial T}{\partial z}, \qquad \text{Eq. 2.32}$$

where u is the acoustic displacement along the normal to the surface (z direction), v the longitudinal sound velocity, B the bulk modulus, β the thermal expansion coefficient, N the

carrier density, T the temperature of the lattice and $\frac{\partial E_g}{\partial p}$ is the coefficient of change of the band-gap energy by applied pressure.

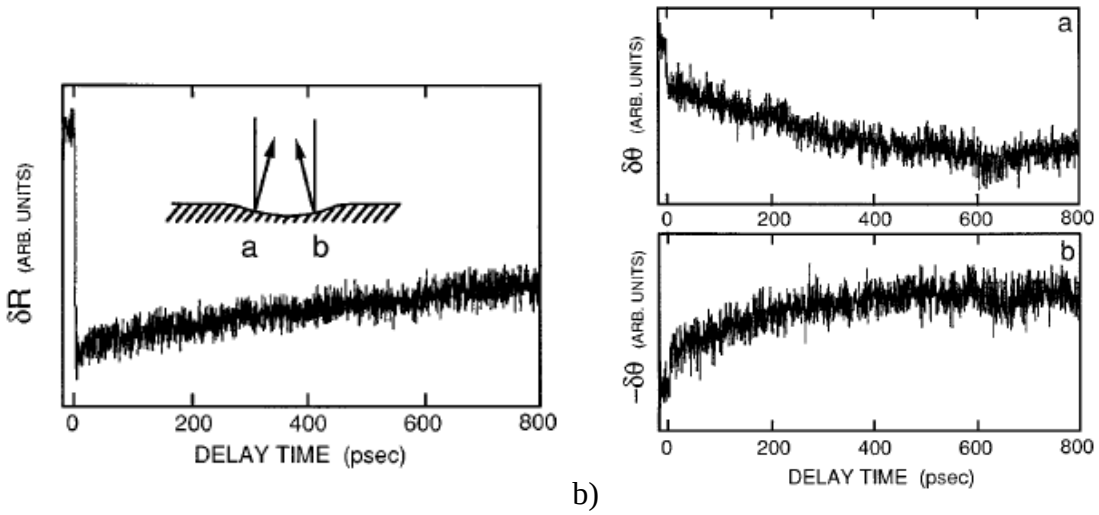

a) b)

Figure 18: a) transient reflectivity change vs. time delay for Si; inset shows the bending of the sample at the spot where the pump pulse hits the surface of the sample; b) angular deflection of the probe beam on the a and b sides of the pump spot showing the change in surface bending with delay time. From [103].

In Fig. 18 are presented the experimental results of Wright and Gusev showing the change in transient reflectivity with time (a), where the probe pulse is concentric with the pump pulse and the combined signal of a split photodiode records the reflectance from the sample, and the probe beam deflection (b) when the probe pulse is displaced from the center of the pump pulse and the two channels of a split photodiode detect the deflection of the reflected beam by the surface contraction in response to the pump pulse. It is clear that the surface recovers from the electronically induced compressive strain over a period of time much longer than the time delay we scan (6 ps).

It is important to note that in diamond structure semiconductors the coefficient $\frac{\partial E_g}{\partial p}$, which determines whether a lattice will contract or expand when electron-hole pairs are

introduced by photoexcitation, is positive for L-valley electrons and negative for X-valley electrons. Therefore Ge, which has conduction band minimum in the L-valleys, expands [104, 105] and Si, which has conduction band minimum in the X-valleys, contracts upon band gap excitation [33, 105]. In the case of 400 nm excitation of Si, however, the L-valley conductions bands in Si are populated initially, and on subpicosecond time scale L-to X-valley transfer occurs. Therefore we expect that Si expands upon initial excitation, and on sub-picosecond timescale it starts to contract. This dilation followed by contraction of the lattice creates an acoustic phonon pulse, which propagates from the photoexcited region into the sample bulk. This could explain the blue shift we see in our results and will be detailed in Section 4.1.2.

3.0 EXPERIMENTAL APPARATUS

In this chapter we introduce the experimental apparatus for transient reflectivity measurements on Si. The apparatus includes a self-made Ti:Sapphire femtosecond laser oscillator, a second harmonic generation (SHG) module for converting the fundamental output of the oscillator from 800 nm to 400 nm, a pump-and-probe module for transient reflectivity measurements, electronics for signal measurement and processing, and a Mach-Zehnder interferometer for delay time axis calibration.

3.1 TI: SAPPHIRE LASER

Pulsed lasers enable excitation of carriers and measurement of subsequent carrier and lattice dynamics in solid-state systems. Ultrafast lasers delivering pulses as short as 5 fs were reported already in 1999 [107]. Such lasers permit the delivery of very intense electric fields and therefore the excitation of high-density non-equilibrium carrier distributions with deposition of low energies, which could otherwise destroy a sample. Titanium-doped sapphire (Ti^{3+}:Al_2O_3) is the most commonly used gain material for generating 10-100 fs duration mode-locked pulses, because of its wide gain bandwidth [108] and superior mechanical and thermal properties. The gain of Ti:Sapphire lasers peaks at about 800 nm. Moreover, its absorption band, which peaks at about 490 nm [109, 110], does not overlap the gain spectrum covering the spectral range from

650 to 1100 nm, thus avoiding light reabsorption and, consequently, power losses. The large bandwidth and therefore tuning range of Ti-Sapphire typically requires use of different mirror sets. The large optical bandwidth of Ti:Sapphire and the nearly instantaneous response of the Kerr effect in the gain medium make possible the generation of very short (<10 fs) laser pulses. An important step in the generation of subpicosecond pulses was the use of a prism-based compensation of the positive intracavity group delay dispersion (GDD) [111]. In this way, pulses as short as 10 fs could be achieved [112, 113]. Further decrease of the pulse duration was limited by the higher orders of dispersion introduced in part by the prisms themselves. The drawbacks of using ultrashort pulses produced with prism dispersion compensation included the decrease of the pulse quality (time-bandwidth product increase), and sensitivity of the pulse width to the cavity and prism alignment. These problems were partially overcome by the development of negative-dispersion (chirped) dielectric stack mirrors.

The self-made Ti:Sapphire laser oscillator cavity based on the design of Xu et al. [114] is depicted in Fig 19. A CW Nd:YVO_4 Millenia laser operating at 532 nm excites Ti:Sapphire gain medium with a typical power of 4.85 W. When optimized, this Ti:sapphire oscillator provides less than 10 fs duration, ~ 800 nm central wavelength pulse trains with a 70 MHz repetition rate. For the shortest pulse duration, the output power and the bandwidth are typically about 0.8 W and ~ 130 nm. The precise details of the laser operation depend on the alignment, dispersion compensation, temperature on the crystal, etc.

The pump beam is focused onto the gain crystal by a 6.5 cm focal length lens. Around the gain medium two concave folding mirrors with focal length of 3.5 cm collect the emission form the Ti:Sapphire crystal. The folding mirrors are dichroic, reflecting 800 nm and transmitting 532 nm. The crystal is cut into a parallelogram at the Brewster angle, with dimensions of 2.3 mm

optical pathlength and 1 mm thickness. Four of the cavity mirrors have a negative dispersion (ND) dielectric coating of ~ -60 fs^{-2} per bounce to compensate for the positive dispersion in the cavity.

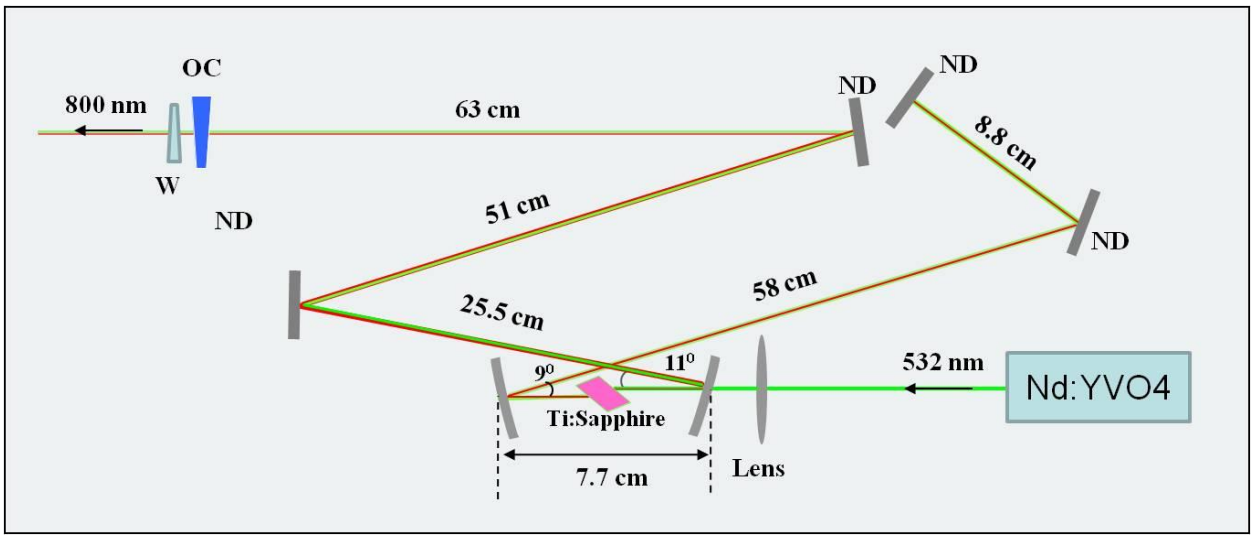

Figure 19: Ti:Sapphire laser cavity schematic (not at scale). ND labels denote the negative dispersion (chirped) mirrors, OC the output coupler.

The output coupler (OC) reflects 80% of the laser energy and transmits 20% that is used in the experiments. The OC is coated on a wedged substrate (5°). An identical antireflection coated quartz wedge oriented in the opposite direction to the OC is placed at the exit from the cavity. Translating the wedge into the beam pathe permits the fine adjustment of the total dispersion of the 800 nm pulse output. The idea behind dispersion tuning is to achieve the minimum 800 nm pulse duration and therefore peak intensity at the SHG crystal.

The whole cavity, less the pumping laser, is encased in a black anodized aluminum box covered with an orange Plexiglas lid. Holes are provided for the input pump and output pulse. This way the optics are shielded from dust or other particles and the air pressure is not subject to fluctuations.

The repetition rate of the oscillator (time between two consecutive pulses) is directly related to the time it takes a photon to travel twice through the whole cavity ($L = \frac{c}{2 \times repetition\ \ rate}$). Therefore, changing the length of the cavity permits the adjustment of the repetition rate. Our laser pulses have a repetition rate of 70 MHz, which corresponds to a cavity length of 2.14 m. Note that the cavity is asymmetric with respect to the path lengths on either side of the gain crystal. This is preferred for stable operation.

To set up such cavity for producing very short pulses requires high quality optics with properties suitable for the wavelength range of light involved, and very good alignment. The cavity geometry and mirrors were selected to optimize the pulse duration and output power. A pragmatic way to build up a cavity is to start with arranging the optics as close as possible to a configuration enabling lasing. One needs to ensure that the beam of the 532 nm pump laser and the fluorescent spots of the Ti:sapphire laser propagate at the same height above the optical table. Then, one needs to align the horizontal directions of the end mirrors so that the forward and backward traveling beams overlap each other. Finally, one should fine adjust the cavity for the quality of the lasing mode and output power, in order to create conditions for mode-locking. The first requirement of mode-locking is that inside the gain medium the green and red beams must spatially overlap. The second is to increase losses (detune the focusing) of the CW operation with respect to mode-locked operation. In our case a 300-400 mW CW beam will correspond to a 700-800 mW mode-locked beam. The third requirement is to keep adjusting the position of the optics and realign, until a stable cavity emitting sub-10 fs pulses is obtained. The forth requirement is to be patient and persevering. In Fig. 20 a typical spectrum of the fundamental output of our Ti:Sapphire oscillator shows almost no residual pump light. The daily routine of

laser usage and short description of optics cleaning and realignment method I employ are summarized in App. B.

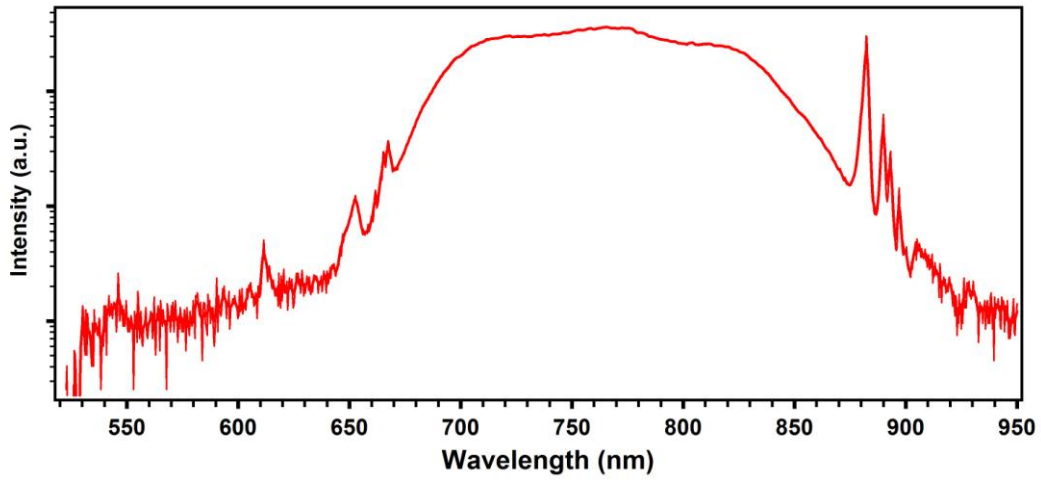

Figure 20: A logarithmic plot of a typical spectrum of the Ti:sapphire laser oscillator taken at 1 m distance from the cavity output coupler.

3.1.1 The mode-locking procedure

In the CW mode the Ti: Sapphire laser oscillates in a narrow range of wavelengths centered at the gain maximum of about $\lambda = 800$ nm (1.55 eV photon energy). The width of the frequency distribution and its amplitude depend on the gain medium, the population inversion, and the cavity alignment. In the cavity, light will oscillate on longitudinal modes satisfying the resonant condition $\nu_n = n\frac{c}{2L}$, n being the mode number and L the cavity length. CW output consists of several discrete frequencies spaced by an amount of $\Delta\nu_n = \frac{c}{2L}$, with the phase of each mode randomly distributed. While the laser oscillator can support all the wavelengths for which the relation $\lambda = \frac{2L}{n}$ is satisfied, it lases only for those for which there is gain (650 to 1100 nm for

Ti:sapphire). To achieve intense mode-locked operation the lasing frequencies must be in phase periodically so that the individual waves can interfere constructively to produce a coherent burst of light. Therefore, a mode-locking mechanism is needed to force all of the frequencies to oscillate in phase for a brief instant within the photon round trip period through the cavity.

In the case of Ti:Sapphire oscillator, the gain crystal itself provides the mode-locking mechanism. This is due to the nonlinearity of its index of refraction, which increases as the optical intensity increases. Inside the resonant cavity, the transverse mode of a laser can be assumed to have a Gaussian intensity profile [115]. This will create a transverse Gaussian index of refraction profile inside the crystal, which acts on the light beam like a gradient index lens (Fig. 21), inducing a phase delay between the middle and the edges of the Gaussian beam.

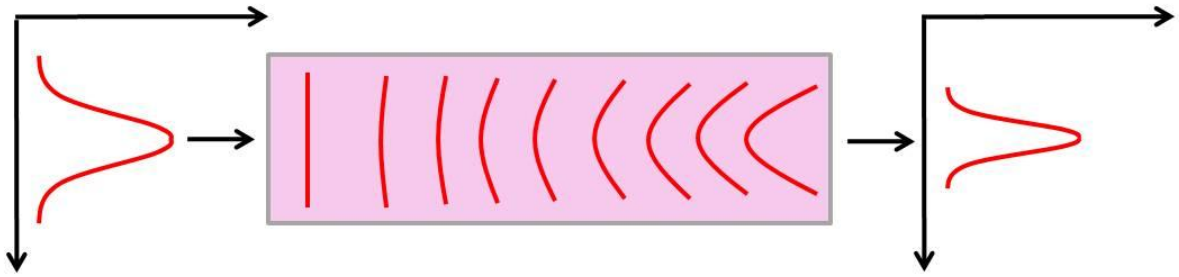

Figure 21: The self-focusing of an intense laser beam propagating through a Kerr medium. The red lines represent the intensity dependent nonlinear modulation of the phase front.

The transverse phase modulation of the beam results in its self-focusing. This nonlinear optical interaction is known as the Kerr effect, which is described by the third order nonlinear susceptibility. Disturbing the cavity, such as by taping one of the pump mirrors, induces power fluctuations, which are amplified with respect to the CW operation, because of the nonlinear lensing effect in the Kerr medium, to create a mode-locked pulse. By contrast to CW mode lasing, an ideal mode-locked (phased-locked) pulsed beam will have a broad frequency spectrum width, e.g., a Gaussian distribution of mode amplitudes and a fixed phase relationship among

them (Fig. 22). The frequency spacing between the cavity modes is $\Delta\nu_n = \frac{1}{\tau_R}$, where τ_R is the repetition rate.

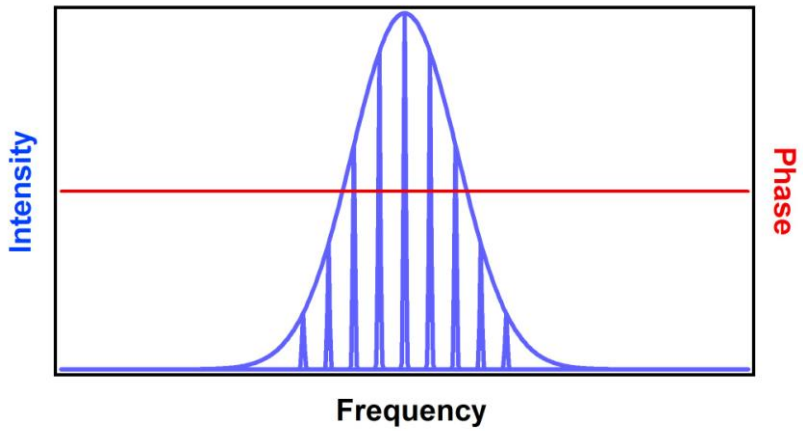

Figure 22: Schematic representation of a mode-locked pulse spectral intensity and phase. The single equally spaced lines are individual cavity modes, which oscillate with the same phase.

The number of modes that are oscillating in phase *n* and the mode interval $\Delta\nu_n$ give the frequency bandwidth through $\Delta\nu = n\Delta\nu_n$. The mode-locked pulse duration is determined by the energy-time uncertainty and therefore is inversely proportional to the number of modes that can be mode-locked. The broader the pulse bandwidth, the shorter the pulse duration.

3.1.2 Pulse duration

Knowing the duration of the pulses is a requirement in any pump and probe experiment, as the dynamical processes to be measured requires comparable or shorter pulse duration. We can theoretically estimate the duration of a pulse according to the following procedure. The relation between the frequency bandwidth $\Delta\nu$ and the temporal pulse width T_p is given by the uncertainty product

$$\Delta\nu \times T_p \geq C\,, \qquad \text{Eq. 3.1}$$

where the dimensionless constant C is 0.441 for a Gaussian pulse, and 0.315 for a hyperbolic secant pulse [116]. For pulses emitted by mode-locked lasers, the solution of the wave propagation equation through the oscillator (nonlinear Schrödinger equation, including dispersion terms) has a hyperbolic secant form [117]. The bandwidth of a pulse is given by:

$$\Delta\nu = c\ \Delta\left(\frac{1}{\lambda}\right) = c\left(\frac{\Delta\lambda}{\lambda_1\lambda_2}\right), \qquad \text{Eq. 3.2}$$

where c is speed of light and $\Delta\lambda = \lambda_2 - \lambda_1$ is the spectral width of the pulse.

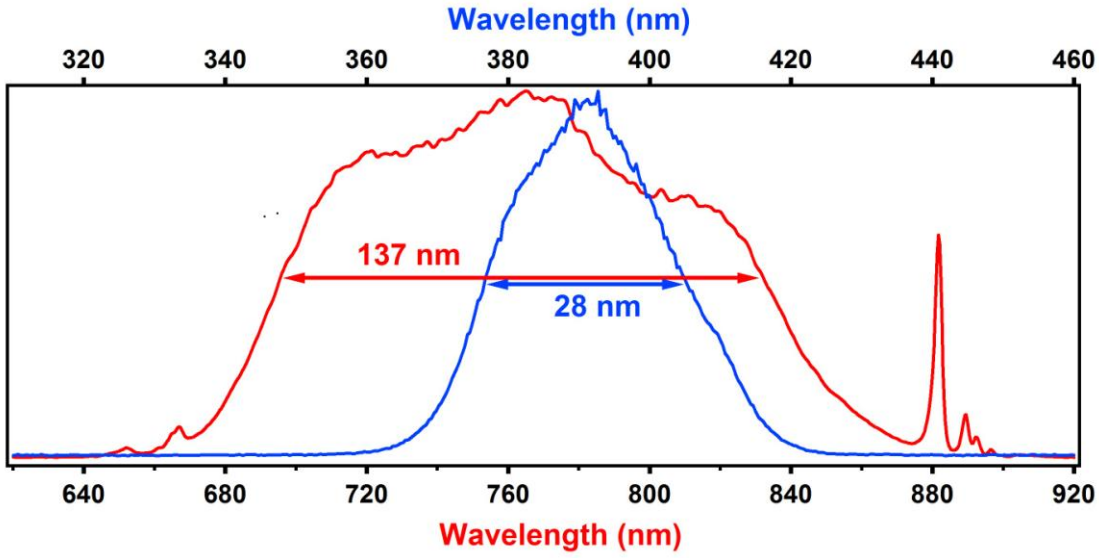

Figure 23: (red) Typical pulse spectrum generated by the self-made Ti:sapphire laser oscillator. (blue) The second harmonic (SH) spectrum obtained by frequency doubling the fundamental pulse.

If we apply these relations to a typical pulse emitted by our oscillator (Fig. 23) with $\lambda_1 = 695$ nm and $\lambda_2 = 833$ nm, i.e. HWHM of 137 nm, and assuming for simplicity that the pulse has Gaussian shape, its duration could be theoretically as short as $T_p \geq 2\frac{C}{c}\frac{\lambda_1\lambda_2}{\Delta\lambda} \approx 6.34$ fs; assuming the pulse to have a hyperbolic secant shape, its duration could be 8.88 fs.

The actual pulse spectrum and duration depend on the optimization of the dispersion within the cavity. The pulse duration at any position in the optical set-up will be determined by the total dispersion contributed by the optics and air in the optical path the pulse encounters within and outside the cavity up to that position. The pulse shape, in practice, is neither a perfect Gaussian, nor a hyperbolic secant, as can be deduce from spectra in Fig. 23, which deviates from an ideal shape.

3.2 SHG MODULE AND DISPERSION COMPENSATION

After emerging from the laser, the oscillator output passes through a negative dispersion stage consisting of 4 ND mirrors. These mirrors ensure the minimum pulse duration at the SHG crystal. The Second Harmonic Generation (SHG) module (Fig. 24a) consists of two concave dielectric mirrors with 5 cm focal length and a type I β-Barium Borate (β-BaB_2O_4; BBO) crystal cut for frequency doubling the 800 nm light. The nonlinear BBO crystal was purchased from FUJIAN CASTECH CRYSTALS, INC. It is cut with a phase-matching angle θ of 29.2°, and its dimensions are $3\times5\times0.05$ mm^3. When properly adjusted, the SHG module converts ~25% of the fundamental light into the SH light. A typical spectrum of the SH light is shown in Fig. 23. In the SHG module, one of the mirrors focuses the incoming 800 nm light at nearly normal incidence into the crystal and the other collimates the outgoing SH light. All three optics are mounted on adjustable mounts to permit easy manipulation and fine alignment. The mounts are set on a custom made base firmly set on the optical table, and, for both safety purpose and shielding from damage, covered by a home-made black anodized box with a removable lid and

apertures for the incoming and outgoing beams. The mirror reflecting the SH beam permits also adjustment of the beam size at the sample.

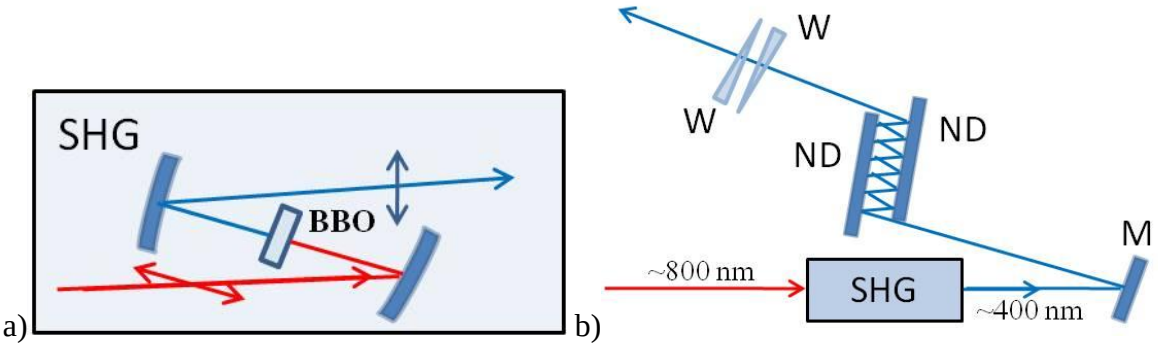

Figure 24: a) SHG diagram showing the BBO crystal and the polarization of light for the 800 nm (red) and 400 nm (blue) light generated in the BBO crystal; b) dispersion compensation optics: chirped mirrors (ND) and fused silica wedges (W).

To compensate for dispersion in the optical pathway for the 400 nm light, after the SHG module we add a pair of chirped mirrors (Fig. 24b). Each mirror introduces -20 fs^2 GDD (group delay dispersion) per reflection. Reflecting the frequency-doubled pulses from these mirror pairs n number of times introduces negative dispersion corresponding to discrete values of $2n \times 20$ fs^2. A pair of thin quartz wedges provides further continuously variable positive dispersion, which is adjusted together with the number of reflections from ND mirrors to achieve the shortest pulse at the sample.

3.3 PUMP AND PROBE SET-UP

The last part of our experimental apparatus is schematically presented in Fig. 25. The first optic of the module is a beam splitter (BS1), which divides the 400 nm beam into two parts. The intense transmitted part acts as the “pump”, and the weak reflected part acts as the “probe”.

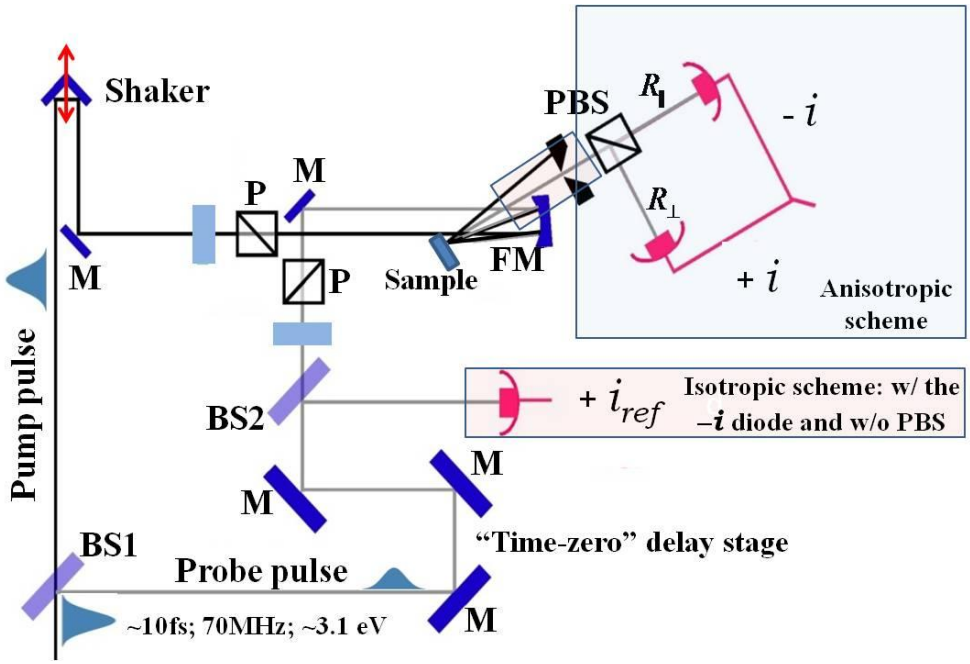

Figure 25: Schematic of the transient reflectivity measurement set-up. The blue square highlights the diodes needed for anisotropic set-up, while the rose ones, for isotropic set-up.

A manually adjustable delay stage placed in the path of the probe beam to define "time-zero", i.e., to make the optical paths equal so that the pulses temporally and spatially overlap at the sample. A rapid scanning (10-20 Hz) voice coil delay stage (shaker) incorporated into the pump beam path scans the optical path difference needed to induce a variable time delay between the pulses. We perform our measurements with the shaker working at 16 Hz with a time delay of about 6 ps. During experiments, the intensity and polarization of both pump and probe pulses are controlled by one half-wavelength wave plate ($\lambda/2$) and one polarizer (P) placed into the path of each beam. The polarizers define the polarization of each beam before the pump and probe beams are focused onto the sample. First the polarization is set for the appropriate experiment, and then $\lambda/2$ plate is rotated to adjust the amount of light transmitted through each polarizer. The pump and probe beams are rendered parallel to each other before being focused onto the sample by a concave mirror (FM) of 5 cm focal length. In order to minimize the focusing angle,

and therefore, the astigmatism associated with off-normal reflection by spherical mirrors, the beams are reflected very close to the edge of the focusing mirror. The surface of the sample is vertical with respect to the optical plane and tilted from normal reflection within the plane in order to direct the reflected probe beam into a photodiode detector. The angle between the incoming and reflected probe beams is made as small as possible in order to minimize the beam spot size on the sample. The pump reflection is blocked to avoid scattered pump light to reach the signal photodiodes.

For electro-optic sampling measurements, the reflected part of the probe is separated by a polarizing beamsplitter into perpendicular and parallel components. The two signals are recorded by identical photodiodes with an opposite bias to generate photocurrents with the opposite polarity ($i+$, $i-$). The two electrical signals are added in order to eliminate the laser amplitude fluctuations and the isotropic response of the sample. The anisotropic component of the signal is amplified, and the final result recorded by a digital oscilloscope. The amplification is provided in two stages: the resultant current from the diodes is amplified through Variable Gain High Speed Current Amplifier (Model DHPCA-100 from FEMTO, Berlin), after which the output is amplified through a low-noise voltage amplifier (Model SR560 from Stanford Research, Inc.). The main function of the second amplification stage is to filter the amplified signal using the variable low- and high-pass settings of the voltage amplifier.

3.4 TRANSIENT REFLECTIVITY MEASUREMENT

Pump-probe technique provides a general method for measuring the dependence of the reflectivity on the photoexcited charge carrier concentrations [118]. The pump excites the

sample, i.e. causes a change in the dielectric function, and the reflected probe "records" the perturbation through changes of its amplitude and/or polarization. By varying the delay between the pulses, it is possible to map out the temporal changes in the reflectivity.

In our experiments, three main factors contribute to the change in reflectivity: the non-thermal carrier population photoexcited at time delays <100 fs, the thermalized carrier population at later time delays, and the LO phonon oscillation. These components can be separated by different factors such as their time dependence, but also by how they influence the polarization of the reflected light. The processes which preserve the polarization of the reflected probe are "isotropic", while those that change its polarization are "anisotropic". The anisotropic, i.e., the electro-optic, set-up was described in the previous section. The signal recorded is proportional to the difference between the parallel and perpendicular components of the probe intensity, $\Delta R / R_0 = (\Delta R_{ll} - \Delta R_{\perp}) / R_0$. It contains, therefore, only the anisotropic contributions, i.e. those induced by the non-thermal high-density primary carrier distribution excited at time zero and by the modulation of the susceptibility in response to the coherent LO phonon oscillation; the slow contribution of the thermalized electronic population is isotropic. Because the isotropic contribution is the same for both polarization components of the probe, it is subtracted from the difference signal.

The transient reflectivity signals show the response of the sample according to the symmetries of $\Gamma_{25'}$ and Γ_{12} tensors. To probe the material response with these symmetries, the pump and probe polarizations are oriented with respect to the crystalline axes of the sample as shown in Fig. 26. In both configurations the polarization of the probe is rotated by 45° with respect to that of the pump; in the $\Gamma_{25'}$ configuration (Fig. 26a), the pump is polarized along the [110] crystalline axis of the sample, whereas in Γ_{12} configuration (Fig. 26b) the pump is along

[010] axis. The relative polarization of the pump with respect to the crystalline axes of the sample determines the photoexcited carrier distributions in the real and reciprocal spaces.

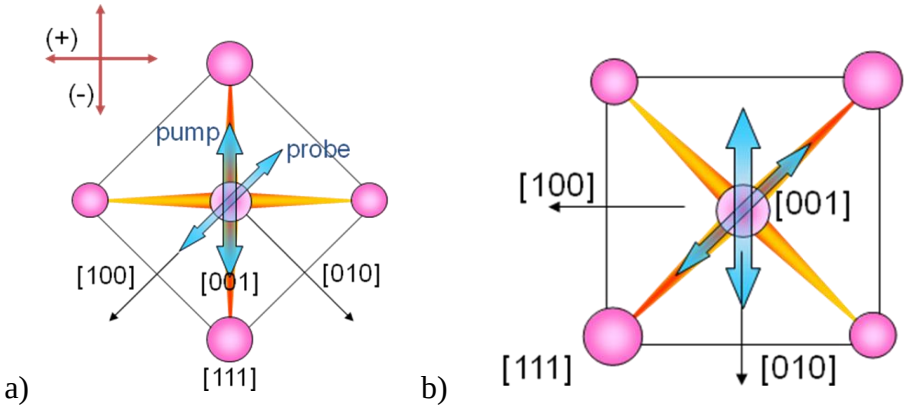

Figure 26: Pump and probe pulse polarizations with respect to the lattice of Si; a) $\Gamma_{25'}$ symmetry; b) Γ_{12} symmetry. (+) and (-) represent the bias of the diodes that record $R_{\perp}$ and R_{ll} .

A typical set of transient reflectivity data for pump powers varying from 15 to 64 mW, measured for n-Si (high doping density) with the Electro-Optic Sampling (EOS) technique is shown in Fig. 27. The initial response of the sample consists of a bipolar transient (negative drop followed by a positive overshot) in the reflectivity; this response corresponds to the coherent electronic currents generated by the pump and detected by the probe field. This aperiodic component is followed by an oscillatory component due to the change of the refractive index by the coherent zone-center phonon. The main focus of this thesis is on the oscillatory behavior. In addition to these coherent responses, closer inspection reveals an offset of the oscillatory signal, which is due to a small, slowly varying electronic signal. This residual signal is probably due to the incoherent charge current induced by the excitation (photo-Dember effect, arising from the ambipolar diffusion of the two types of curriers, which have different mobilities,,because of the fields created between them).

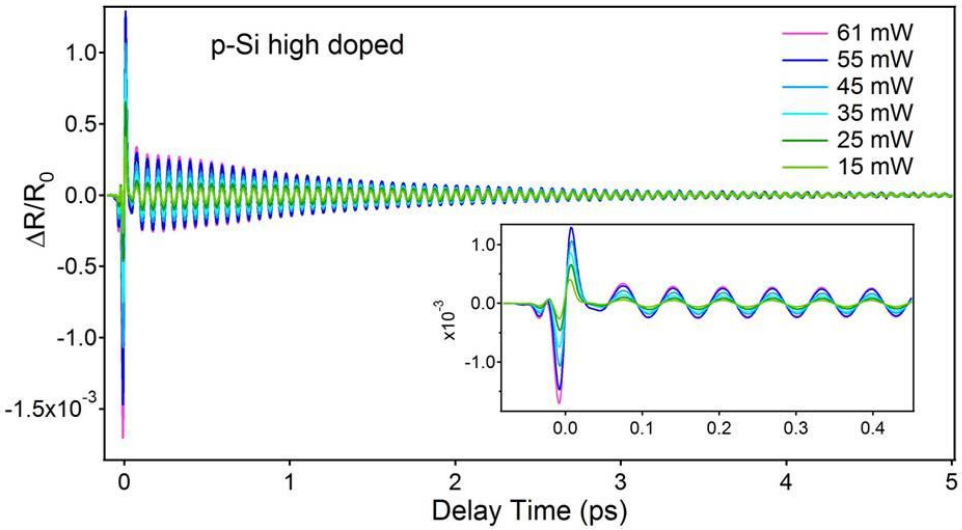

Figure 27: Transient reflectivity scans for highly doped p-Si, measured for the $\Gamma_{25'}$ symmetry for various pump power excitation; the inset shows data on an expanded time axis, to focus on the signal during the first 450 fs time delay.

For the isotropic scheme the set-up of the anisotropic experiment is slightly modified: the polarizing beam splitter is removed from the path of the reflected probe (see Fig. 25) and the total intensity of the reflected probe part is recorded by one of the diodes; a reference signal is recorded by another oppositely biased photodiode, which serves to reduce the laser amplitude fluctuations. As in the anisotropic case, the electric signals from the two diodes are added, and the resultant signal is amplified and recorded in the same way as for the anisotropic case. The isotropic detection includes both the nonthermal and isotropic contributions from the carriers, along with the phonon modulation of the susceptibility. Maximum amplitude of the oscillatory contribution to the transient reflectivity is obtained for the pump polarization parallel to the [110] crystalline direction, and the probe polarization rotated at 45° with respect to probe (Fig. 26). The transient reflectivity signal represents the averaged change in the dielectric function of Si over a volume defined by the area of the pump and probe pulses, and the irradiated depth of Si at the excitation wavelength (Fig. 28).

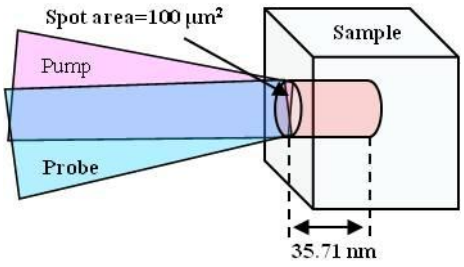

Figure 28: Schematic representation of the effective measured volume V (not to scale!)

In Fig. 27 it can be seen that the amplitude of time-resolved reflectivity signals depends on the pump power, i.e. the photoexcited carrier density. In order to evaluate the degree of excitation inside the sample, i.e. the carrier density generated inside the measuring volume, we need to estimate the size of the beam spot at the surface of the sample. The procedure and equipment necessary for this step are presented in Section 3.5. The index of refraction of Si is $n = 5.6$ at 400 nm wavelength. The thickness of the reflective layer is $\lambda/(2n) = 35.7$ nm. We measure the area of the sample on which the pump and probe are focused to be $A \approx 25\,\mu\text{m}^2$ (Section 3.5). The volume we probed is $\approx 0.925\ \mu\text{m}^3$.

In order to verify if the probe pulse power perturbs the measurements, transient reflectivity curves for different probe intensities while keeping the pump power at ~60 mW are recorded. The signal shows negligible change for probe powers between 2 mW and 5 mW [see Fig. 29]. Typical probe powers employed in the experiments are 3 mW.

For both anisotropic and isotropic measurements, the only non-negligible source of noise in the signal is from the residual power fluctuations of the laser, which could not be subtracted by the balanced double channel detection. To control this noise we average the signal over 3000-10,000 of sweeps. The number of sweeps is chosen to obtain an adequate signal-to-noise ratio at particular pump power.

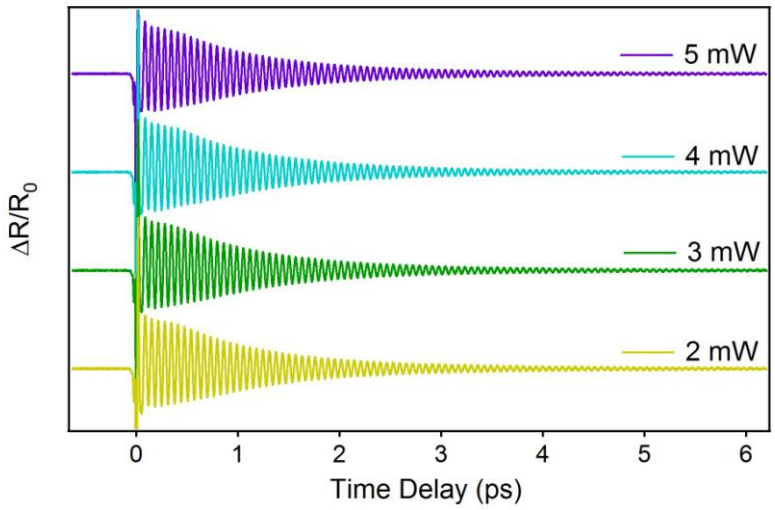

Figure 29: Transient reflectivity scans recorded for different probe pulse powers 2 to 5 mW.

3.4.1 Sources affecting the transient reflectivity: pulse chirp

Pulse duration influences the amplitude of the coherent phonons, and therefore the amplitude of the oscillatory contribution to the transient reflectivity. Also the chirp influences the initial phase of the oscillation. Transient reflectivity data obtained with our set-up, which qualitatively show the change due to the chirp of the amplitude and phase of the coherent LO phonon, are presented in Fig 3.18. For maximum amplitude of the oscillatory contribution to the reflectivity change the pulses should not be chirped at the sample. The chirp is adjusted by careful compensation of the positive dispersion in the optical pathway with the negative dispersion from mirrors M1 and M2. The positive dispersion is continuously varied by adjusting the insertion of the pair of fused silica wedges into the optical beam path, as described in section 3.2 (Fig. 24).

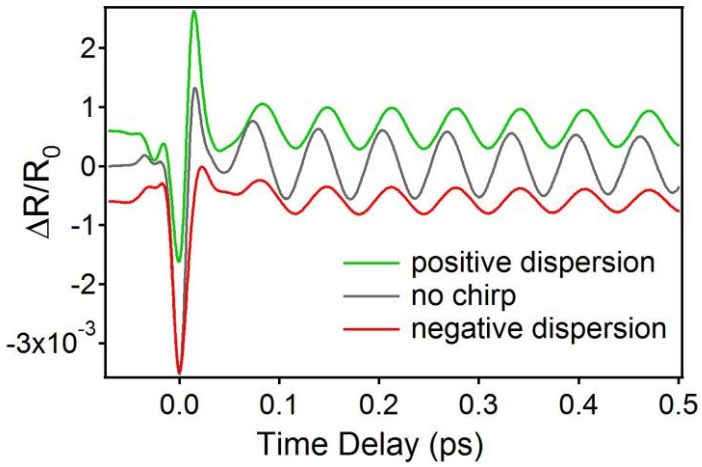

Figure 30: Transient reflectivity measured for positive chirp, negative chirp and zero chirp of the excitation pulse.

The experiments are performed for dispersion that gives maximum LO phonon signal; this condition refers to "no chirp" in Fig. 30. The influence of the linear chirp of a pulse on the coherent phonon amplitude was also found experimentally for Te; for both positive and negative chirp the amplitude of the phonon decreases, the larger effect being given by the positive chirp [119, 120].

3.5 BEAM SIZE AT THE SURFACE OF THE SAMPLE

There are several methods that can be employed for measuring the spot size of a Gaussian beam. Usually they consist of scanning opaque objects across the beam and observing the change in its transmitted power. If two mutually perpendicular directions are scanned, than one can define the shape and size of the transverse profile of the beam.

We use the "knife-edge" method. The transverse intensity profile of a Gaussian beam (TEM_{00} mode) with a beam waist w_0 power P_0 is described by [121]:

$$I(x,y)=\frac{2P_0}{\pi w_0}\exp\left(-\frac{2x^2+2y^2}{w_0^2}\right). \qquad \text{Eq. 3.3}$$

A sharp edged object moving in a direction x perpendicular to the beam path gradually blocks it and modifies its power profile according to:

$$P(x)=\frac{1}{2}P_0\,erfc\left(\frac{\sqrt{2}\,x}{w_0}\right). \qquad \text{Eq. 3.4}$$

The waist of the beam is estimated by fitting the recorded power profile with Eq. 3.4, letting w_0 and P_0 to be fit parameters. Note that the derivative of the power profile represents the actual beam intensity profile, which can be fitted to a Gaussian; the Gaussian waist, taken at $1/e$ of the height, gives the waist of the beam [107].

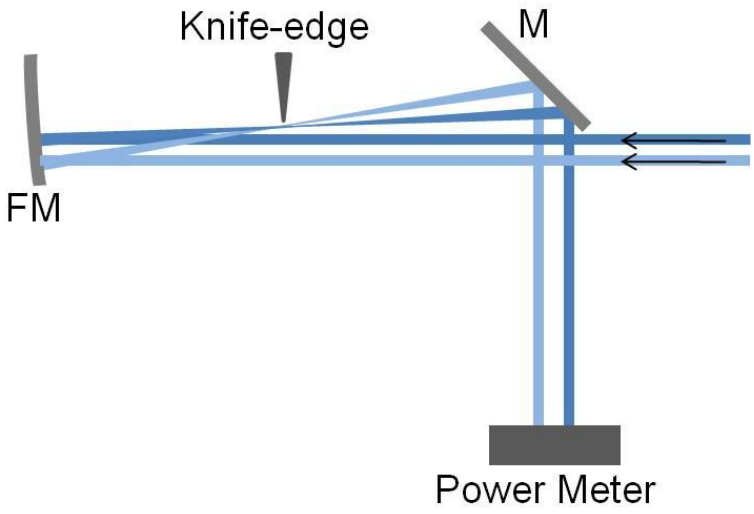

Figure 31: The "razor-edge" set-up (not at scale) for measurement of the laser beam focus.

For measurements, we used a razor placed at the position of the sample, transverse to the propagation direction of the beam. A high-resolution micrometer translated the razor edge into the beam. To locate the spot position, we visually estimated where the beams focused, positioned the razor very close to that point on one of its sides, and measured beam power profiles for various positions while approaching the spot, and continuing until the razor was on the opposite

side of the spot. The spot position corresponded to the smallest waist measured for the transverse profile of the beams. The power profile of the beam was recorded with a power-meter placed as in Fig. 31. Horizontal (x-direction, parallel to the optics table) and vertical (y-direction) measurements were performed. The power profiles were fitted to Eq. 3.4 and the fitting curves shown in Fig 32. The waist of the beam in the x-direction was found to be $a = 5\,\mu\text{m}$, and, in y-direction, $b = 6.5\,\mu\text{m}$. The spot is an ellipse with area A given by $\pi \times \left(\frac{a}{2}\right) \times \left(\frac{b}{2}\right) \approx 25\ \mu\text{m}^2$.

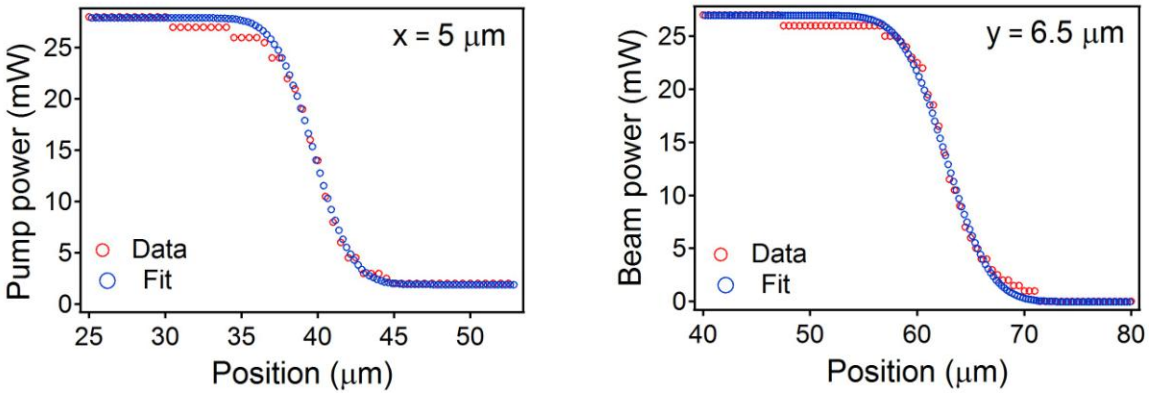

Figure 32: Knife-edge measurements: transmitted beam intensity versus razor's edge blocking distance for horizontal (left) and vertical (right) dimensions; data are fitted to Eq. 3.3.

3.6 DATA ANALYSIS: RETRIEVING THE LO PHONON FREQUENCY AND DEPHASING TIME VS. TIME DELAY

A major interest in this work is to estimate the change of LO phonon frequency and dephasing time as a function of the time delay between the pump and probe pulses. The LO

phonon frequency dependence on the delay time is extracted by multiplying the reflectivity signal with a 200 fs width Gaussian "window" scanned along the delay time interval in steps of 75 fs, and taking the peak frequency of the Fourier spectra of the resulting "wave-packets". In Fig. 33 the oscillatory part of a typical reflectivity data curve is shown together with a set of Gaussian windows. Their full-width at half maximum of 200 fs ensures that the "wave-packets" contain sufficient number of oscillations to return a meaningful result. The time zero response due to the broad frequency bandwidth electronic signal was removed from the signal in order to minimize deviations of the frequency spectra from the Gaussian form due to the non-oscillatory components in the time domain.

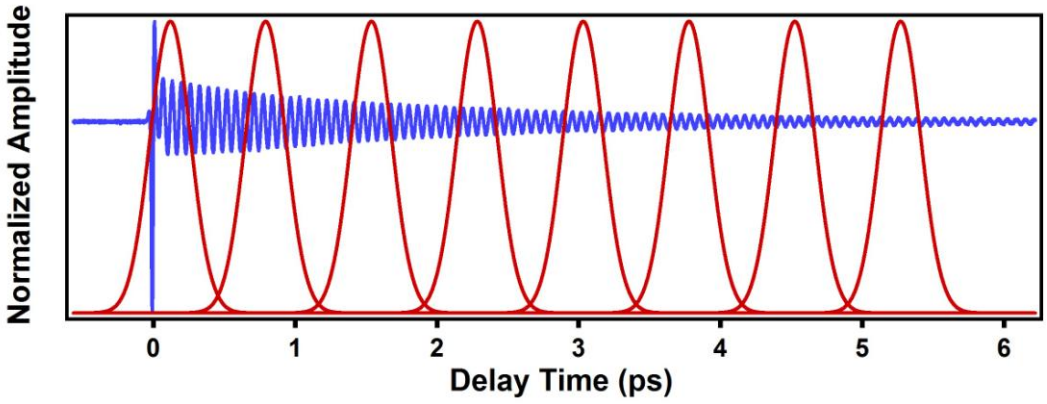

Figure 33: Temporal positions of the Gaussian window used for retrieving the LO phonon frequency as a function of delay time.

A set of "wave-packets" (centered at 0.75 ps, 2.55 ps and 4.95 ps) obtained by Gaussian windowing is presented in Fig. 34, together with their Fourier spectra fitted to Lorentzians. At 0.75 ps, the fit has a residual of about 1%. The shape of the FT of the "wave-packets" centered at earlier times is distorted due to the discontinuity of the oscillation at zero delay time.

The shape of the FT of the "wave-packets" centered at earlier times is distorted due to the discontinuity of the oscillation at zero delay time.

In this case the LO frequency corresponding to each Gaussian "window" is obtained by averaging the frequencies obtained for 20 "wave-packets" constructed by "sliding" the reflectivity signal over the first oscillation in 20 steps (dividing the first oscillation in 20 parts, removing a part at a time and taking the corresponding peak value of the LO phonon spectra each time). This avoids unphysical frequency shifts associated with a particular position of the Gaussian window.

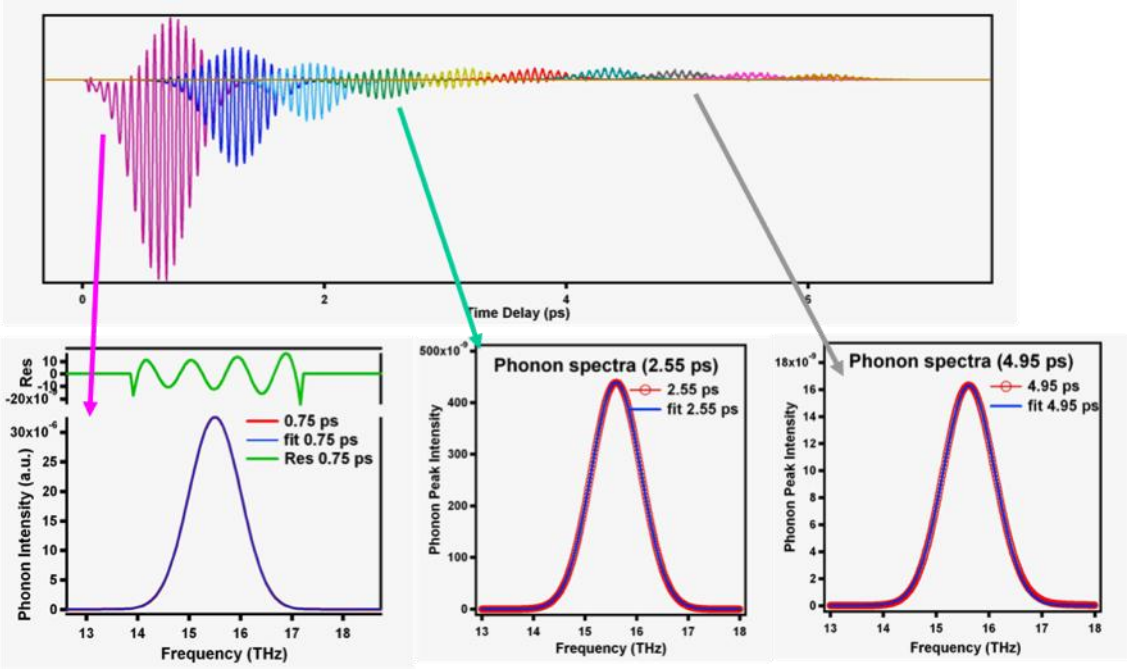

Figure 34: "Wave-packets" obtained by multiplying the experimental data with a shifting Gaussian function. Their FTs show good Lorentzian fitting.

The dephasing rate of the LO phonon is evaluated from the damping, i.e., the amplitude change with delay time, of the transient reflectivity oscillatory component, after separating it from the residual slow electronic contributions. The envelopes (E) of the oscillations are related to the time delay t and the LO phonon dephasing time τ through the approximate relation $E \approx Ae^{-\frac{t}{\tau}}$, where A is the time-zero value E. The relation between the envelope of the transient

reflectivity oscillation and the LO phonon dephasing time $\tau(t)$ is time dependent and given therefore by $\tau(t) = \dfrac{t}{\log(A) - \log(E)}$.

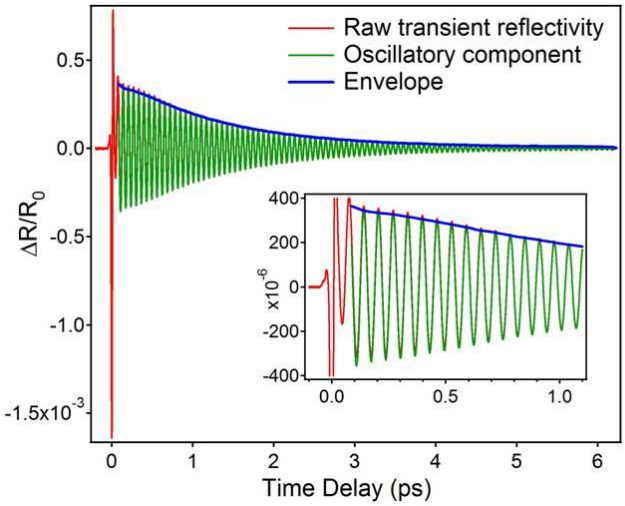

Figure 35: Typical transient reflectivity signal and its oscillatory part for 50 mW pump excitation, with the envelope blue.

In Fig. 35 is shown the oscillatory contribution (green) to transient reflectivity of p-Si (red), measured at 50 mW pump power, together with its upper (blue) envelope. It can be seen in both graphs of Fig. 35 that the oscillation amplitude has a "saturation" tendency at early times. This is not actual saturation of the signal, because it appears also at lower excitation powers and is independent of the amplifier gain, but probably arises from the evolution of the anisotropic electron distribution at the early times, as will be explained further. Also the oscillatory part (and the envelope) is slightly down-shifted from the transient signal at early times, due to eliminating the slow varying signal superimposed on the reflectivity signal. To evaluate the time-zero amplitude of the oscillation, we extrapolate the envelope using a "model" function constructed by fitting the well-behaved part of the envelope with any combination of exponentials that return the best fit.

3.6.1 Time axis calibration

The shaker providing the delay between the pump and the probe pulses requires calibration to obtain the correct time axis for the transient signal, hence meaningful results. The calibration is performed with a Mach-Zehnder Interferometer (MZI), which incorporates the delay stage (Fig.36), and is obtained from interference measurements of a He-Ne laser which, when scanned, produces a sinusoidal fringe pattern.

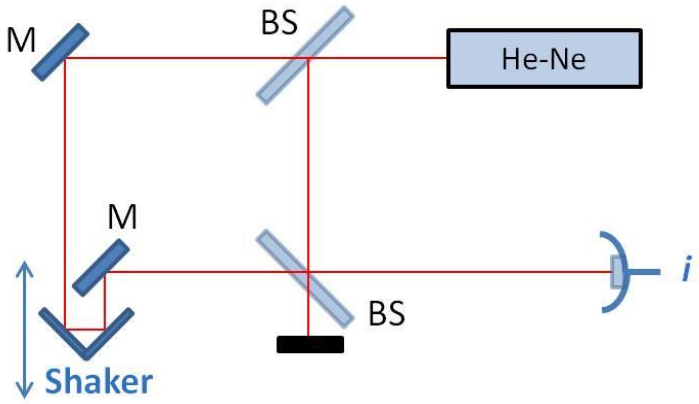

Figure 36: Mach-Zender interferometer incorporating the delay stage (shaker).

Scanning the delay stage generates a sinusoidal interference measurement of a He-Ne laser. The fringes oscillate with the He-Ne light frequency of 6328 Å. Knowing the period of the reference light, we get information about the nonlinearity of the delay stage by retrieving the "zero-crossings" (the value of data points that corresponds to each half of a total oscillation) throughout the time delay interval scanned, using the Igor Pro rutine presented in Annex D, which was developed by Kunie Ishioka and Albert Heberle. In Fig. 37a an interference pattern of the He-Ne light is shown together with the raw transient reflectivity signal to be calibrated.

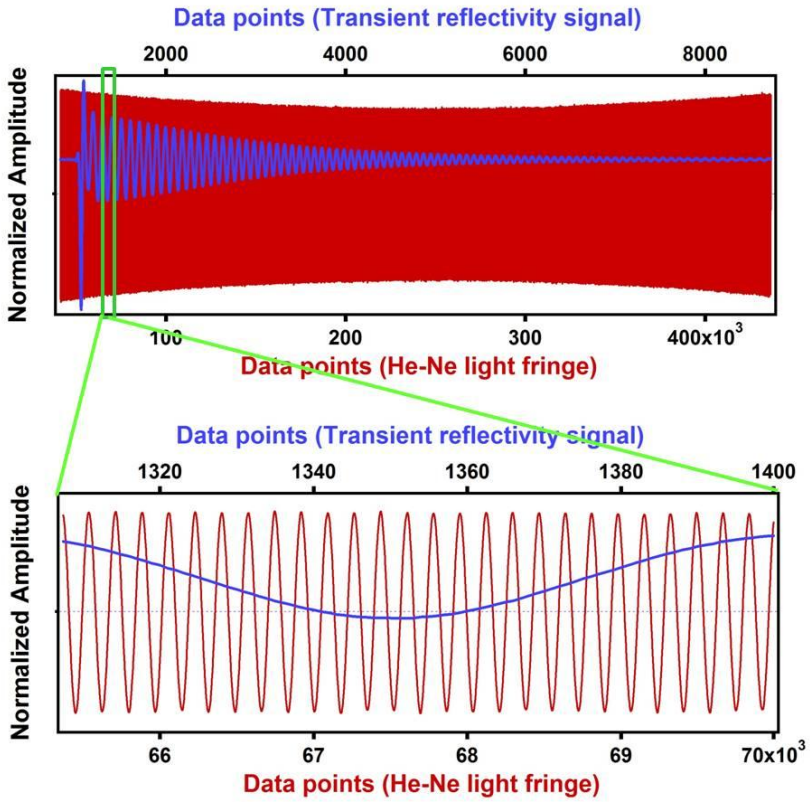

Figure 37: Calibration fringes (red) together and raw transient reflectivity data (blue) for the entire time delay interval scanned, and detail showing the second oscillation of the LO phonon.

In Fig. 37b the zero-crossings are shown (blue) for 225 fs time interval. From the zero-crossings we obtain a time curve (App. D) with which the transient signal is interpolated. Note that it is essential for both the transient data and interference fringes to be recorded with the scan delay performing under identical conditions so that the path scanned by the delay is the same for both measurements.

4.0 EXPERIMENTAL RESULTS

In this chapter we present the experimental results on transient reflectivity measurements on Si, as well as the results of our data analysis in conjunction with the numerical calculation presented in Chapter 5. The experiments to be described are transient reflectivity and electro-optic sampling pump-and-probe experiments in which the change in reflectivity is measured for various excitation pulse fluencies (i.e., pump pulse powers), for different pump and probe polarization angular rotations with respect to the sample crystalline axes, and different excitation light wavelengths.

The main results shown in this Chapter are the ultrafast formation of a quasiparticle (LO phonon "dressed" by elementary electronic excitations [122]) with renormalized self-energy after photoexcitation of the lattice (Subchapter 4.1), the evolution of its self-energy with time delay (Subchapter 4.2), and the interplay between the ISRS and DECP mechanisms in the generation of the LO phonon (Subchapters 4.3 and 4.4). All of those results are consequences of the interaction between photoexcited carriers and coherent LO phonons. The carrier-LO phonon coupling manifests itself through two main effects: the change in self-energy of both excitations involved, and the interference between the electronic and lattice responses to the pump pulse (Fano interference). The electronic self-energy change through phonon scattering manifests itself in the modulation of the band gap at the phonon frequency (see Sections 2.41 and 2.4.4). This modulation is primarily responsible for the observation of coherent phonon oscillations in the

transient reflectivity measurements. The change of the LO phonon self-energy manifests through frequency shifts and line broadenings. The Fano effect [123, 124] arises through the excitation of coherent phonons through the Raman tensor and electronic charge density fluctuations, combined with the residual electron-phonon interaction. It manifests itself through an asymmetry in the lineshape of LO phonon embedded in a continuous electronic response [28, 124-126]. This effect is discussed in detail in Subchapter 4.4.

4.1 STUDY OF COHERENT LO PHONON "DRESSED" WITH ELEMENRATY EXCITATIONS

In this section we describe the lattice response of Si(001) to excitation by 10 fs laser pulses by examining the transient reflectivity signals recorded for various pump pulse intensities. The transient reflectivity signals show a nearly instantaneous electronic response followed by an oscillatory component with frequency corresponding to the LO phonon of Si. The oscillation is due to the coherent LO phonons generated through the interaction of the light pulse with the lattice via second-order nonlinearity. Results based on this work were published [127] and presented at the 4th USD Conference, 2003.

4.1.1 Experimental results

The anisotropic transient reflectivity of Si(001) was measured by electro-optic sampling (EOS) method for pump powers from 5 to 40 mW. The experimental set-up and technique are described

in Sections 3.3 and 3.4. The four Si samples measured are n- and p-type doped with both low and high doping amounts (Table 2).

Table 2: Samples specifications.

Sample	Type	Resistivity (Ω cm)	Doping density (cm^{-3})
p-high doped	p-Si (001)	0.03	1.4×10^{18}
p-low doped	p-Si (001)	>10	$<1.3 \times 10^{15}$
n-high doped	n-Si (001)	0.005	1.2×10^{19}
n-low doped	n-Si (001)	<10	$<4.4 \times 10^{14}$

In an anisotropic measurement, only the off-diagonal components of the Raman tensor are sampled because of the choice of the orientation of the pump and probe pulse polarizations (see Section 3.4) with respect to the crystalline lattice [128].

$$\frac{R_{\perp}(\tau) - R_{ll}(\tau)}{R_0} = \frac{\Delta R_{eo}(\tau)}{R_0} \approx P^{(2)}_{001}(\tau). \qquad \text{Eq. 4.1}$$

The recorded signal expressed by Eq. 4.1 represents the change in reflectivity due to the effects induced by the pump pulse in the sample, normalized to the reflectivity of the sample in the absence of excitation.

The complex macroscopic second-order polarization induced by the pump pulse inside the sample is given by:

$$P^{(2)}_j(\tau) = {}^{S}\chi^{(2)}_{jkl}(\tau - t)E_k(t)E_l(t) + {}^{Q}\chi^{(2)}_{jkl}(\tau - t)E_k(t)E_l(t) + \int_{-\infty}^{\tau} J_j(t')dt'. \qquad \text{Eq. 4.2}$$

where t is the time at which the pump pulse field components E arrive at the sample, and τ is the delay time between the pump and the probe pulses. The parameters in the Eq.4.2 are: the second-order surface dipole nonlinear susceptibility ${}^{S}\chi^{(2)}$, the second-order bulk quadrupole nonlinear susceptibility ${}^{Q}\chi^{(2)}$, and the photo-Dember current $J(t)$ arising from the different mobilities of

electrons and holes [129-131]. $\vec{E}_k$ and $\vec{E}_l$ are any pair of the incident electric field components along the *j*, or surface normal, direction with frequencies ω and ω' that satisfy the requirements for the nonlinear processes generated inside the sample. The bulk dipole contribution does not exist for a centrosymmetric material such as Si [132]. The nonlinear polarization $P_j^2(\tau)$ modulates the sample reflectivity through the electro-optic effect [129, 130, 133], i.e., Pockels effect, which is the change of the refractive index of a medium by application of an electric field [134, 135]. The polarization and the photoexcited carrier density created by the pump pulse change the reflectivity of the sample by changing its dielectric function. The change in reflectivity is related to the change in the electric field generated by the LO vibration through $\Delta n_{EO} = \frac{1}{2} n^3 r_{41} \Delta E$, where *n* is the index of refraction of Si and *r* is the electro-optic coefficient [8]. The probing of the pump induced nonlinear polarization occurs thus by scattering of the probe from the induced polarization, as shown in Fig. 38.

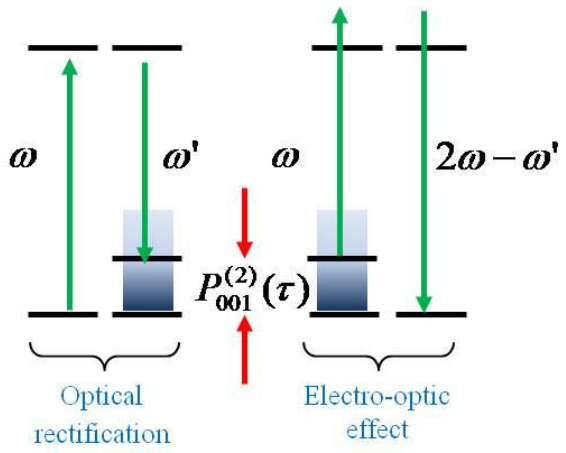

Figure 38: Cascaded excitation and probing Si by coherent anti-Stokes Raman scattering (CARS). The pump pulse generates a second-order polarization (optical rectification) with the frequency of the LO phonon and the probe scatters from it, with its intensity and polarization direction changed.

The excitation and probing of coherent phonons can be thought of as a cascaded sequence of coherent Stokes and anti-Stokes scattering (CSRS, respectively CARS), which are third-order in the electric field for the overall process, and therefore described by a third-order susceptibility given by:

$$\chi^{(3)}(\omega'';\omega',-\omega,\omega') \approx \chi^{(2)}(0;-\omega,\omega')\chi^{(2)}(\omega'';\omega',0), \qquad \text{Eq. 4.4}$$

In Eq. 4.4 the second order susceptibility $\chi^{(2)}(0;-\omega,\omega')$ describes the optical rectification [129, 136] of the pump electric field in the material where two THz frequency fields mix to generate a polarization at their difference, and $\chi^{(2)}(\omega'';\omega',0)$ describes the linear electro-optic effect, where the mixing of the generated polarization and the incoming probe field modulates the reflected field at THz frequencies.

Due to the time dependent change of the dielectric function, $\varepsilon(\tau - t)$, induced by the pump, the electric field of the probe pulse reflected by the sample is changed in a time delay dependent manner:

$$\vec{E} = \frac{\vec{E}_0}{\varepsilon(\tau - t)}, \qquad \text{Eq. 4.5}$$

where *E* is the electric field of the probe pulse, E_0 the magnitude of its electric field before reflection, *t* the arrival time of pump pulse at the sample (Fig. 39), τ the delay, and the time.dependent dielectric function is related to the susceptibilities (Eq. 4.4, Ref. [54], page 53).

As indicated in Fig. 39, the induced longitudinal polarization modulates the perpendicular and parallel components of the reflectivity with respect to the polarization of the pump pulse with the opposite phase (See Fig. 26); therefore, only the surface normal component of polarization, $P^{(2)}_{001}(\tau)$, is recorded. The isotropic contribution of the thermalized carriers to the reflectivity changes the two probe polarization components with equal amplitude and phase.

Therefore, subtraction of the electronic signals of each component eliminates the isotropic contributions.

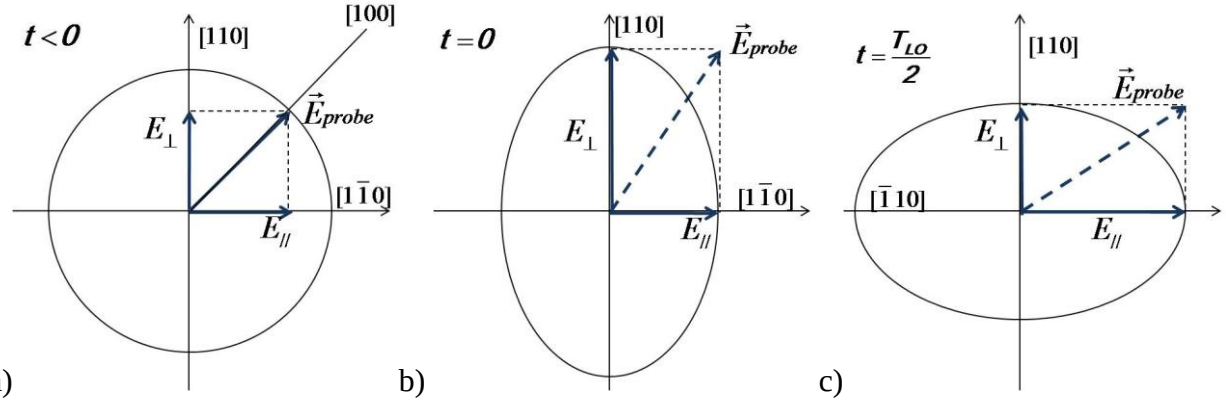

a) b) c)

Figure 39: The reflected part of the probe electric field shows the change of its amplitude and polarization orientation with respect to the crystalline structure a) before pump arrives at the sample, b) when pump arrives at the sample and c) after half period of the LO phonon oscillation.

The choice of orientation of the linear polarization of the pump pulse with respect to the crystalline lattice permits the excitation of the LO phonon both by the sudden increase of the number of carriers in preferential *k*-space directions, which force the ions to move from the equilibrium position to compensate for the new charge distribution (DECP), and by the frequency mixing of two light pairs that match the phonon frequency (ISRS). DECP and ISRS mechanisms are extensively discussed in Sections 2.2.3 and 4.4.1.

In Fig. 40 are presented the transient reflectivity signals recorded in the $\Gamma_{25'}$ symmetry (Fig. 26a) for all the samples measured. The transient signal consists of an aperiodic component created around zero time delay, and on a longer picosecond time scale, of an oscillatory component with a residual slowly varying aperiodic contribution. This residual contribution to the signals is largest for the p-high doped sample. In the transient reflectivity signals measured

for the Γ_{12} symmetry the Raman excitation of LO phonon in Si is not allowed by optical selection rules.

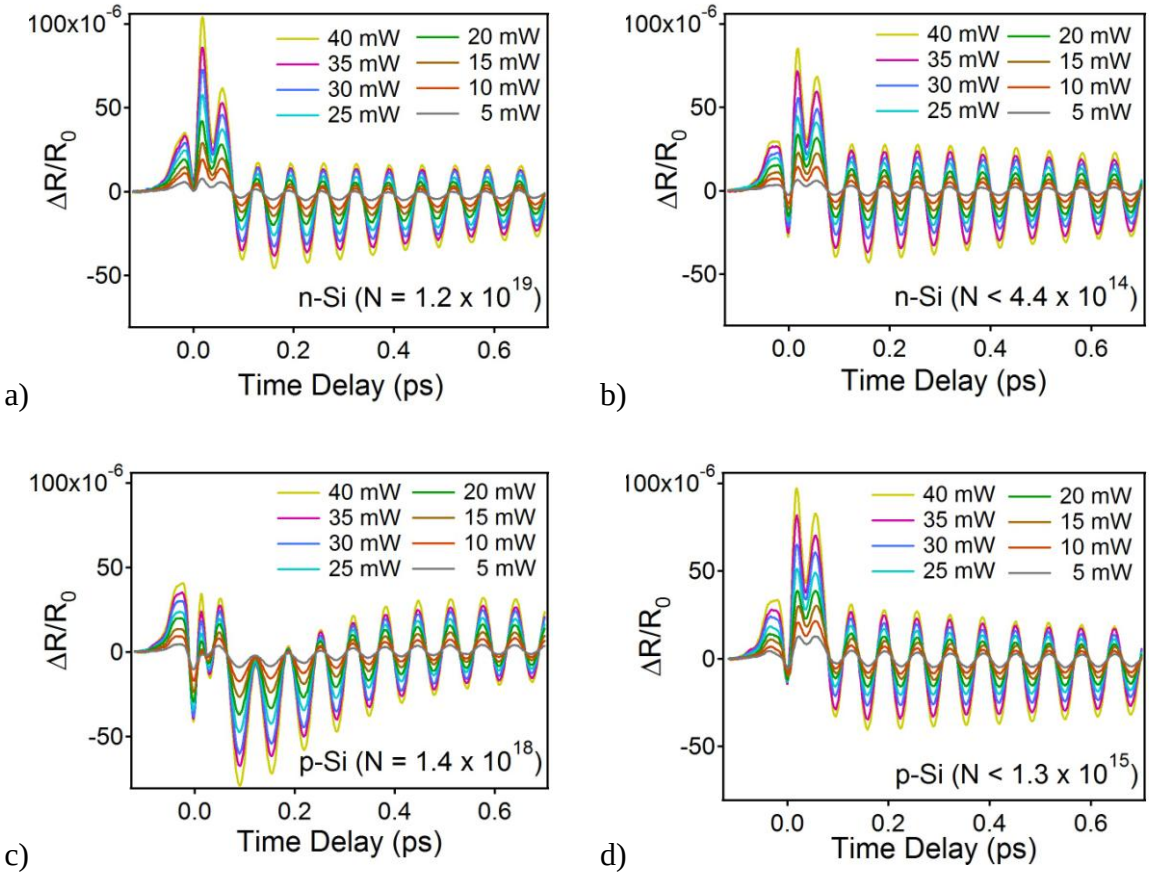

Figure 40: Transient reflectivity of Si for the $\Gamma_{25'}$ symmetry for: a) n-high doping, b) n-low doping, c) p-high doping, and d) p-low doping (see Table 2 for samples description).

A less abstract explanation is that in Γ_{12} symmetry, the pump polarization is oriented (Fig. 26b) such that that the excitation generated in the sample is isotropic in the real and reciprocal space. Therefore, there is no directional force exerted on the lattice that would excite coherent phonons. The faint oscillatory part visible in the Γ_{12} symmetry transient signals is due to slight misalignment of the pump pulse polarization with respect to the lattice. The aperiodic component near zero delay consists of a slight rise in the reflectivity, followed by a sharp drop near time zero, and an overshot back to positive values. Its appearance strongly depends on the

properties (duration and chirp) of the pump pulse. At longer times the reflectivity anisotropy decays to zero in a sample doping dependent manner. The signal near time zero comes from the optically excited currents induced in the sample. The signal has approximately a second derivative shape, because it reflects the acceleration of charges by the electric field of the excitation pulse. The zero crossings should occur at approximately the inflection points of the excitation pulse.

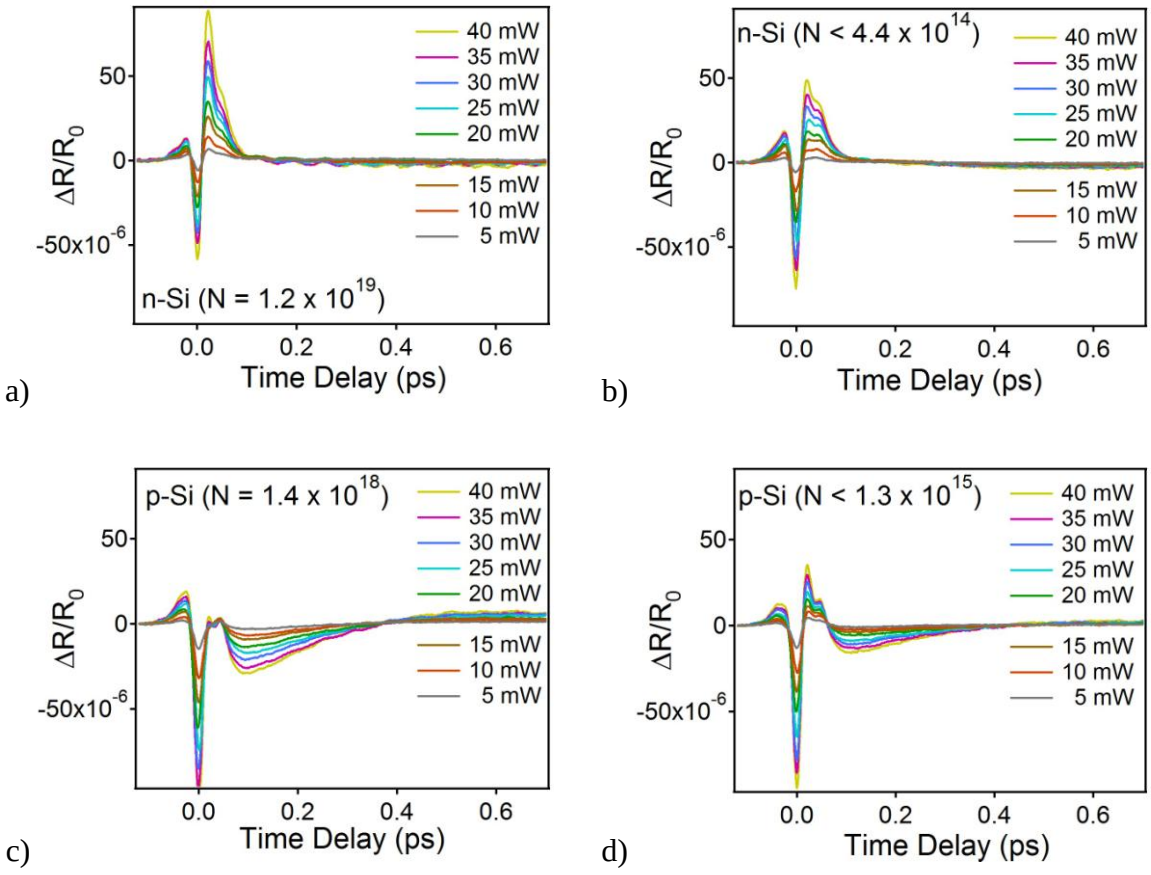

Figure 41: Transient reflectivity of Si for Γ_{12} symmetry for n-type: a) high doping and b) low doping; p-type: c) high doping and d) low doping.

However, because the excitation creates real carriers which can undergo momentum scattering, the material response does not follow the instantaneous electric field of the laser pulse. The detailed interpretation of the signal near time zero, however, is uncertain because it depends on

the laser pulse chirp as well as the scattering processes. The decay of the initial anisotropy on about 50 fs time scale probably corresponds to the momentum randomization by electron-phonon interactions. To analyze the different contributions to the transient reflectivity signal in frequency and time domain we perform a continuous wavelet transform (CWT) analysis (Vallen Wavelet software, [137]). In this way a frequency-time chronogram is created for each signal. As an example, in Fig. 42 are shown the chronograms (CWT) corresponding to n-type high doped Si transient signals at 40 mW pump power for $\Gamma_{25'}$ and Γ_{12} symmetries.

The chronograms show the LO phonon response at ~15.3 THz for $\Gamma_{25'}$ symmetry, and the ultra-broadband electronic signal centered at zero delay for both $\Gamma_{25'}$ and Γ_{12} symmetries. The electronic signal spreads from 0 to >50 THz and its high frequency tail position marks time delay zero. Based on the frequencies involved, it has contributions from inter- and intra-band electronic currents excited by second-order electric field interactions in the sample. These second order interactions include electron-hole pair excitation across the direct band gap of Si and electronic Raman scattering.

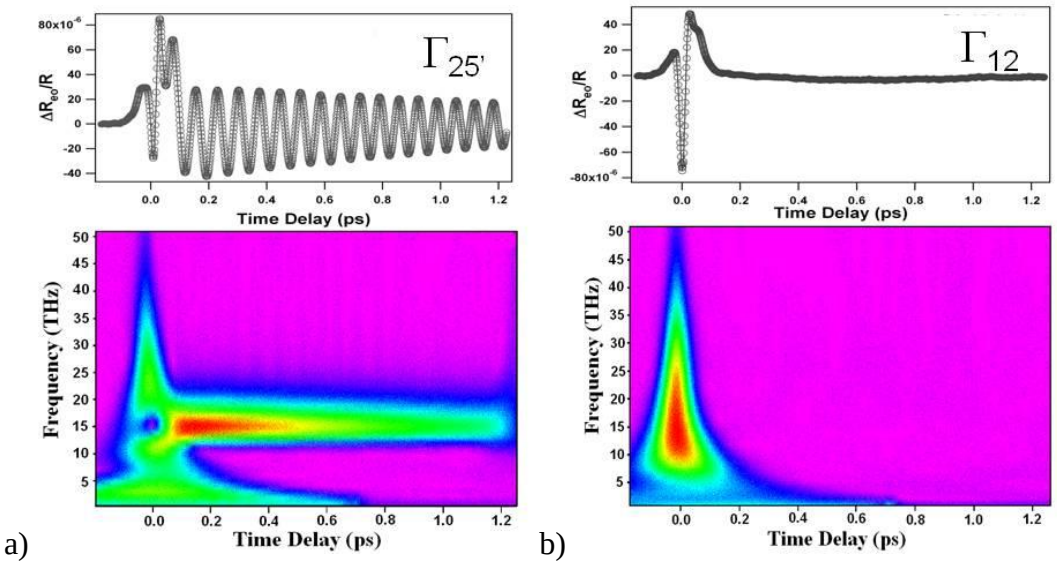

Figure 42: CWTs of n-type Si (40 mW pump power) for a) the $\Gamma_{25'}$ symmetry, and b) the Γ_{12} symmetry.

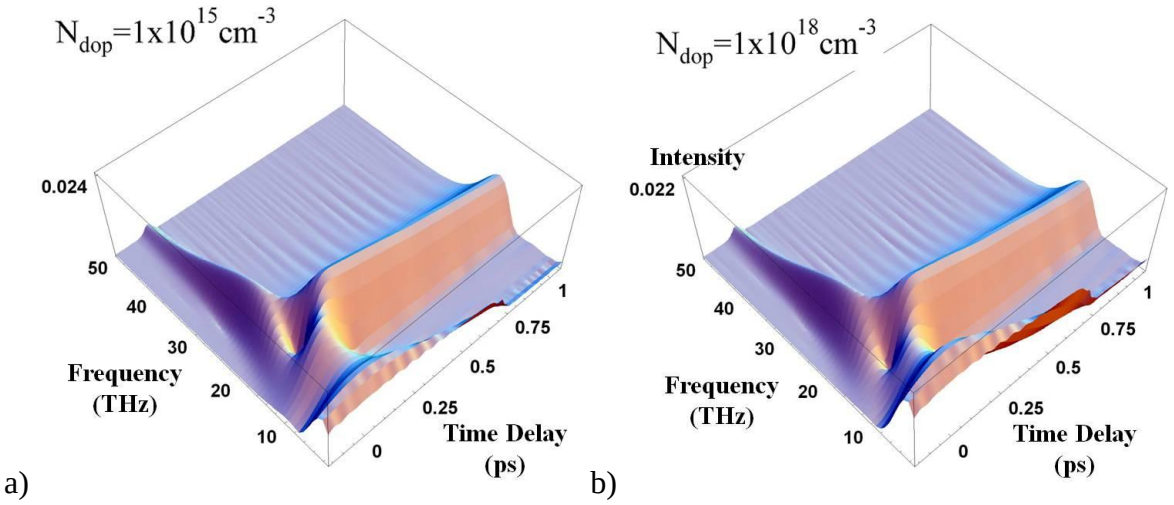

Figure 43: 3D view of the CWT of n-type Si at 40 mW pump power and $\Gamma_{25'}$ symmetry; a) low doping, and b) high doping.

3D views of chronograms for n-Si, low and high doped are shown in Fig. 43. Both the dip at around time zero and the build-up of the phonon line intensity at 15.3 THz are clearly visible. For decreasing excitation frequency the spectral amplitude of the broadband electronic response with respect to the amplitude of the LO phonon increases. Cross-sections of the chronograms at zero time delay display information about different scattering and excitation contributions to the response of the Si lattice to the applied pump field. In Fig. 44 are presented the time-zero CWT cross-sections for the signals measured at pump powers between 5 and 40 mW, for $\Gamma_{25'}$ symmetry. One can distinguish three main features in the time zero slices of the chronograms: a dip at a frequency around the LO phonon mode frequency (labeled B in Fig. 44a and 45a), around which there is a feature at lower frequencies containing two peaks (A), and a decaying tail at higher frequencies (C).

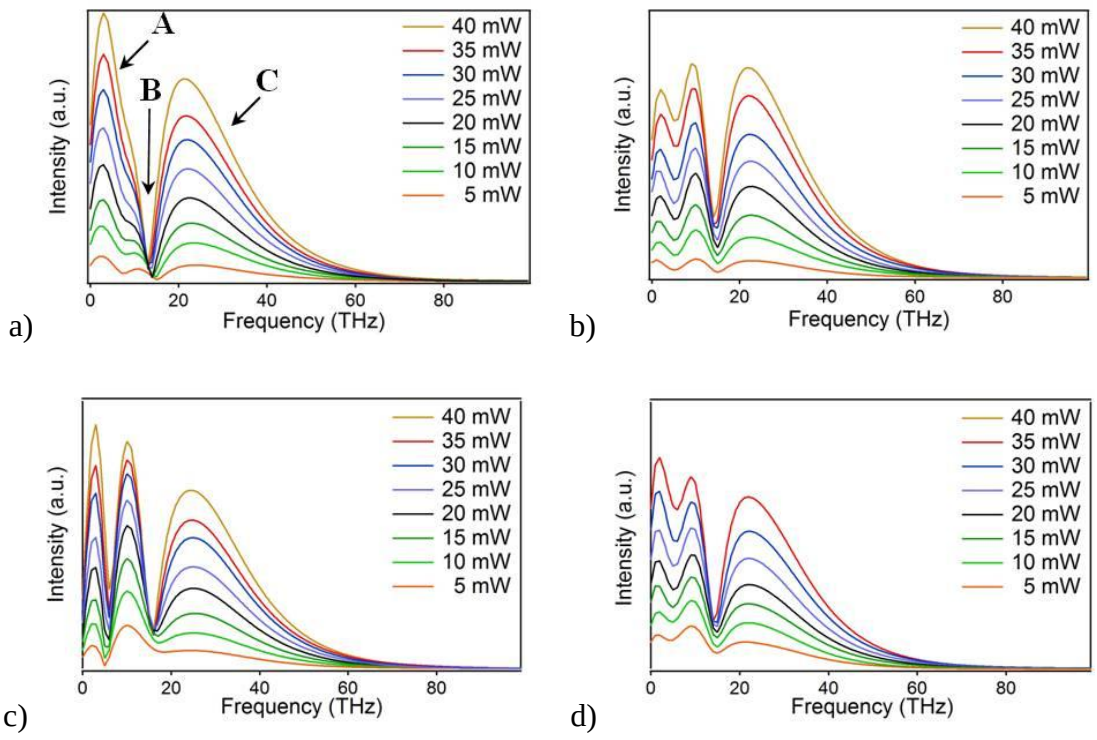

Figure 44: Cross-sections of the chronograms of CWTs at time zero, at $\Gamma_{25'}$ symmetry: a) n-high doped; b) n-low doped; c) p-high doped; d) p-low doped. The distinctive features are labeled A, B, C.

For $\Gamma_{25'}$ symmetry the peaks of the time zero cross-sections labeled A, which occur at 3-4 and 10-11 THz, are attributed to the intra- and inter-band electronic Raman scattering by doped carriers [28]. In Fig. 45 are displayed time-zero CWT slices at 5 and 40 mW pump power, both for $\Gamma_{25'}$ and Γ_{12} symmetries, for all the samples measured. As expected, the dip (feature B) does not appear for Γ_{12} symmetry. The feature C is similar to both geometries measured, which suggest the same type of contributions in both cases. This ultra-broadband electronic response extends to beyond 50 THz, as shown in Figs. 44 and 45, and is therefore associated in part with the electron-hole pair excitation across the direct band gap of Si. Absorption is the same order in the electric field as Raman scattering, and therefore, it is expected to contribute to the signal. These real processes, together with virtual processes at near-resonance with the direct band-gap of Si, contribute to the $\chi^{(2)}$ modulating the lattice response and generating the LO phonon, i.e.

the LO phonons can be excited via the Raman tensor or through the excitation of an anisotropic electron hole pair distribution.

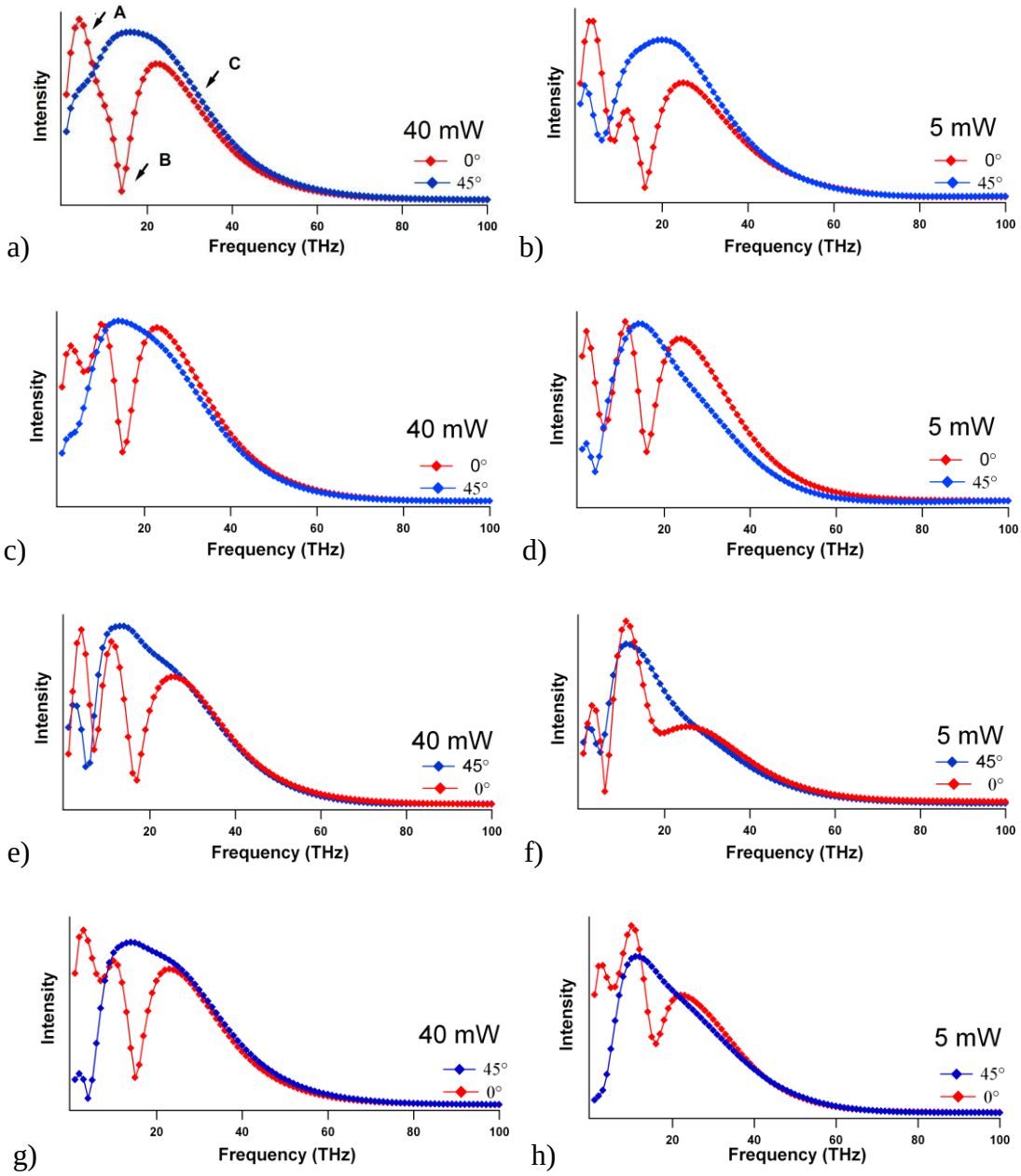

Figure 45: Cross-sections of the chronograms at 5 and 40 mW pump power, for both Γ_{25}' (red) and Γ_{12} (blue) symmetries, at time delay zero; a) and b) n-high doped Si; c) and d) n-low doped Si; e) and f) p-high doped; g) and h) p-low doped. The distinctive features are labeled A, B, C.

The large dip (feature B) occurring around the LO phonon frequency of 15.3 THz arises from the coupling of the LO phonon mode with the photoexcited electron-hole pair continuum. The LO phonon couples to the electron-hole pair continuum through the deformation potential interaction, and its amplitude is suppressed by destructive interference (a window resonance) with the electronic continuum. The decrease in the frequency position of the dip as the excitation intensity increases is more noticeable for high doping density for both n-and p-type samples. In time domain, the dip minimum occurs at slightly different delay times (2-5 fs) for various measurements. The less intense the excitation, the later the dip occurs. In other words, the time-frequency location of the anti-resonant interaction between LO phonons and carriers vary with the doping amount and with the pump power, suggesting concomitant excitation mechanisms the coherent LO phonon, finite phase relaxation time of the induced polarization and time-frequency uncertainty, as detailed in Subchapter 4.4.

In Fig. 46 are shown intra- and inter-band transitions responsible for creating the continuum overlapping with the energy of the discrete phonon state [124] for both n- and p-type doped Si. The transitions involved in intraband scattering in p-type doped Si occur mainly within the heavy-hole (*hh*) valence band while excited holes relax toward the band top, and the ones involved in interband scattering occur in between the *hh*, *lh* (light-hole) and *so* (split-orbit) bands (Fig. 46b), in a frequency range that overlaps with the LO phonon frequency, and can contribute to the Fano interference [40, 124, 138]. The case of p-doping is quite similar to p-Si, with the continuum provided in this case by interband transitions $\Delta_1 \rightarrow \Delta_{2'}$ with a minimum energy of ω_{min} and a maximum energy of ω_{max}, as shown schematically in Fig. 46a. The energy spreading of the continuum in the case of doped Si depends on the impurity doping. For both p- and n-

doped Si the interaction between the continua and the LO phonon renormalize the self-energy of the phonon and affect the shape, peak frequency and broadening of the Raman spectra.

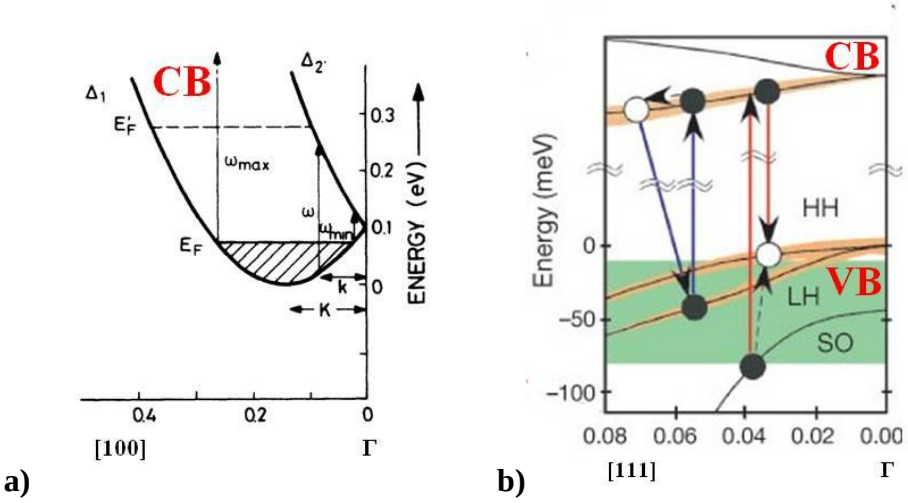

Figure 46: a) Transitions involved in Raman and electron-LO phonon scattering in n-type doped Si; from [139]; b) transitions responsible for both electronic Raman scattering and electron-phonon interaction in heavily impurity doped p-type Si; adapted from [127].

4.1.2 Summary

The self-energy of the coherent zone-center LO phonon measured in these experiments is evident through the departure from the values of the LO phonon frequency (15.3 THz) from the value of 15.6 THz for intrinsic Si [40]. We will show later that the LO phonon damping time also is reduced from the 3.5 ps value for intrinsic Si. The shift of frequency is related to the real part of the complex self-energy, and the dephasing rate with its imaginary part. The chronograms show evidence of the many-body processes that participate at the generation of LO phonon and electron-hole pair continuum, their time-scales and their subsequent interaction via Raman or carrier-phonon interactions, which contribute to the $\chi^{(2)}$ and $\chi^{(3)}$ responses.

4.2 COHERENT LO PHONON SELF-ENERGY UNDER HIGH CARRIER DENSITY EXCITATIONS IN SI

Free carriers and carrier-phonon interactions influence both the optical and electrical properties of semiconductors. An indicator of the state of the matter is its phonon spectrum, which can change drastically when the material is subjected to high intensity laser pulses with less than 100 fs duration [140]. In this Subchapter we report the time dependence of the zone-center LO phonon frequency shift and dephasing rate (i.e., complex self-energy of LO phonon $\Sigma = \Sigma_r + i\Sigma_i$) after the excitation of Si(001) with 10 fs pulses of various intensities. Recall that the self-energy results from the interaction of free carriers with LO phonons through the deformation potential mechanism. The real part of the self-energy is proportional to the frequency shift, $\Delta\nu_{LO}$, and the imaginary part contributes to the dephasing rate, Γ_{LO}.

4.2.1 Introduction

As introduced in Chapter 2, the LO phonon in Si can decay into or be excited by single-particle electron-hole pair excitations through the deformation potential interaction. This interaction is associated with the dynamical changes in the electronic band structure due to the LO phonon acting as a strain on the lattice. The anisotropic and periodically varying strain induces redistribution of the carriers within and among bands. These interactions induce a red-shift in LO phonon frequency and contribute to its broadening. The LO phonon frequency can also be influenced by the lattice temperature as the photoexcited carriers lose their energy to the lattice. Moreover, the gradient of optically injected carriers creates a strain perpendicular to the sample surface, which excites acoustic phonons that propagate into the bulk [28] (Section 2.6). Also, the

transient positive strain produced by the lattice temperature increase (Subsection 2.5.1), combined with the transient negative strain produced by the excitation of carriers, lowers the crystalline symmetry and produce opposite shifts of the LO phonon frequency as well as changes in its spectral broadening. We measure in a time-resolved (TR) manner the combined effect of these factors on the coherent LO phonon shift and broadening with respect to the Si zone-center optical phonons in the absence of any perturbation.

The effect of free carrier density N introduced by doping on the first-order Raman spectrum of Si was extensively studied by Cerdeira and Cardona [28]. The zone-center LO phonon acts on the lattice in a manner similar to a shear strain applied in the [111], which causes splitting and shifting of the electronic bands according to their symmetry. For instance, the [111] strain in Si lifts the eight-fold degeneracy of the L-valleys, splits the conduction bands at the X-point, and lifts the degeneracy of the *hh* and *lh* bands at the Γ-point. The effect on the L-valleys and valence bands is first-order in the lattice displacement, whereas for the X-valleys, which remain equivalent under [111] strain, the effect is second-order in the lattice displacement. In the case of the LO phonon oscillation, the time-dependent strain causes the carriers to dynamically redistribute among the different valleys in accordance to the changes induced in the energy bands, if the scattering processes are sufficiently faster than the 64 fs LO phonon oscillation period. Therefore, the effect of free carriers on the LO phonon is expected to be observed when $\omega_0 \tau \leq 1$, where ω_0 is the intrinsic LO phonon frequency and τ is the electron scattering time associated with minimizing the free energy of the system. The redistribution causes a reduction in the shear elastic constants, as well as a red shift of the LO phonon frequency and spectral broadenings of the Raman lines, which Cerdeira and Cardona [28] measured for increasing doping concentration of charge donors and acceptors in Si. In the case of free electrons in the L-

valleys and free holes at Γ point, the frequency shift $\delta\omega$ was predicted to be proportional to the cubic root of the carrier density; in the case of X-valleys electrons, the shift was found to be directly proportional to the electron density [28, 141]:

$$\left.\frac{\delta\omega}{\omega}\right|_{holes} \approx -\left(\Xi_{u'}\right)^2 N^{\frac{1}{3}}, \quad \left.\frac{\delta\omega}{\omega}\right|_{electrons} \approx -\left(\Xi_d^{\Delta} + \frac{1}{3}\Xi_u^{\Delta}\right)^2 N, \qquad \text{Eq. 4.6}$$

where $\Xi_{u'}$ and $\Xi_d^{\Delta} + \frac{1}{3}\Xi_u^{\Delta}$ are the deformation potentials for LO phonon-hole, respectively the LO phonon-electron coupling (App.C). The change in the decay time of LO phonon, τ_{LO}, was found, based on Raman line shape analysis, to be negligible for n-type doping and inversely proportional to the carrier density for p-type doping [28]:

$$\tau_{LO} \approx \frac{1}{N}. \qquad \text{Eq. 4.7}$$

The effect of L-valley electrons in Si can only be observed under nonequilibrium conditions, such as in our experiments. Recently Tanimura et al. reported the L- to X-valley scattering in Si to be on ~300 fs time scale [39]. This suggests that in our experiments the electron-phonon interaction will be governed by different deformation potentials for the first few hundred femtoseconds before the L- to X-valley transfer is complete.

Lattice temperature has a smaller contribution than the carrier density to both frequency shift and dephasing rate of the LO phonons [99, 142, 143]. Hart et al. [99] measured the LO phonon frequency decrease with lattice temperature increase; for n-Si with doping density of 7.8×10^{19} cm^{-3}, for example, they found a variation of the LO frequency with the lattice temperature T_L given by

$$\nu_{LO}(T_L) = 15.8 - 6.45\times10^{-4}\times T_L. \qquad \text{Eq. 4.8}$$

The dependence of LO phonon dephasing rate on the lattice temperature T_L was found to be [98]:

$$\Gamma(T) = \Gamma_0\left[1 + \frac{2}{\left(e^{\hbar\omega_0/2k_BT} - 1\right)}\right]. \qquad \text{Eq. 4.9}$$

where Γ_0 is an effective anharmonic dephasing rate, $\hbar$ is the reduced Plank's constant, and k_B is Boltzmann's constant.

Unlike the static cases of doped Si studied in literature, in this work the doped carrier density is smaller than the photoexcited carrier density, and holes and electrons are photoexcited in equal amount and contribute simultaneously to the lattice softening. The photoexcited carrier distribution and density change in time by a variety of scattering processes, diffusion, and recombination (see Chapter 2); therefore, the LO phonon self-energy is a function of time through its dependence on the dynamically varying lattice and electronic subsystems. The measurement of the LO phonon frequency as a function of delay from the excitation pulse provides information on the time evolution of the electronic system.

4.2.2 Experimental results

We measured the transient reflectivity change of Si for n- and two p-doped (Table 2) Si samples. All measurements were done at room temperature for pump powers varying between 10 and ~63 mW. In Fig. 47 are presented transient reflectivity signals for the high-doped p-type Si sample. Their normalized frequency spectra, in the region of the LO phonon peak, are shown in the inset. A shift of the peak frequency towards lower values, an increase of the peak broadening, and a more pronounced asymmetry of the phonon line shape can be clearly seen as the initial photoexcited carrier concentration is increased (i.e. pump power increases). All of these features, including the peak asymmetry which arises from the Fano interference between LO phonon and the electronic continuum, are manifestations of electron-phonon coupling.

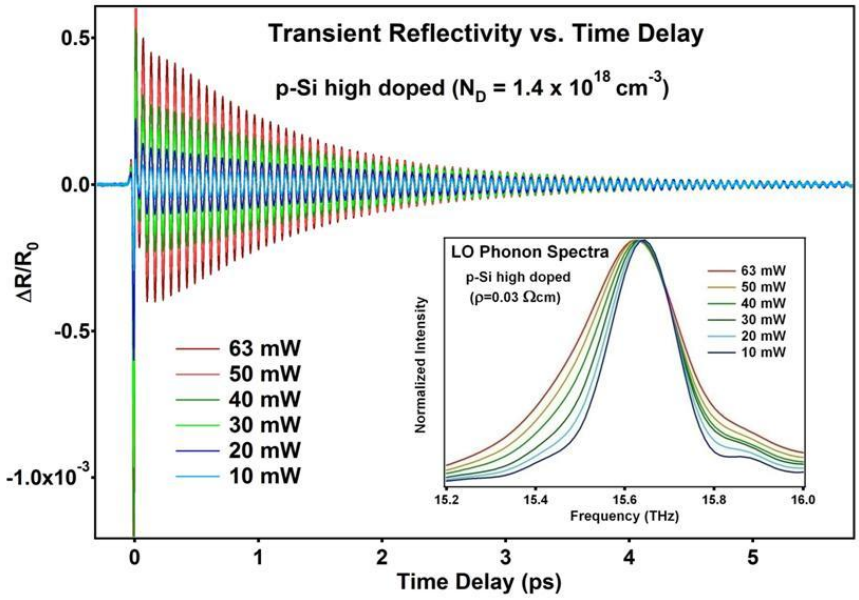

Figure 47: Transient reflectivity of p-doped Si. The inset shows FT spectra of the LO phonon peak.

As described previously, the transient reflectivity signals show an initial aperiodic component followed by an oscillatory contribution slightly offset by a slowly varying signal. The slowly varying signal is removed from the oscillation by fitting the signals to a combination of exponentials and subtracting the resultant curve, as shown in Fig. 48. The oscillatory component of the transient reflectivity is approximately a damped cosine function of time delay *t*, with the frequency and decay time expected to vary with the carrier concentration, and therefore, the time delay. The signal can be modeled with a functional dependence described by

$$F(t) = A\exp\left(-\frac{t}{\tau+\delta t}\right)\cos\left[(2\pi\nu+\eta(t))t+\varphi\right], \qquad \text{Eq. 4.10}$$

where A is the amplitude of oscillation, τ the LO phonon dephasing time, ν the LO phonon frequency, and φ the initial phase of the oscillation. To account for the variation of the dephasing time and frequency on the delay time, i.e., the carrier density, Eq. 4.10 describes the dephasing time and frequency time dependence, respectively, by δt and a frequency chirp $\eta(t)$.

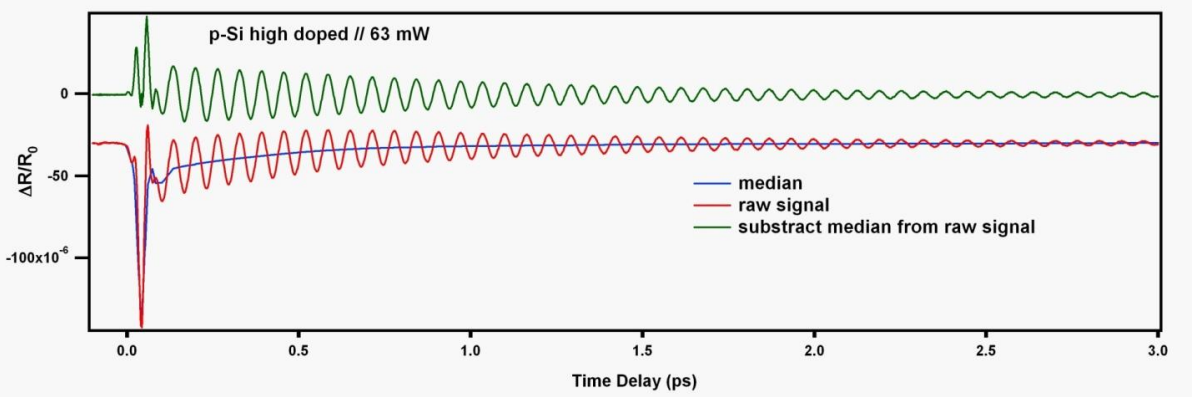

Figure 48: Transient reflectivity of p-Si high doped (63 mW pump power excitation): measured signal (red), slowly varying component (blue); pure oscillatory component (green).

We are interested to retrieve the LO phonon frequency at time zero, and the average value of the phonon dephasing rate over the scanned time delay interval. We fit the oscillatory part of transient reflectivity signals to Eq. 4.10, assuming a frequency shift $\eta(t)$ has a 3rd degree polynomial dependence on the time delay, and, for now, a time independent dephasing rate.. We let the frequency shift, the time zero frequency, phase and amplitude, and the dephasing rate be variable parameters. The time zero LO phonon frequency and its dephasing rate (inverse of dephasing time) obtained are shown in Fig. 49. They are found both to vary linearly with the photoexcited carrier density, i.e., the pump power, which was estimated (App. A) with absorption coefficients from Jellison [85] (Fig. 66); these trends are in agreement with the frequencies and dephasing rates of the zone-center LO phonon measured by Raman scattering in doped Si [28, 41]. In our case the p-Si doped samples display slightly higher LO phonon frequencies than the n-type samples, fact which departs from the reported literature findings.

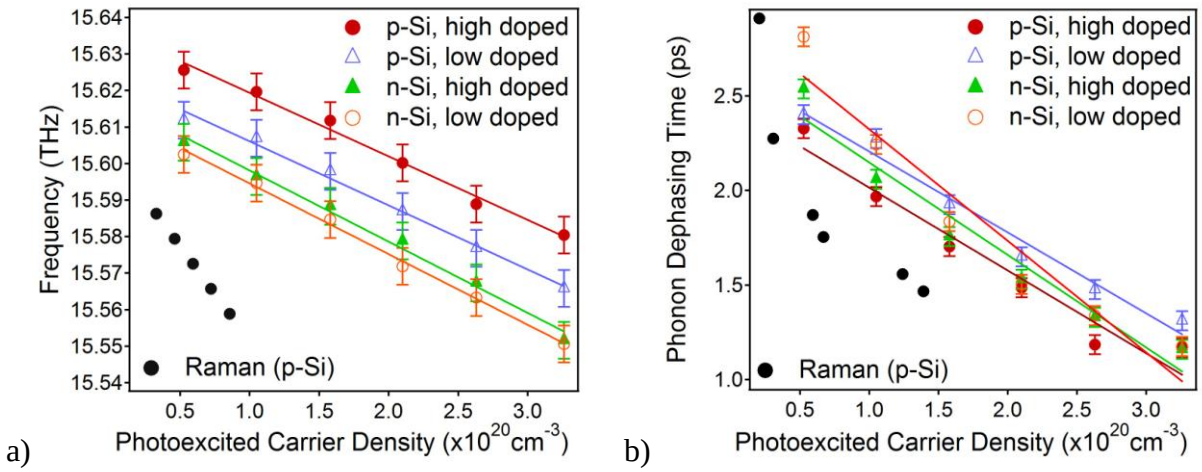

Figure 49: LO phonon frequency (a) and dephasing rate (b) (from transient oscillatory data fit with Eq. 4.10) vs. carrier density. The black dots represent the frequency and dephasing time reported in [28].

To get a clearer picture of LO phonon frequency and decay time dependence on the time delay, we present in Fig. 50 a typical transient reflectivity signal measured for p-Si low doped at 62 mW pump power, fitted to Eq. 4.10. The fit returned a time zero frequency of $\upsilon = 15.58 THz$ and a decay time constant of $\tau = 1.18 ps$. The inserts of Fig. 50 show enlarged portions of the transient reflectivity oscillations at different time delays. The mismatch between the fit and the data becomes more pronounced as the time delay increases, and is explained by the LO phonon frequency not having the time dependent form consistent with a fitting function of the form of Eq. 4.10, and LO phonon decay time being dependent on the time delay, rather than constant, as we considered it for fitting. The conclusion is that both LO phonon frequency and decay time vary with time delay through their dependence on carrier density and lattice temperature, and, as shown by the numerical calculations presented in Chapter 5, their variation is nonlinear with respect to time delay because of the carrier density and lattice temperature do not vary linearly with the time delay. In fact, a simple linear approximation would not capture the actual time evolution of the LO phonon frequency and dephasing rate.

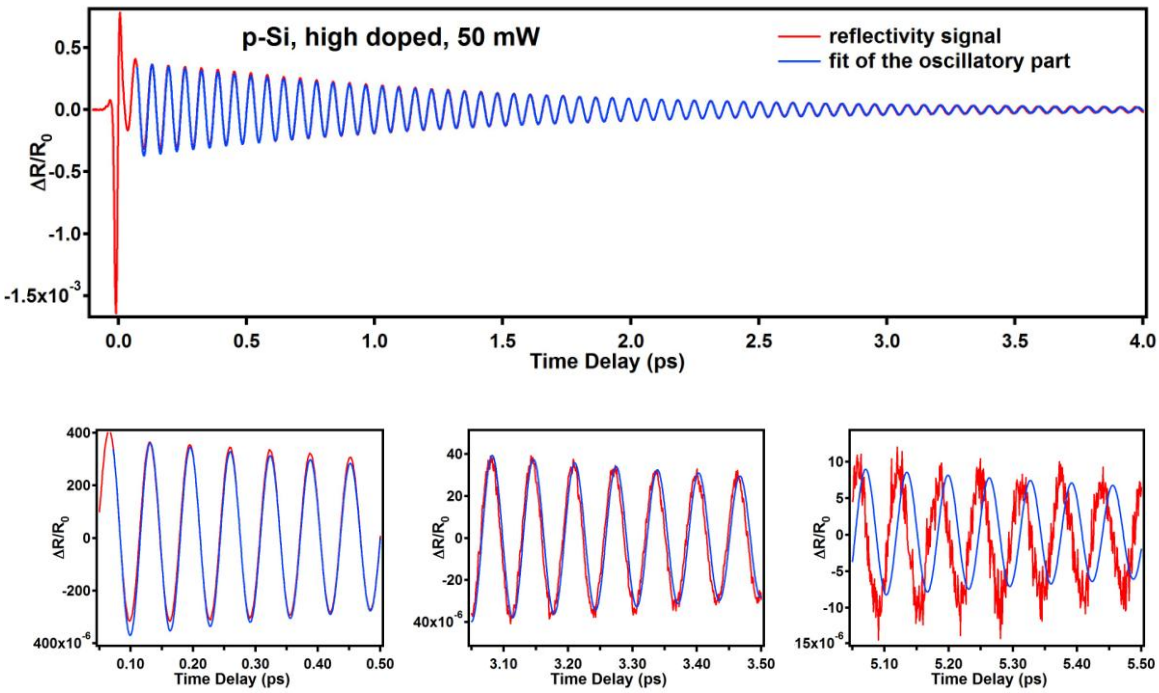

Figure 50: Transient reflectivity signal fitted to Eq. 4.10; p-Si high doped, 62 mW pump power. The expanded oscillations show a mismatch between the fit and the data which increases as the time delay increases, and arises from the delay, i.e. carrier density, dependent decay rate and frequency chirp.

In order to get the true variation in the LO-phonon frequency and decay rate, their time dependences for p- and n-type Si samples are retrieved from data following the procedure explained in Section 3.6, and are presented in Fig. 51. The loss of LO phonon phase correlation is directly observed from the decay of the probing reflected signal, while the frequency shift is retrieved by a "window-Fourier" transform of the transient signal. Comparing the results obtained for samples with different type and doping density, it is clear that the initial doping contributes to the lattice softening. With respect to the n-type samples, the p-type Si samples display at early times less softening, i.e. smaller initial LO frequency red-shift, and at later times higher LO phonon frequencies with respect to the LO phonon frequency value of ~15.6 THz reported in literature for intrinsic Si samples. Also there is a clear difference between the LO phonon frequencies of high and low doped p-Si, while the frequencies corresponding to high and

low doped n-Si are almost the same. All samples display a kink in the frequency at a delay of ~500 fs.

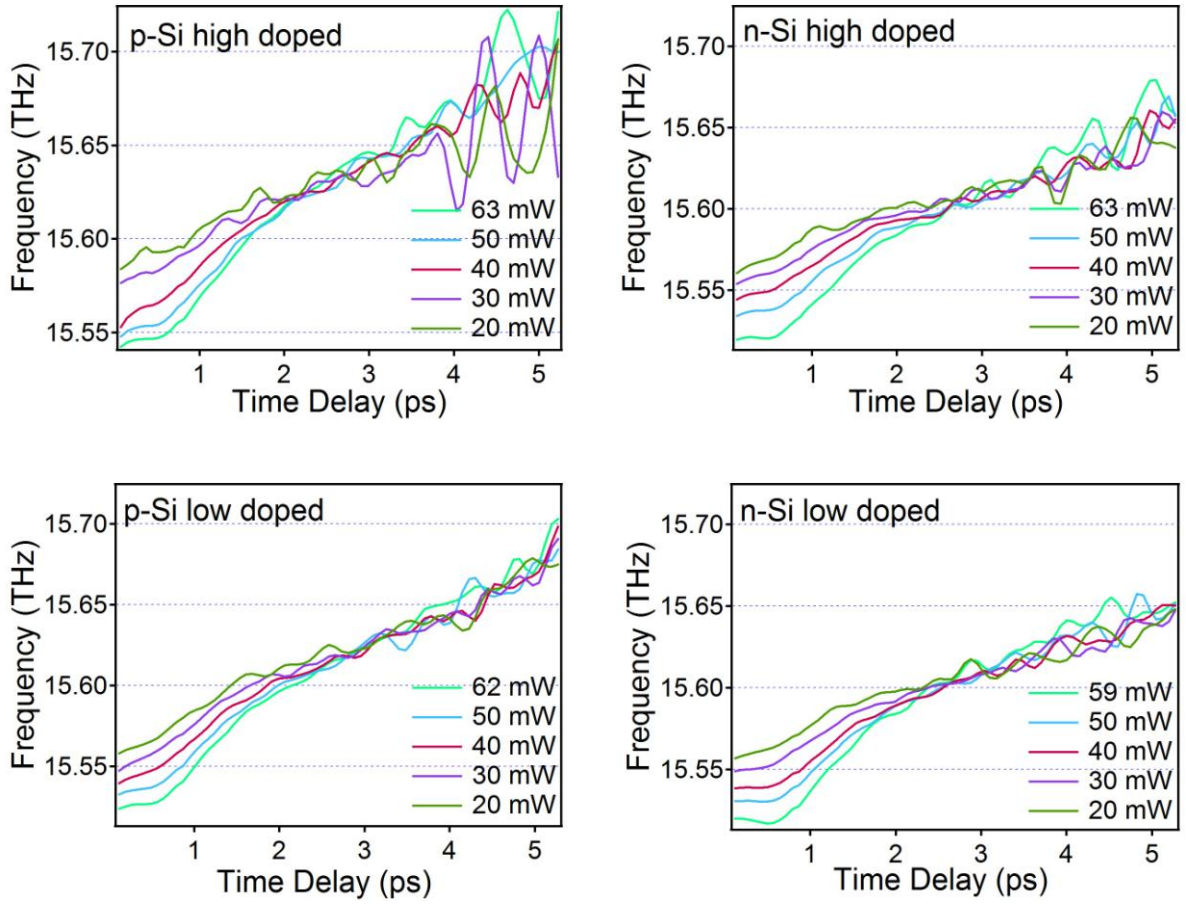

Figure 51: LO phonon frequency vs. time delay for various pump powers, and for different type and density of doping.

The time delay dependent LO phonon decay time is shown in Fig. 52 for all the samples measured. The procedure of extracting the decay time from the envelopes of oscillatory component of the reflectivity is highly sensitive to the noise of the signal. As the pump power decreases, the transient reflectivity data are noisier. Although we smooth the reflectivity curves for 10 and 20 mW pump power, the noise is still sufficiently large to induce high uncertainty in the LO phonon decay time vs. time delay curves extracted for the low doped n- and p-type samples at these pump powers. The decay time displays quasi-linear time delay dependence for

all the samples. The deviation from nonlinearity is most pronounced for the p-type high doped Si sample for all pump powers. The degree of the nonlinearity increases for increasing intensity of the initial excitation.

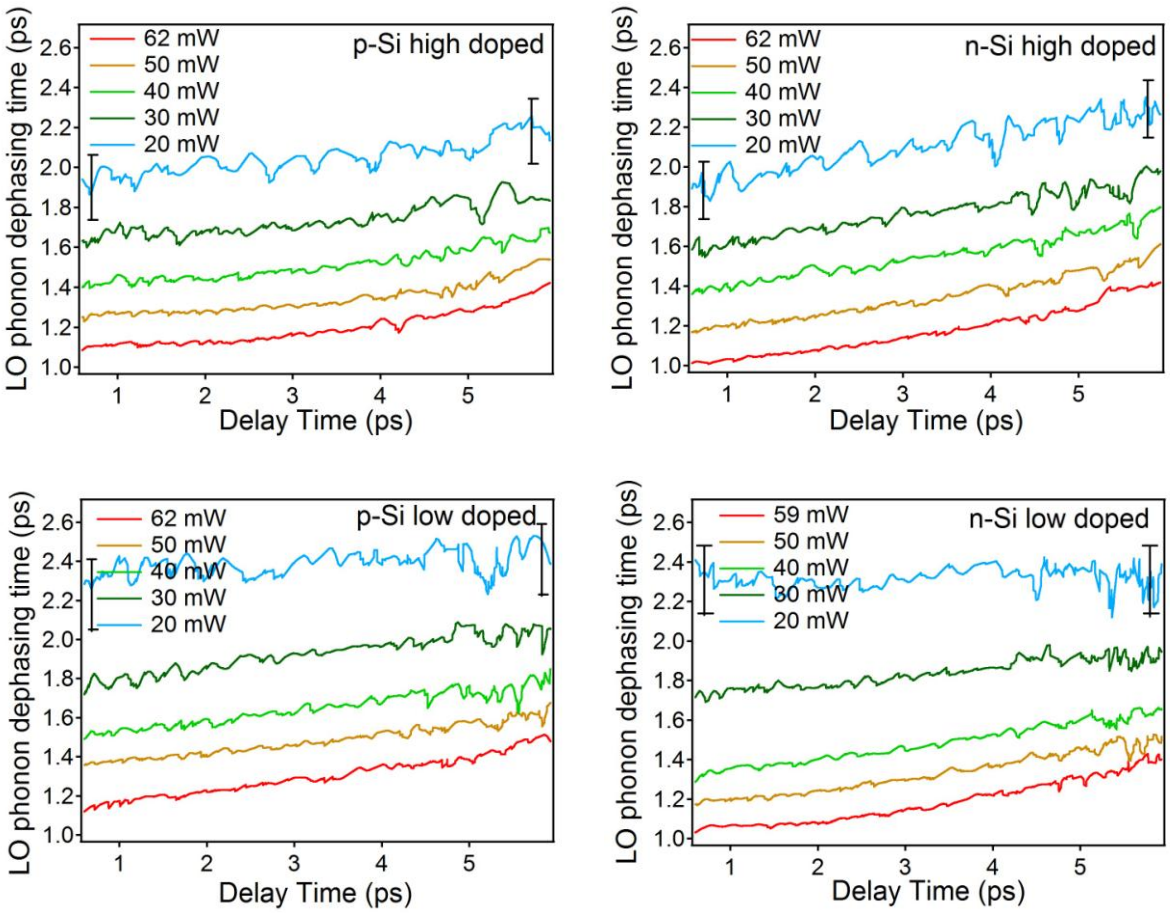

Figure 52: LO phonon decay time vs. time delay for p- and n-type Si measured for various pump powers.

The LO phonon frequency vs. time delay curves show three distinct dependencies on time during the scanned time delay. Right after the excitation the LO phonon frequency vs. time delay profiles clearly show the LO-phonon frequency shifted to values below the 15.6 THz frequency from Raman studies. We attribute this shift to the sudden excitation of carriers in the L-valleys, which interact with the lattice through the deformation potential. The increase in the valence and conduction band carrier densities lowers the conduction band and raises the valence

band in the *k*-space region the carriers were excited, hence softening the lattice and thus producing the initial red shift of the LO phonon frequency. In the first 0.5 ps after excitation the LO phonon frequency is flat, or it may even further decrease. During this period the free carriers thermalize within the L-valleys and also scatter to the X-valleys, while the holes scatter toward the top of the valence band. During this time interval the LO phonon amplitude decay shows a characteristic nonexponential behavior ("saturation effect", Figure 35). There is evidence that following 3.1 eV excitation, the free carrier density in the X-valleys builds up with a time constant of ~300 fs through L- to X-valley scattering [39]. According to the theory of Cerdeira and Cardona [28], the L- and X-valley carriers interact with LO phonons through different deformation potentials and with different carrier density dependences, therefore, in our case it is expected that the transient LO phonon frequency will respond to the carrier redistribution between the two types of valleys on sub-picosecond time scale. After the first 500 fs, the LO phonon frequency continuously increases. Because the carrier thermalization occurs on a sub-picosecond time scale, the frequency change after the initial 500 fs has contributions from the carrier diffusion from the probed volume. During the next 2-2.5 ps the increase occurs at different rates for different initial photoexcited carrier densities, reflecting a density dependent carrier depopulation from the measured volume. Note that the carrier depopulation rate increases as the excitation power increases. The lattice continues to harden and the LO phonon frequency is expected to reach its specific value in the absence of the excited carriers. The numerical calculations we perform (Chapter 5) show that by the end of the 6 ps time delay, the carrier population is reduced in the probing region by only one-half with respect to the initially excited population. According to the dependence of phonon frequency on the carrier density in Eq. 4.6, the LO phonon frequency should still be softer, after a delay of 6 ps, than the 15.6 THz Raman

frequency in the absence of photoexcited carriers. The transient frequency, however, becomes larger than 15.6 THz after a delay of 2-3 ps. In the 6 ps interval for which we can follow the LO phonon frequency in the time domain, the LO phonon frequency for each sample seems to have converged to a pump power independent value that depends weakly on the sample. The LO phonon frequency seems to converge to a steady-state value [41] for later times than the 6 ps we measure. During the later half of the time delay scanned, the measurements reveal that the LO phonon frequency is actually blue shifting with respect to its value in the absence of excitation. The same behavior is observed for all samples measured. The saturation value of the frequency depends on the initial type and density of doping. The observed frequency after 6 ps delay is about 15.65 THz for n-Si and 15.67 THz for p-Si. Similar coherent phonon measurements on other samples, like graphite and diamond, confirm that these changes are due to physical processes occurring in the Si samples rather than an artifact of, for example, the time axis calibration [144-147]. In fact, the interferometric time axis calibration is essential to remove artifacts from the accurate frequency measurement.

In order to further relate the frequency and dephasing rate changes to the physical processes occurring in the samples, in Fig. 53 we plot both the LO phonon frequency shift and dephasing rate vs. the calculated carrier density for n-high doped Si. Other samples show similar behavior. The procedure for calculating the carrier density will be described in Chapter 5. The LO phonon dephasing rate increases as the carrier density increases. In the first-order approximation, this relationship should be linear, which is the case for up to 30 mW pump power. For pump powers above 30 mW, the dephasing rate seems to have a sublinear dependence on the carrier density.

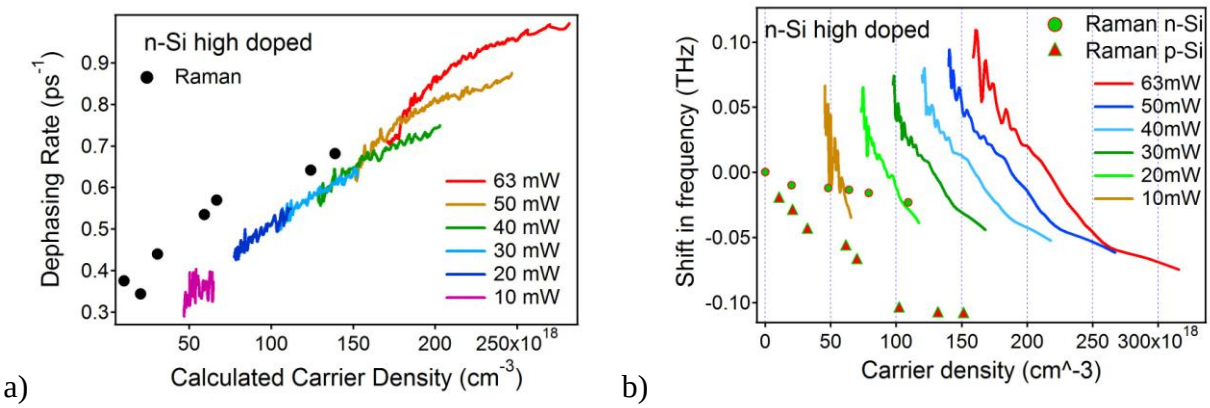

Figure 53: a) The LO phonon dephasing time, and b) its frequency shift as retrieved from the transient reflectivity signals plotted vs. calculated photoexcited carrier density (n-Si, high doping); the lattice temperature contribution was subtracted from the shift. The dots and triangles are Raman values reported in Ref. [28] for n-type Si.

The interpretation of the LO phonon frequency shift is more complicated. In order to estimate other contributions to the frequency shift, we first correct the frequency for the effect of the substrate temperature (see Fig. 54). We can calculate the transient heating of the lattice by considering the energy deposited into the conduction and valence bands of Si, the heat capacity of Si, and a carrier dependent energy relaxation time, as described in Chapter 5. The LO phonon frequency change through sample heating was estimated from the temperature dependence of the LO phonon frequency described by Eq. 4.8, with the equilibrium value of LO phonon frequency taken from Ref. [99] for 300 K (see Fig. 54b). The frequency shift due to lattice temperature increase is subtracted from the measured LO phonon frequency (Fig. 54a); the resultant curves are plotted in Fig. 54c. The heating of the lattice leads to the softening of the LO phonon frequency, so when the lattice contribution is subtracted from the experimental curve, one can clearly see that the stiffening of the LO phonon frequency on picosecond time scale is even more pronounced. Therefore, the self-energy associated with the carrier-phonon interaction as expressed by Eqs. 4.6 and 4.7 cannot fully explain the experimental results, and specifically the

blue shift. Other factors must influence the LO phonon frequency on the picosecond time scale. Because carriers cool and diffuse on picosecond time scale, these factors could be of the electronic in nature, and reflect the effect of photexcited carriers on the lattice.

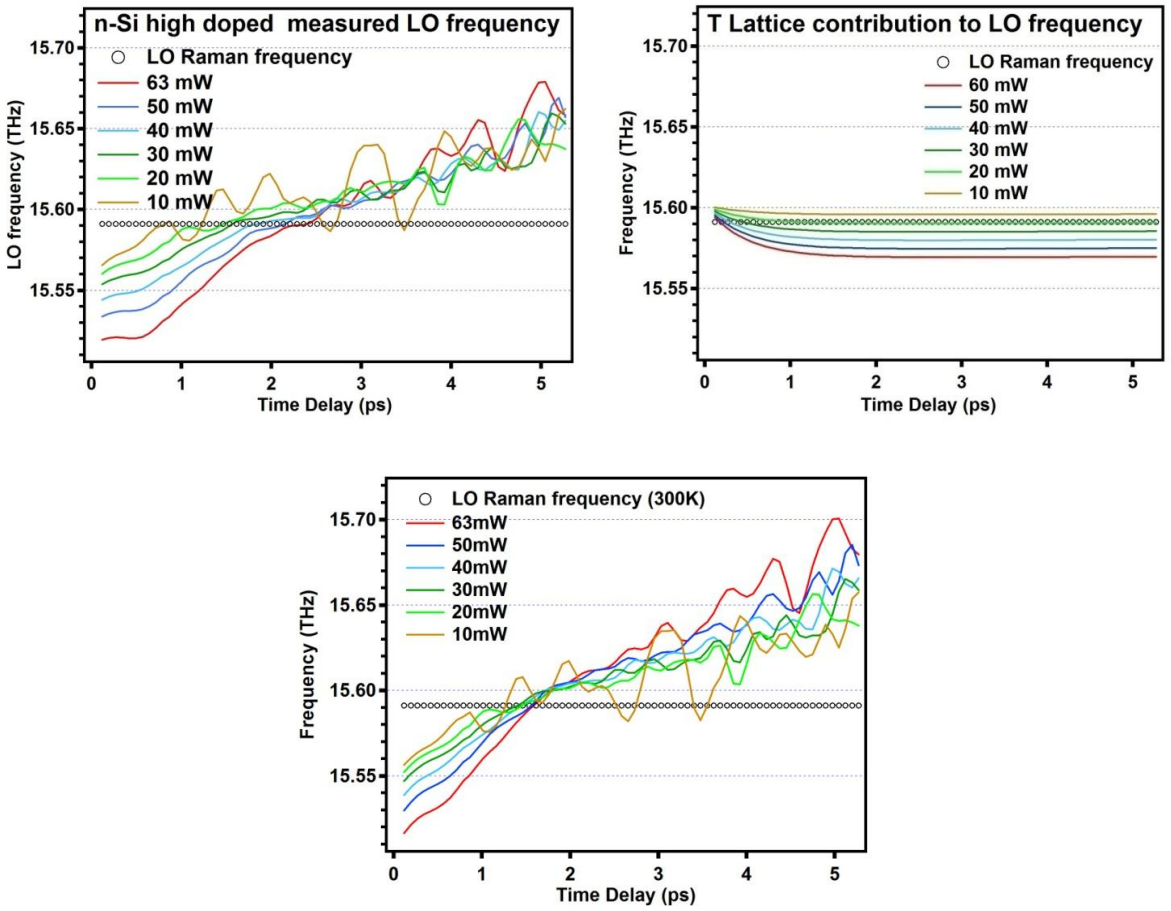

Figure 54: Contributions to the LO phonon frequency (n-Si high doped): a) measured frequency; b) calculated frequency change due to the lattice heating; c) LO phonon frequency corrected for the lattice heating contribution.

4.2.3 Discussion

The departure of LO phonon dephasing time and frequency respectively from the established values for intrinsic Si of 3.5 ps and 15.6 THz reflects the coherent phonon self-energy change,

which depends on the excitation density, and to a smaller extent, the concomitant lattice temperature rise [28, 99, 142]. As for the LO self-energy doping dependence, Sabbah [41] also measured transient reflectivity signals for variously doped Si, and found a clear dependence of the LO phonon dephasing rate on the type and density of doping. He found that the time-domain measurements yield faster dephasing rates than the frequency-domain measurements (Raman), and attributed this effect to the presence of photoexcited carriers. We measure both power and delay dependent dephasing rates which converge at later delay times to the values reported by Sabbah. With 800 nm excitation, however, the penetration of the excitation light into the sample is on the micro scale, and therefore transport out of the volume of excitation should not result in transient changes in the self-energy.

Here we will discuss further the results of the present measurements, and how they can be reconciled with other time domain and static measurements on Si.

To begin with, the LO phonon frequency should be red-shifted for doped Si with respect to values characteristic of intrinsic Si, due to the indirect band gap shrinkage [84] induced by exchange and correlation terms of the electronic Hamiltonian in the presence of doping carriers [148]. The phonon spectra (inset Fig. 47) obtained by FT the reflectivity data over the whole delay time range show the LO frequency peak shifting towards lower values with increasing photoexcitation intensity, and exceeding the literature value of 15.6 THz measured for the LO phonon in nonexcited intrinsic Si for all the pump fluencies. In time-domain, the frequency shows the expected red shift at time zero, and recovers to the Raman value in about 2 ps: at later delay times (Fig. 51); however, at later time delays the frequency continues to a blue shift with respect to the unexcited value. This blue shift can be clearly seen for the LO frequency vs. calculated carrier density curves (Fig. 53b): although the curves should converge to the same

pump power independent frequency after the sample returns to its unexcited state, it is obvious that for different initial photoexcited carrier densities the frequency reaches the same value at different carrier concentrations. The free (hot) carriers and the lattice heating created by illumination should contribute in equal amounts to the renormalization of LO phonon in all samples, for the same initial excitation power. The difference seen between differently doped samples should be therefore attributed in part to the doping. Also, to explain the fact that, for different excitations, the frequency is different at the same carrier density, there has to be a contribution from a mechanism that produces a blue shift of the frequency on the picosecond time scale, and counteracts the red shifts created by the free carriers and the heating of the lattice. The free carriers weaken the atomic bonds and therefore decrease the phonon frequency. The temperature increase produces dilation of lattice and acts as a tensile stress weakening the bonds. The extra mechanism needed to explain the data should have as an effect the strengthening of the atomic bonds, i.e., it should act as a compressive stress. This mechanism is provided by a contraction of the lattice in response to free carrier photogeneration. As detailed in Section 2.6, Wright and Gusev [103] measured a surface deformation, produced by low intensity 200 fs, 630 nm pulses on Si, by performing beam deflection measurements, i.e., the probe spot was displaced from the pump spot and the carrier density dependent contraction of the surface caused the beam deflection. They explain the surface contraction detected by the presence of a tensile stress created by the photoexcited plasma along the direction normal to the surface. The initial carrier density in the L-valleys is responsible for the initial lattice softening that is induced by photoexcitation. This is consistent with the photostriction effect observed in Ge, where the indirect band gap leads to L-valley population [141]. On sub-picosecond time scale the L- to X-valley transfer occurs. The relevant X-valley effective deformation potential has opposite sign

than for the L-valley, leading to the lattice contraction and to eventual formation of a compressive strain pulse that was observed by Wright, Gauster and others [33, 103, 105]. The results of Ref. [103] show maximum contraction at early times, and recovery on a much longer times (>100 ps) than we can follow the LO phonon frequency; their study, however, does not resolve the onset of the contraction, which is probably limited by the excitation of carriers directly to the X-valley by their picosecond excitation pulse. Based on published data, p-doped samples undergo a larger LO phonon frequency red shift due to free carrier contribution than n-type samples. In the case of photoexcited carriers, however, we observe lower values of LO phonon frequency for n-type, rather than for p-type Si. The origin of this difference is not understood, but we note that p-type samples undergo larger amplitude contraction of the lattice due to photoexcited carriers then the n-type samples [103].

Regarding the LO phonon dephasing rate, Hart & al [142] measured the linewidth and the frequency of zone-centered optical phonons in Si(111) between 20-770 K; the effect of lattice temperature on the LO phonon linewidth, with the assumption that the optic phonon decays into two LA phonons of equal energy and opposite momentum, was found to be well described by Eq. 4.9. The same dependence was found by Hase et al. [149] to fit well experimental results on bismuth. The nonlinear behavior we obtained for pump powers over 30 mW, however, suggests that the LO phonon dephasing also depends on the coherent phonon amplitude, or the carrier density, in a nonlinear manner, which may arise from anharmonic effects or contributions to the pure dephasing rate and other contributions [99]. The LO phonon frequency itself depends on the lattice temperature, correction not taken into consideration in Eq. 4.1. Even corrected for the lattice temperature effect, the LO phonon dephasing rates we measure deviate from linear dependence of free carrier density for pump powers higher than 30 mW. We note, for example,

that the longitudinal and transverse gradients in the electron density and temperature will create dispersion in coherent phonon frequencies; this inhomogeneous distribution of excitation may cause the dephasing of coherent phonon oscillations when the signal is averaged over the observation volume.

4.2.4 Summary

We measured the LO phonon frequency and dephasing rate change for ~6 ps after excitation with various intensities. The observed phonon frequency decreases within the laser pulse and evolves slowly for the first 500 fs possibly even decreasing further. After this initial softening, the lattice hardens due to the L- to X-valley scattering. At delay times of about 2 ps, the LO phonon reaches its characteristic value for unexcited Si. The recovery of phonon frequency overshoots the static phonon frequency on few picosecond time scales on account of the photostricive effect of X-valley carriers. The analysis of the frequency chirp for different pump powers yields the expected result that, as the pump power decreases (less number of carriers excited initially), the lattice softens less, and the phonon frequency is chirped by a smaller amount. The analysis also reveals that the nonlinearity of the chirp has contributions from the lattice temperature increase and the contraction of the lattice due to electronic contributions. The phonon dephasing rate is decreasing as the carrier density increases, the manner in which it depends of the carrier density at pump powers larger than 30 mW clearly showing the onset of nonlinear effects. In summary, the coherent LO phonon self-energy provides a complex picture of the transient carrier dynamics in Si.

4.3 POLARIZATION DEPENDENCE

The focus of this section is on the effect on the LO phonon amplitude of the pump and probe polarizations orientation with respect to the crystalline lattice of Si. Si has three degenerate optical phonon branches at the Γ point (see Section 2.2.2). Polarized light excites selectively the phonons according to the symmetry of the corresponding Raman tensor. The 400 nm light used in our experiments is incident on the sample with the pump and probe *k*-vectors near-parallel with its [001] crystalline axis. Because the photon momentum is small and the light penetration depth is ~100 nm, the zone-center LO phonon mode is excited. We expect both pump and probe pulses to interact with the coherent phonon in the same way, due to the common symmetry of the Raman tensor describing the LO phonon generation and detection.

We perform experiments in the anisotropic geometry described in Section 3.4 keeping the probe polarization fixed and rotating the pump polarization around the [001] crystalline axis of the sample. In the isotropic geometry, the pump polarization is fixed and the probe polarization is rotated in the same plane.

4.3.1 Pump polarization rotation

For this experiment the probe polarization is fixed along the [100] crystalline direction, and the pump polarization is rotated in the (001) plane. The angle of rotation θ is defined with respect to the [110] axis, as shown in Fig. 55a.

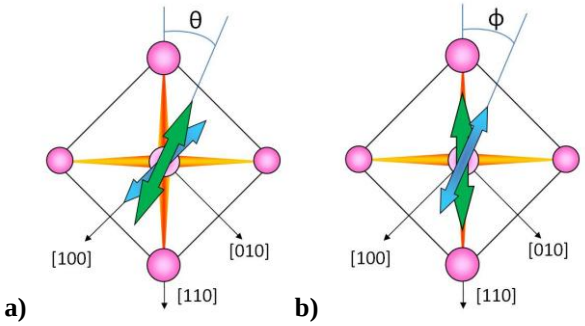

Figure 55: Pump and probe polarizations orientations with respect to the crystalline lattice for a) pump, and b) probe polarization rotation measurements.

From the transient reflectivity signals (Fig. 56) it is clear that the amplitude of the oscillatory component varies with the relative rotation angle θ.

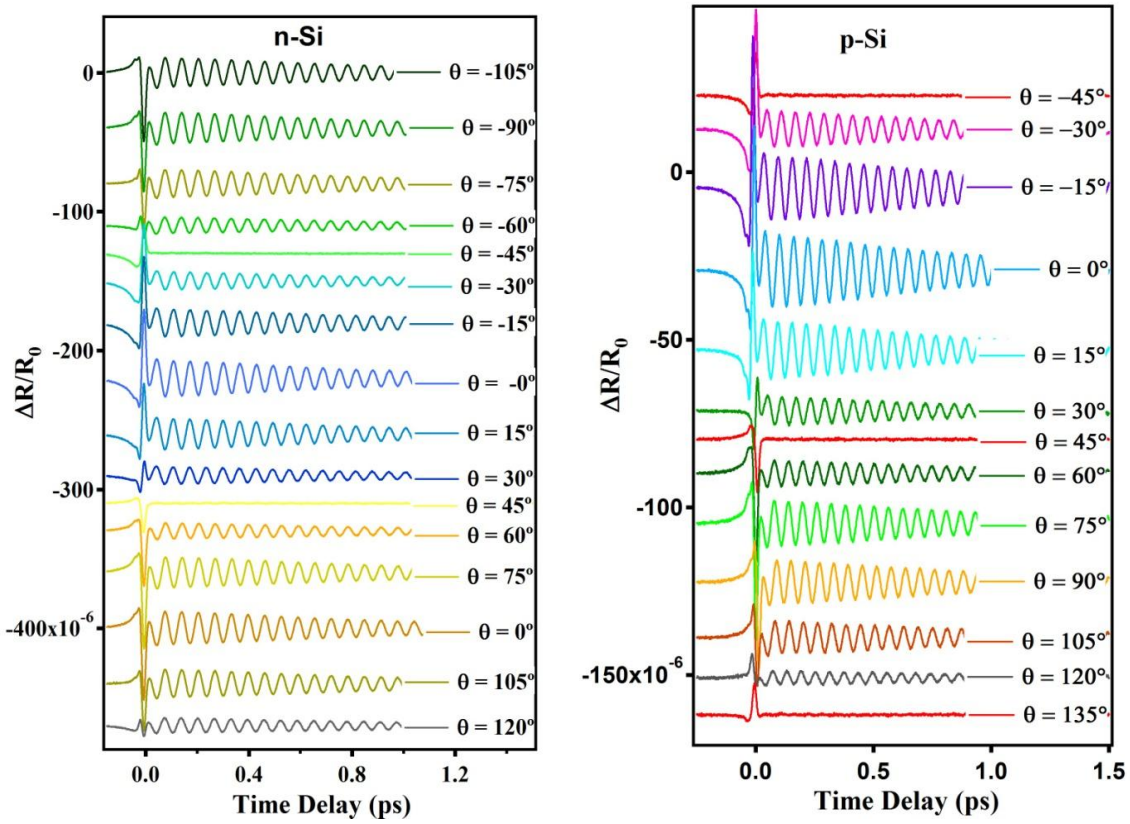

Figure 56: Transient reflectivity data as a function of pump polarization for n-and p-doped Si.

To retrieve the amplitude of the oscillatory part we fit the reflectivity data with $f(t) = A\exp(-t/\tau)\cos[2\pi\omega_{LO}(t)t + \varphi]$, where the fitting parameters are: the initial amplitude of

the oscillation *A*, damping time τ, oscillation frequency $\omega_{LO}(t)$, and the initial phase of the oscillation φ. We let the coherent LO phonon initial (i.e. at time zero) amplitude, frequency and decay time to be the fitting parameters. The amplitude of oscillation at time zero obtained for n-type Si is presented in Fig. 57, as a function of pump rotation angle θ.

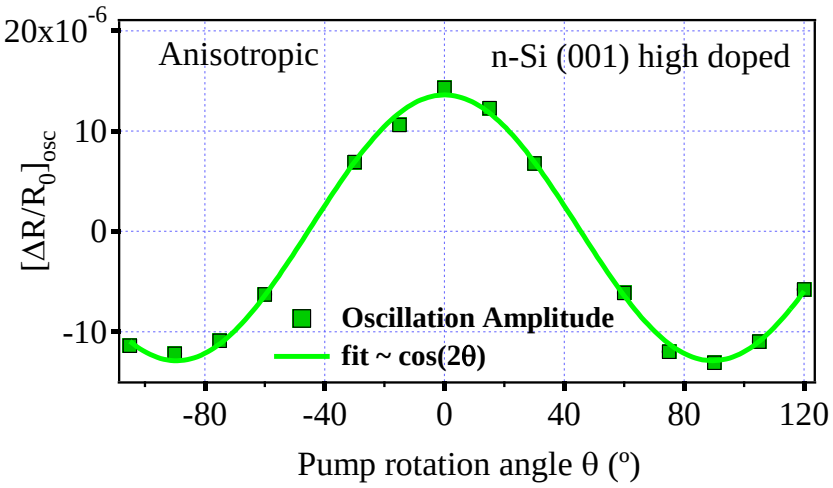

Figure 57: The amplitude of coherent phonon as a function of the angle θ, fitted to a cosine function.

The amplitude of oscillation varies as $\cos(2\theta)$ with the pump polarization angle θ, as it can be seen in Fig.57. This dependence is easily verified theoretically through a simple matrix multiplication. For traditional Raman scattering, the Raman intensity is proportional to $\left(\vec{e}_i^{\,T}\,\vec{\vec{R}}\,\vec{e}_s\right)^2$, where $\vec{e}_i^{\,T}$ is the transposed unit vector of polarization of the incident photon, and $\vec{e}_s$ indicates the polarization direction of the scattered photon. $\vec{\vec{R}}$ is the Raman tensor associated with the phonon involved in the Raman transition, which in our case is the LO phonon. When the phonon is generated by a pair of frequencies within the same pulse, $\vec{e}_i$ and $\vec{e}_s$ must be both parallel to the polarization of the pulse. The change in reflectivity due to the phonon oscillation is proportional to the Raman intensity. To calculate the dependence of phonon amplitude on the pump polarization angle of rotation θ with respect to the [100] axis, the Raman tensor can to be

transformed according to a rotation around [001] with angle θ. The Raman tensor thus becomes $\vec{\vec{R}}^{\theta} = T(\theta)^{T}\,\vec{\vec{R}}T(\theta)$, where $T(\theta) = \begin{bmatrix} \cos\theta & \sin\theta & 0 \\ -\sin\theta & \cos\theta & 0 \\ 0 & 0 & 1 \end{bmatrix}$. The amplitude of the coherent phonon is proportional to the product $\vec{e}_i^{\,T}\vec{\vec{R}}^{\theta}\vec{e}_s$. Performing the required matrix multiplications with the Raman tensor defined by R_3 in Eq. 2.13 [58, 60], we obtain $\vec{e}_i^{\,T}\vec{\vec{R}}^{\theta}\vec{e}_s = 2d\cos(2\theta)$, where θ is the pump polarization angle with respect to the [110] crystalline direction of the Si sample, and *d* is the magnitude of the non-zero components of the LO phonon Raman tensor. The amplitude of phonon is, therefore, proportional to $\cos(2\theta)$. The coherent phonon is generated impulsively, displacively, or by both mechanisms simultaneously. The impulsive generation is revealed by a sine-like oscillation of the phonon amplitude (zero amplitude at time zero), and the displacive generation will impose a cosine-like oscillation of the phonon amplitude (maximum amplitude at time zero). In polar semiconductors, such as GaAs, these mechanisms can give rise to isotropic and anisotropic generation mechanisms. This means that the amplitude of the phonon, which is proportional to the transient reflectivity change, will consist from an isotropic contribution independent of pump polarization rotation, and an anisotropic variable contribution. The amplitude of the LO phonon will still have a $\cos(2\theta)$ dependence, but the amplitude vs angle θ curve will be shifted up or down by the amount of the isotropic contribution. In homopolar Si (001), excited with linearly polarized light, both coherent phonon generation mechanisms are anisotropic. The amplitude of the phonon will be, therefore, defined by a function $A\cos(2\theta)$, as shown in Fig. 57, where *A* is a constant that includes contributions from both mechanisms and θ is the angle the pump makes with [110] crystalline axis.

Another observable in the oscillatory part of the reflectivity data is the sign of driving force. The driving force undergoes a π phase shift each time the pump polarization is rotated by 90°. The change in the direction of the impulsive force that launches the coherent LO phonon is associated with which of the two pairs of equivalent bonds of the tetrahedrally coordinated Si lattice are excited [see Fig. 58].

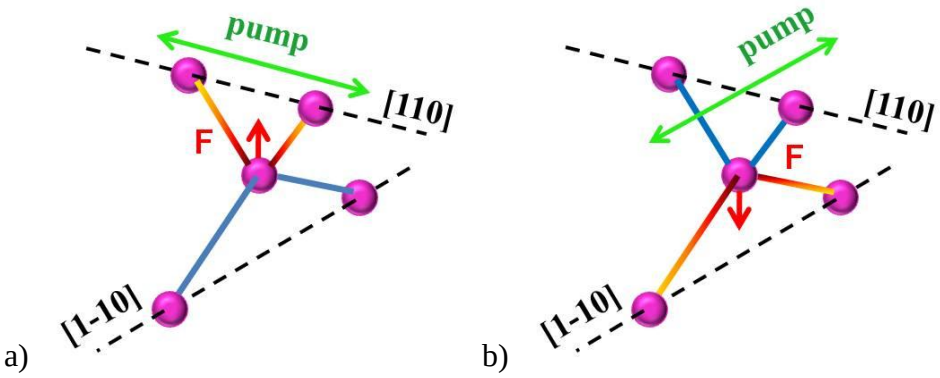

Figure 58: Schematic representation of the excited bonds (red-yellow hues) of tetrahedral Si: a) pump polarization parallel to $[110]$**, and b) pump polarization parallel to** $[1\bar{1}0]$**. F denotes the driving force acting.**

4.3.2 Probe polarization rotation

To study the effect of the probe polarization orientation on the LO phonon, we perform isotropic measurements of the transient reflectivity. We rotate the probe polarization by an angle φ with respect to [110] crystallographic direction along which the pump polarization is kept parallel throughout the experiment (as in Fig 55b).

The transient reflectivity data obtained for this experiment are shown in the Fig. 59. The oscillation of the transient reflectivity change with the angle φ follows a $\cos(2\varphi)$ dependence

(Fig. 60), which proves that the probing of coherent LO phonons occurs via the same mechanisms as their generation.

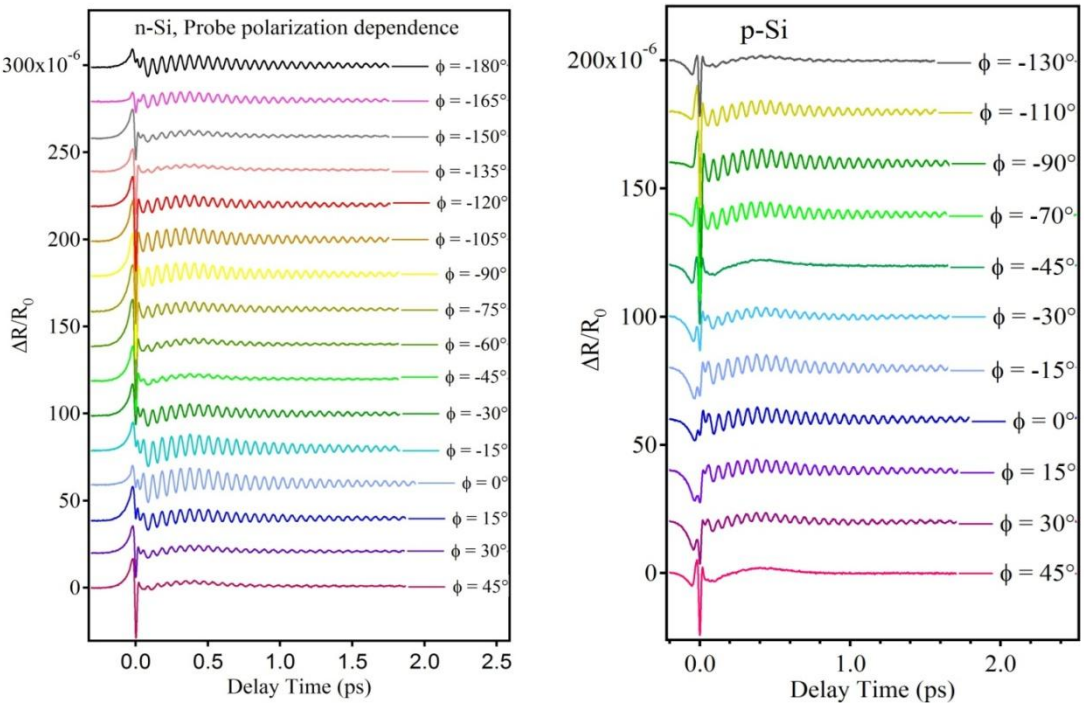

Figure 59: Transient reflectivity data for n- and p-Si as a function of probe polarization rotation angle.

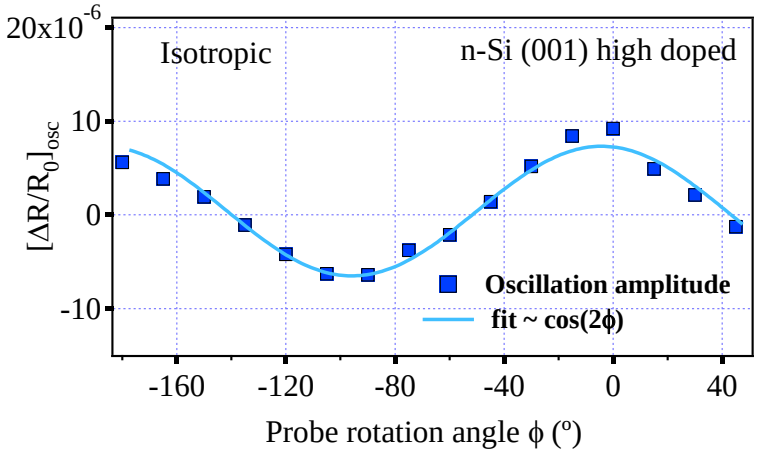

Figure 60: The coherent LO phonon amplitude vs. probe polarization rotation angle φ.

An interesting finding comes from the FT spectra of the transient reflectivity. In Fig. 61 are shown FT spectra of the transient reflectivity signals of p-Si high doped sample, measured for pump angular rotation around the [110], respectively $[1\bar{1}0]$ crystalline axes.

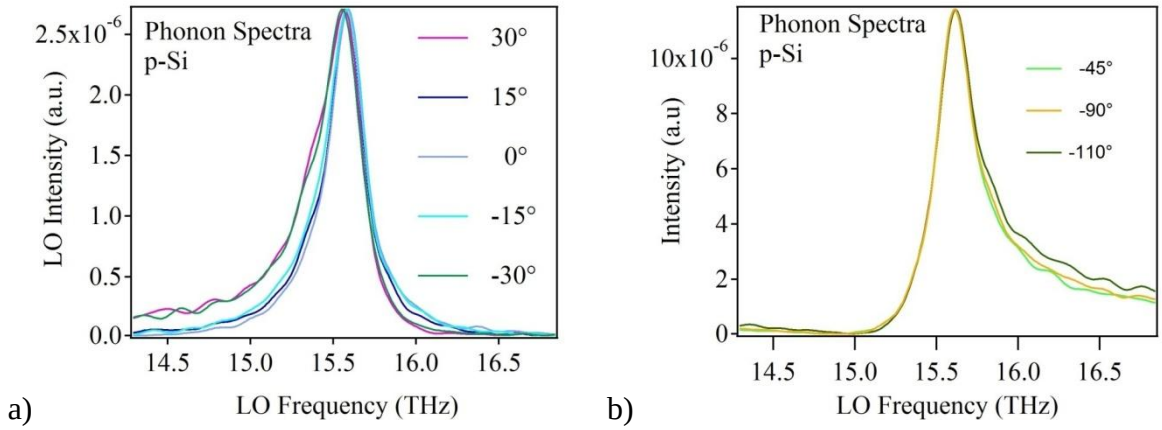

Figure 61: LO phonon lineshape for various probe polarization angles (p-Si high doped). Probe polarization parallel to and pump polarization rotated around the [110] **(a), respectively** $[1\bar{1}0]$ **crystalline.**

The FT spectra (Figs. 61) show Fano line shapes with opposite asymmetry indicating that the asymmetry parameter (q) in the Fano lineshape changes sign when different pairs of bonds are excited (see Figs.55 and 58). In the Fano interference (see Section 4.4.2) observed for doped Si [40], the sign of asymmetry parameter has been attributed to whether the interaction responsible for the interference is the hole-LO phonon interaction ($-q$) or the electron-LO phonon interaction ($+q$). In our case, the sign change in Fig. 61 seems to come from the change of sign of the electronic Raman tensor [150, 151] in between the two experimental configurations shown in Fig. 58. In Figs. 56 and 59 one can clearly see that the electronic Raman tensor changes sign, and the LO phonon oscillation phase changes by π, each time the pump, respectively the probe polarizations rotate by 90° with respect to the [110] crystalline axis. The expression defining the asymmetry parameter q (Eq. 4.15) includes the electronic Raman tensor at the denominator, and the phonon Raman tensor, which was found to be negative for excitations below the 3.3 eV

direct band-gap of Si [151], at the numerator. The change of sign for the Raman spectra asymmetry arises therefore from the change of sign of the electronic Raman tensor.

4.3.3 Summary and conclusions

The amplitude of the coherent phonon signal depends on the polarization vectors of both pump and probe pulses with respect to the crystallographic directions in the (001) surface plane. The dependence shows a cosine of twice the angle between the two polarization vectors and the [110] axis. The same manner polarization angle dependence is not a surprise, as both generation and probing of the phonons involve the coupling of light with the Raman tensor of $\Gamma_{25'}$ symmetry. Both pump and probe pulse polarization influence the amplitude and initial phase of the phonon oscillation due to the similarities between the mechanisms for the generation and detection of the coherent phonon, which both involve the coupling of light with the Raman tensor.

We performed these experiments in order to verify if there are generation and detection mechanisms of coherent phonons in Si of different symmetry. For instance DECP and ISRS excitation mechanisms could have different origins that are described by different symmetry Raman tensors. Whatever mechanisms are involved, they appear to have the same symmetry, and therefore cannot be distinguished through the polarization dependence analysis.

4.4 PUMP PULSE WAVELENGTH DEPENDENCE

In this section we describe experiments that address the mechanisms for excitation of the zone-center coherent LO phonons. We analyze the transient reflectivity change in Si(100) for excitation photon energies approaching its direct band-gap of ~3.3 eV. The measured signals contain an oscillatory component attributed to modulation of the sample's index of refraction by coherent LO phonons. We discuss the generation mechanisms of LO phonons for near-resonant electronic excitation by analyzing the change of its initial phase. We also study the LO phonon oscillation amplitude and the LO phonon complex self-energy as functions of the excitation wavelength.

4.4.1 Theoretical background

The generation of coherent phonons has been extensively discussed in literature for the last two decades. The proposed mechanisms for exciting coherent Raman active phonons in materials with diamond and zinc-blende structures are referred to as the impulsive stimulated Raman scattering (ISRS) [66] and the displacive excitation of coherent phonons (DECP) [7, 68, 152]. ISRS generally occurs in transparent media and DECP in opaque media, but as we shall see, both mechanisms can occur concomitantly, particularly in opaque media. Both mechanisms require an exciting laser pulse with duration shorter than the phonon period, and involve nearly instant onset of coherent lattice vibrations driven by forces created during the pump laser illumination of the sample. The difference between these two mechanisms resides in the nature of the forces. ISRS involves virtual electronic excitations; the atoms are subject to a driving force proportional to the Raman tensor. This is an impulsive delta function-like force, initiating sine-like oscillation

of the atoms from their quasi-equilibrium positions, i.e., the ground state. By contrast, DECP involves real transitions between the valence and conduction bands, i.e., transitions from the mainly bonding states to the antibonding states, and the photoexcited electrons couple with the phonons by exerting a displacive force on the nuclei. This force is a step-like function of time that is proportional to the nonequilibrium carrier density, i.e., the photoinduced charge density fluctuations. The excitation induces a shift of the nuclear potential with respect to that of the ground state, forcing atoms to undergo coherent motion towards their new equilibrium positions. Because at the time of excitation the atoms are at their maximum displacement from the excited state equilibrium position, their oscillation has cosine-like dependence on time. For both mechanisms, the oscillation follows the equation of motion of a damped harmonic oscillator (Eq. 2.14).

A more general description of the excitation mechanism that encompasses both mechanisms for opaque samples has been proposed by Stevens et al. [75], and applied to the specific case of diamond structure materials by Riffe et al. [76]. Stevens et al. [75] argues that two tensors contribute to the stimulated Raman scattering. One is given by the classical Raman susceptibility tensor and the other one is due the electrostrictive force caused by real anisotropic charge carrier excitations. Both the Raman and the "electrostrictive" tensors are complex quantities. Their real parts equal the Raman tensor in the absence of absorption. In the case of transparent materials the tensors are, therefore, identical, whereas for absorbing media the imaginary part of the "electrostrictive" tensor can be more than one order of magnitude larger than that of the Raman tensor [75]. Within this theory, the authors conclude that the coherent phonon driving force through Raman susceptibility contains both impulsive and displacive components, and takes the form:

$$F(\Omega) \propto \left[\frac{d\,\mathrm{Re}(\varepsilon)}{d\omega} + 2i\frac{\mathrm{Im}(\varepsilon)}{\Omega} \right] \int_{-\infty}^{+\infty} e^{i\Omega t} |E(t)|^2 \, dt, \qquad \text{Eq. 4.11}$$

where $\varepsilon(\omega)$ is the linear dielectric tensor, Ω the phonon frequency, ω the laser pulse frequency, and $E(t)$ the exciting electric field at time *t*. The displacive component of the force becomes relevant as the transitions involved approach resonance with the material's band-gap, i.e. as the excitation field can couple to real charge density fluctuations.

Riffe and Sabbah [76] extend the model of Stevens by considering the finite lifetime of the electrostricitve force, particularly in the case of Si. They theoretically formulate the excitation photon wavelength dependence of the initial phase of the oscillation and express the total initial phase of LO phonon by:

$$\phi = \arctan\left(\frac{\frac{\Omega}{2\varepsilon_2}\frac{d\varepsilon_1}{d\omega} + \frac{\gamma}{\Omega} - \frac{\beta}{\Omega}}{1 - \frac{\Omega}{2\varepsilon_2}\frac{d\varepsilon_1}{d\omega} \times \frac{\gamma}{\Omega}} \right), \qquad \text{Eq. 4.12}$$

where the quantities involved are: the phonon frequency (Ω) and decay time (β), the real and imaginary parts of dielectric constant $\varepsilon = \varepsilon_1 + \varepsilon_2$, and the decay time γ of the anisotropy in the photoinduced carrier distribution. With Eq. 4.12, Riffe and Sabbah calculated the initial phase of the LO phonon vs. excitation wavelength for Si (Fig. 69). They assumed a constant contribution of 23° to the phonon initial phase from the displacive mechanism. This constant contribution was an ad hoc assumption that permitted the theoretical curve to be shifted into correspondence with two experimental data points for 800 and 400 nm measurements.

Our results on Si, obtained for excitation wavelengths tuned around 400 nm, strongly deviate from the predictions of Riffe et al. As we will see in the experimental part of this work, the initial phase of the phonon changes dramatically when the excitation photon energy

approaches resonance with the direct band gap in a manner that contradicts the theoretical model of Riffe et al. Furthermore, we find that the initial amplitude of the LO phonon changes with the wavelength probably in part because of its dependence on the photoexcited carrier density. The initial LO phonon frequency and its decay time are independent of the excitation wavelength, but the phonon spectra show asymmetric Raman lineshapes, with the asymmetry increasing as the excitation phonon approaches resonance with the ~3.3 eV direct band gap of Si. This asymmetry is a manifestation of a Fano interference involving the coupling of charge density fluctuations and phonons through optical excitation and residual deformation potential interaction. The analysis of the Fano profile provides the most direct window on the phonon excitation mechanism beyond the description by Stevens [75] and Riffe et al. [76].

4.4.2 Experimental data and analysis

We perform pump-probe transient EO reflectivity experiments on four Si(100) samples with various doping densities (all samples are n-type; samples 1,2,3 are of unknown doping densities, whereas sample 4 has a resistivity of 0.05 Ω·cm corresponding to a doping density of 1.2×10^{19} cm^{-3}). The experimental set-up and measurement technique used are described in Chapter 3 and Section 4.1.1.

The wavelength of the pulses is tuned from 385 to 405 nm by changing the phase matching angle of a 50 μm thick BBO crystal for second harmonic generation (SHG); the tuning range is limited by bandwidth of the Ti:Sapphire oscillator. The angular acceptance angle of the BBO crystal is too small to double the entire bandwidth of the fundamental, and therefore the crystal angle can be used to select a particular wavelength range. Although the tuning range of the crystal is not large, it is sufficient to see a clear trend in the coherent phonon response. The

excitation power is maintained constant for all measurements: the pump power used for measurements on samples 1, 2, 3 was 21 mW, and for sample 4, 34 mW.

At the instant of excitation there is a contribution to EO sampling signal from the initially excited nonthermal anisotropic distribution carriers, which decays toward an isotropic distribution in *k*-space through momentum scattering on <100 fs time scale. This initial transient is defined by the pulse duration and the response of resonantly excited e-h pairs, and is followed by an oscillatory component attributed to the modulation of the sample index of refraction by the LO zone-center phonon. The nonthermal carrier and coherent phonon contributions are entangled, as described in Ref. [127]. From the transient reflectivity signals measured at different excitation wavelengths it can be seen that the initial phase is quite sensitive to the excitation wavelength (Fig. 62). To extract the LO phonon parameters of interest (initial phase, amplitude, frequency and decay time), the transient reflectivity signal is differentiated with respect to the time delay in order to remove the residual slow electronic contribution from the oscillatory signal. We fit the differentiated signal with a function

$$f(t) = A\exp(-t/\tau)\sin[2\pi\omega_{LO}(t)t + \varphi], \qquad \text{Eq. 4.13}$$

where the fitting parameters are: the initial amplitude of the oscillation *A*, damping time τ, oscillation frequency $\omega_{LO}(t)$, which includes the chirp as a 3rd degree polynomial, and the initial phase of the oscillation φ. From the fit parameters we can reconstruct the oscillatory part of the signal (Fig. 62b).

The initial phase has some uncertainty with respect how one defines the time origin. Zero can be defined either as the point where the reflectivity change has the steepest slope (Fig. 62b), or as the point of minimum reflection in the initial reflectivity transient. The difference in phase for these two definitions can be as large as ~30 degrees (~5 fs). Independent measurements of

zero delay, using for instance a transparent sample with instantaneous response, suffer from uncertainty arising from the requirement to perform optical alignment for each sample.

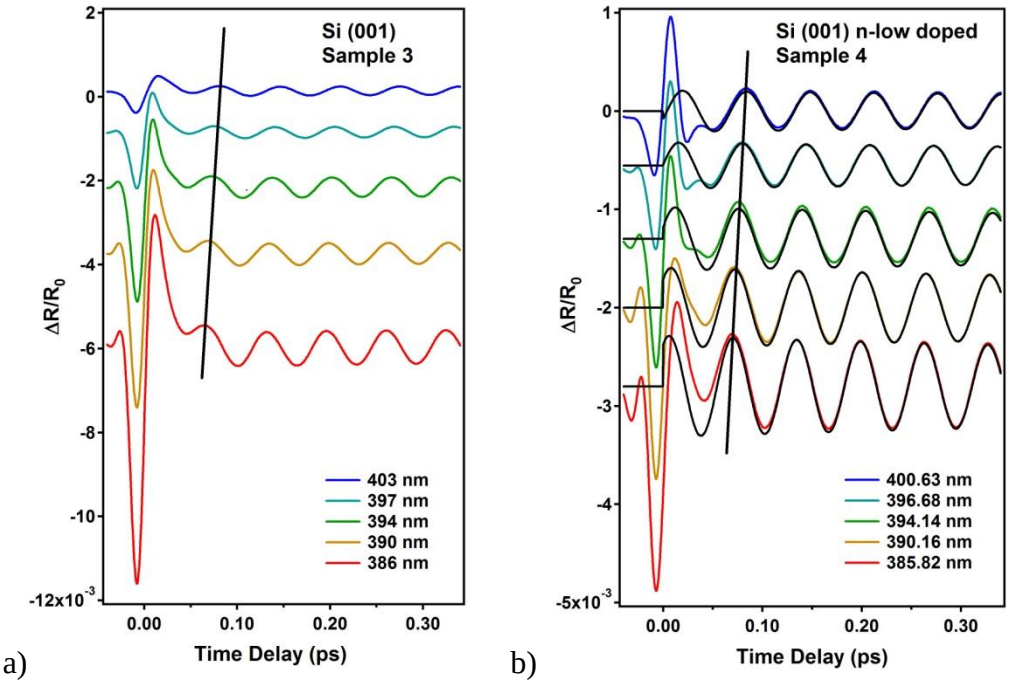

Figure 62: a) Transient reflectivity (sample 3) and b) transient reflectivity (sample 4) for various pump wavelength. Contributions of LO phonon to the transient reflectivity reconstructed from fit parameters (black curves). Black oblique line emphasizes the phase change.

By performing a Fourier Transform of the reflectivity signals, we obtain the FT spectra of the signals showing the LO phonon peak close to its expected value of 15.6 THz (Fig. 63); it is evident that the LO phonon feature shows an asymmetric Fano lineshape, with asymmetry increasing as the excitation wavelength approaches resonance with the ~3.3 eV direct band-gap energy of Si. The asymmetric Raman line shape is characteristic to a discrete state which is embedded within a continuum of states, with the discrete state and the continuum coupled by the excitation and a residual interaction. The two-path interference in the case of Si LO phonon spectra presented in Fig. 63 results in a destructive interference on the low energy side of the LO phonon peak and a constructive interference on the high energy side. The positions of the

destructive and constructive interference depend on the pump and probe polarizations, as shown in Fig. 61. Such spectral interference was studied first by Fano [123] in order to explain the asymmetric shape of autoionization resonances in noble gas atom absorption spectra. In Fano's formulation the line shape created by the interfering pathways takes the form:

$$I(\omega) \approx \frac{(q+\varepsilon)^2}{1+\varepsilon^2}, \qquad \text{Eq. 4.14}$$

where $\varepsilon = \frac{(\omega - \Omega)}{\Gamma}$ is a dimensionless energy measured from the "dressed" phonon frequency Ω, with Γ gives the strength of the coupling between the discrete and continuum states.

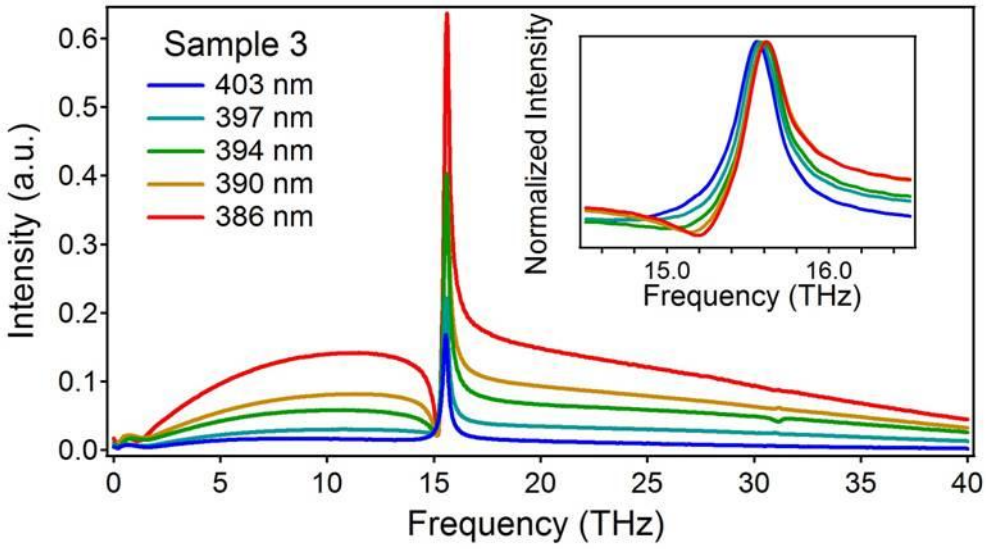

Figure 63: The Fourier spectra of the coherent LO phonon response of Sample 3 for different excitation wavelengths.

The asymmetry parameter (line profile factor) is expressed as

$$q = \frac{R_p}{\pi V_{e-ph} R_e}, \qquad \text{Eq. 4.15}$$

where R_p and R_e represent the transition amplitudes for the discrete and continuum excitations, and $V_{e\text{-}ph}$ represents the residual interaction between them. In the case of Si, R_p and R_e represent

the Raman tensor elements for the excitation, respectively, of LO phonons and charge density fluctuations; V_{e-ph} is the electron-phonon interaction matrix element that couples the charge density fluctuations to LO phonon [151]. Together, these parameters determine the sign and magnitude of *q*. In the definition of ε, $\Omega = \Omega_0 + \delta\Omega$ is the frequency of the discrete state (LO phonon in our case) dressed by the interaction with the continuum; $\delta\Omega$ and Γ correspond to the real and imaginary parts of the self-energy that the phonon gains through the electron-phonon interaction. If we denote by Φ the discrete state renormalized by the interaction with the continuum, by φ the unperturbed discrete state, and by Ψ_E the continuum states, than the electron-phonon coupling matrix element of the Hamiltonian H of the system can be expressed as $V_{e-ph} = \langle \Psi_E | H | \varphi \rangle$. With this notation the asymmetry parameter is described by

$$\Gamma q^2 = \frac{1}{\pi} \frac{\left| \langle \Phi | H | i \rangle \right|^2}{\left| \langle \Psi_E | H | i \rangle \right|^2} \approx \left(\frac{R_p}{R_e} \right)^2 . \qquad \text{Eq. 4.16}$$

Here $\left| \langle \Phi | H | i \rangle \right|^2$ is the transition probability from the ground state of the system to the discrete state, $\left| \langle \Psi_E | H | i \rangle \right|^2$ is the transition probability from the ground state to the continuum of states, and the coupling of the discrete state with the continuum is defined in terms of the broadening:

$$\hbar\Gamma = \pi \left| V_{e-ph} \right|^2 . \qquad \text{Eq. 4.17}$$

The physical meaning of the broadening parameter Γ is, therefore, the strength of the discrete state-continuum interaction for the Raman experiments; its counterpart in time-domain experiments is the coherent phonon dephasing rate by carrier-phonon scattering.

To conclude this section, the experimental data recorded clearly show changes in the amplitude and phase of the LO phonon with the excitation wavelength. The corresponding FT

spectra show a clear shift of the LO phonon peak frequency and also the Fano interference between phonons and carriers.

4.4.3 Discussions and conclusions

In this section we analyze how and why different parameters describing the LO phonon vary when the excitation wavelength approaches resonance with the direct band-gap of ~3.3 eV of Si.

4.4.3.1 LO phonon frequency vs. excitation wavelength

In this section we discuss two quantities: the initial LO frequency (at time delay zero) obtained by time-domain fitting of the transient reflectivity data, and the "dressed" LO phonon frequency obtained by fitting of the Fano-like shaped Raman lines obtained by the FT analysis (Fig. 64).

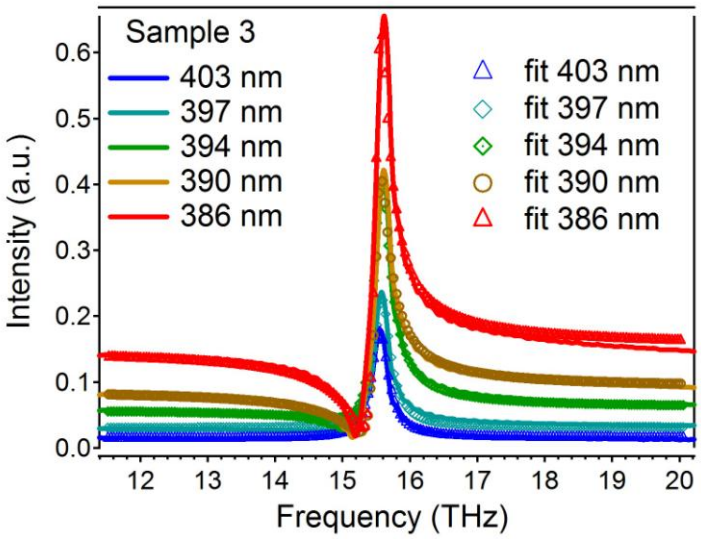

Figure 64: LO phonon Raman lines with the corresponding Fano-fit function (Eq. 3).

The initial (time zero) LO phonon frequencies of Si, obtained by fitting the transient reflectivity signal at different wavelengths to Eq. 4.13 do not reveal any wavelength dependence trend. As for the LO phonon FT spectra peak, in the inset of Fig. 63 is clearly visible that the

position of the maximum is shifting when the excitation wavelength varies. We observe also that, as the excitation wavelength approaches resonance with the direct band gap of Si, LO phonon lineshape asymmetry increases and the anti-resonance (dip) becomes more pronounced. It was already established that the LO phonon frequency should not depend on the excitation wavelength [124, 139]. However, the maximum of the Raman line does not correspond to the real frequency of the phonon, departing from the LO phonon real frequency because of the asymmetry of the line introduced by the interference between the discrete phonon line with the continuum provided by the excited carriers [124]. We fit the FT spectra to the Fano function described by Eq. 4.14, letting the asymmetry parameter q, the LO phonon frequency Ω and the broadening parameter Γ be the fit parameters. The Fano-fit parameters obtained for Sample 3 are listed in Table 3.

Table 3: Fit parameters for various excitation wavelength values for Sample 3.

λ (nm)	q	Ω (THz)	Γ (THz)
403	42.05	15.56	0.149
397	5.38	15.546	0.138
394	3.29	15.55	0.136
390	2.18	15.53	0.128
38	1.96	15.52	0.119

In Fig. 65a and Table 3 are presented the wavelength dependence of the LO frequency and broadening parameter Γ, and of the inverse of the asymmetry parameter, q^{-1}. Similar Fano lineshape analysis has been performed for doped (*n* and *p*) Si samples for nonresonant excitation conditions (with respect to the E_1 critical point) by Cardona and coworkers [124, 139]. In these

measurements, it was found that the inverse of the asymmetry parameter shows a linear dependence on the excitation wavelength, and Γ is sensitive to the carrier density as it measures the electron-phonon interaction strength. Our analysis also shows that the inverse of the asymmetry parameter varies inversely with the excitation wavelength for near resonant conditions, but not with the trend extrapolated from the nonresonant measurements.

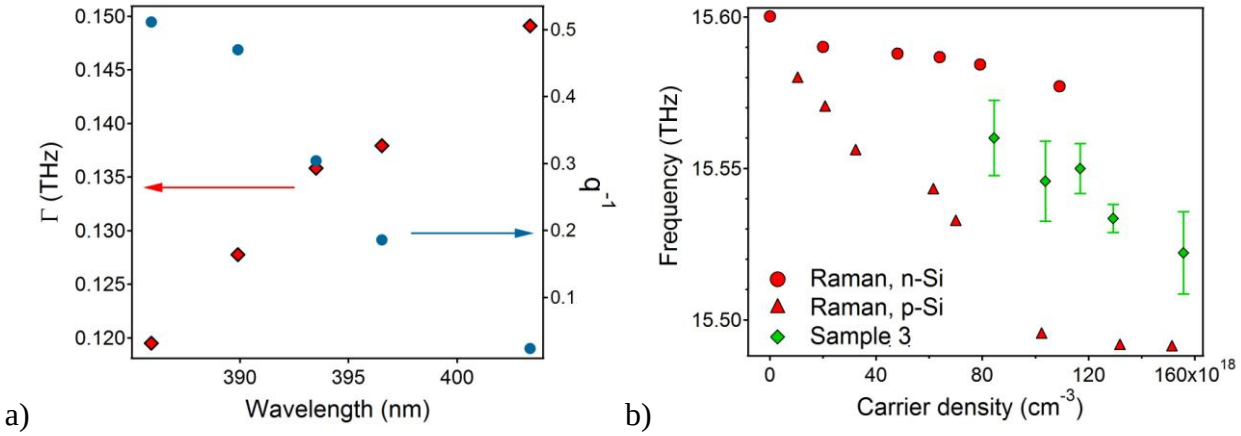

Figure 65: a) Broadening parameter Γ and inverse of the asymmetry parameter q^{-1} vs. wavelength, and b) LO phonon frequency and Raman frequency of n- and p-type Si [28] vs. estimated carrier density.

Next we address the excitation wavelength dependent LO phonon frequency and dephasing rate. Recall that in Subchapter 4.2 we analyzed two physical quantities shown to change the LO zone-center phonon of Si: the total free carrier density, including both the doped and photoexcited carriers, and the rise in the lattice temperature, which is established through equilibrium with environment or through the carrier-lattice energy transfer. Let us first consider the influence of the lattice temperature for the specific case of excitation wavelength dependent measurements.

As the sample temperature increases, the LO phonon frequency of Si decreases while its dephasing rate increases [98]; the rate at which the LO phonon frequency changes with the temperature depends on the doping concentration of the sample [99]. We numerically calculated

the photoexcited carrier density and lattice temperature time delay dependent profiles of Si for the experimental conditions involved in this work (Chapter 5). The calculations show the lattice temperature increasing by a maximum of 17 K for a pump fluence of 1.18 $mJ \cdot cm^{-2}$ (21 mW pump power), and of 30 K for the pump fluence of 1.96 $mJ \cdot cm^{-2}$ (35 mW). Using the temperature dependence found by Huang et al. [99] for the LO phonon frequency, we estimate a frequency decrease (with respect to the value of 15.61 THz for the LO phonon frequency at room temperature) of ~0.1% for 21 mW pump power, and of less than 0.2 % for the 35 mW excitation. These estimates are based on the assumption that the LO phonon frequency is 15.61 THz, but other sources report a Raman phonon line of 15.6 THz or less at room temperature, in which case the change will be even smaller. Also, our calculations show the lattice temperature reaching its maximum value at ~1.5 ps after excitation for both fluencies involved in this work, and as the FT spectra of the transient reflectivity is an average over the whole delay time interval, if follows that the change of the LO phonon frequency with the temperature is smaller even than the changes we estimated above, and this effect can be neglected here.

Let us now consider the contribution of the free carrier density to the LO phonon frequency. The increase in doping impurities results in the reduction of the LO phonon frequency (Section 2.2), and the same effect is shown to occur in the case of optically injected carrier densities (Subchapter 4.2). The experimental works of Aspnes [153] and Jellison [85] show that absorption properties of Si change both with the exciting wavelength and the doping carrier density (Fig. 66). We neglect the doping dependence, and estimate the photoexcited carrier density as a function of wavelength. The photocarrier density depends on the excitation fluence and on the optical constants of the sample. The calculation of the maximum density of carriers (N_{max}) excited by a single pulse is described in App. A. We assume that both the pump power

and focus spot area $A \approx 25\ \mu m^2$ are constant throughout the measurements, at each excitation wavelength.

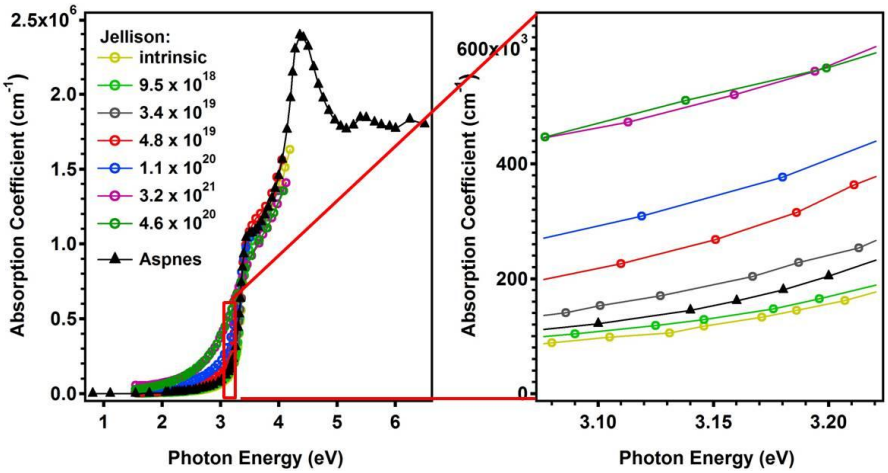

Figure 66: Absorption coefficient of Si vs. wavelength [85, 153, 154] with expanded view of the absorption coefficient change for the wavelength range used in this experiment.

The reflectivity coefficient is estimated from the Fresnel equation at normal incidence, $R=\left((1-n)^2+k^2\right)/\left((1+n)^2+k^2\right)$, where the values for the index of refraction ***n*** and the extinction coefficient ***k*** are taken from Aspnes [153]. The calculated photoexcited carrier densities (integrated over the measurement volume) vs. wavelength, for 21 mW and 34 mW pump powers, are presented in Fig. 67.

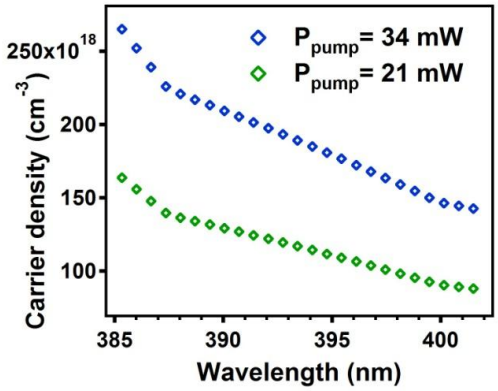

Figure 67: Estimated carrier density vs. wavelength based on absorption coefficients from Ref [85, 153].

In Fig. 65a the LO phonon frequency is plotted vs. estimated carrier density, together with the Raman values obtained by Cerdeira [28] for variously doped Si samples. Our data show consistency with the carrier density dependent Raman values of Ref. [28]. Although the shift of the LO phonon frequency we obtained changes as well by a factor of ~2 between measurements performed for the highest and the lowest wavelengths, the rate of its change is not consistent with the decrease of Raman frequency measured for either n- or p-doped Si, probably because in our case the shift has simultaneous contributions from both electrons and holes, as well as the lattice contraction discussed in Sections 2.6 and 4.2.2. Therefore the frequency shift reported in Table 3 is consistent with the increased photoinduced carrier density at shorter excitation wavelengths. We also expect that Γ should also reflect similar carrier density dependence for different wavelengths, but that is not the case. We clearly see in Fig. 65a that Γ decreases with increasing wavelength. This is unexpected because the carrier density decreases with increasing wavelength, and therefore the electron-phonon contribution to the LO phonon dephasing should also decrease. The origin of this unexpected behavior is not understood.

4.4.3.2 LO phonon amplitude vs. excitation wavelength

The LO phonon amplitude shows roughly a linear decrease when the pump wavelength increases (Fig. 68). The photoexcited carrier density in this experiment varies inversely with the wavelength (Fig. 67), and so does the LO phonon amplitude. The amplitude of phonons is given by the strength and orientation of the driving force, and in our case is a combination of the amplitudes of the phonons generated through each participating mechanism, as it will be explained next. DECP generates oscillations with amplitude proportional to the photoexcited carrier density. The amplitude of phonons generated by ISRS is proportional to the Raman tensor

and the intensity of the light, being given by the driving force $F(t) = \mu \frac{1}{2} N \frac{\partial \alpha}{\partial Q}\Big|_0 : \vec{E}\vec{E}$. In this expression *N* is the density of oscillators and μ is the effective (reduced) lattice mass [155, 156]. The amplitude of phonons impulsively generated is also linear with the photoexcited carrier density because the magnitude of the ISRS driving force is proportional to the pump power. Both forces act to excite phonons in the direction perpendicular to the sample, according to Raman selection rules valid for our experiment. Therefore, when both mechanisms contribute to phonon generation, the resulting vibration amplitude will be proportional to the photoexcited carrier density, and it will depend on the relative signs of the displacive and impulsive forces.

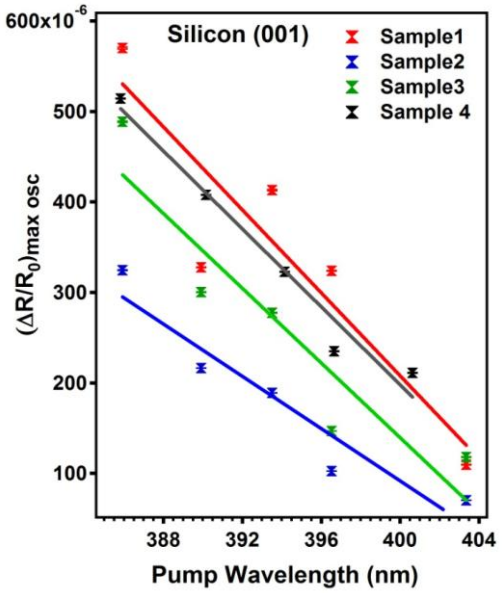

Figure 68: LO phonon amplitude vs. pump light wavelength.

The displacive force changes sign according to weather the pump polarization is parallel to [110], or to $[1\bar{1}0]$ because in each of these measurement configurations different pairs of bonds are excited [157] resulting in opposite effect on the ions (see Subsection 4.3). This effect shows as a π phase change for measurements performed in those two configurations (Subchapter 4.3, Ref. [157]). The sign of the phonon Raman tensor present in the expression of the ISRS driving

force was found to be negative for excitations below the direct band-gap of ~3.3 eV of Si [151], hence the impulsive force has to be always negative, regardless the orientation of the excitation light polarization with respect to the crystalline structure of Si.

The amplitude of the LO phonon is therefore proportional to the algebraic sum of the driving forces provided by the two competing mechanisms but it does not allow for differentiating between the magnitudes of the contributions.

4.4.3.3 LO phonon initial phase vs. excitation wavelength

An interesting result we obtain for the variation of phase with the wavelength. In Fig. 69 we present the LO phonon initial phase retrieved for sample 3 from a damped cosine fitting of the oscillatory part of the original transient reflectivity data. The theoretical results of Sabbah and Riffe [76] concerning the initial coherent LO phonon oscillation phase show the ISRS nature of LO phonon excitation for excitation energy well below (800 nm) the direct band-gap, and DECP phonon generation for above the direct band-gap (< 350 nm; red curve in Fig. 69). They have used a single point from our previous measurements [127] at 406 nm in analyzing the wavelength dependence of the coherent phonon phase (black square in Fig. 69.) Contrary to the established theories of coherent LO phonon generation (Section 2.2) and the theoretical results of Riffe et al.[76], our wavelength dependent results show very strong variation of the LO phonon phase with a trend that is contrary to the analysis of Riffe et al. Within the very narrow wavelength range we measure, the phase changes from the displacive to the impulsive limits as the excitation wavelength approaches the E_1 critical point. We should recall at this point that a chirp in the excitation pulse might induce a phase shift. The measurements presented in Fig. 30, Section 3.4.1, show a ~45° decrease in the LO phonon initial phase for a positive dispersion

change of 40 fs^2 GDD. Tilting of the BBO crystal and constant dispersion compensation conditions used in the experiment might cause our pulse to have a chirp that depends on the central wavelength. We do not believe that this is the case, however, because in addition to changing the phase, chirp causes the phonon amplitude to be substantially reduced, as seen in Fig. 30.

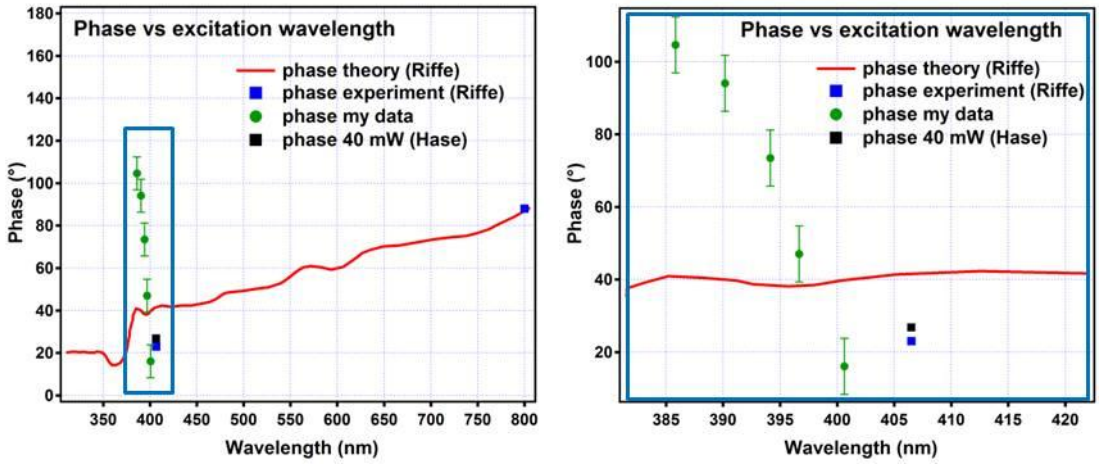

Figure 69: Initial phase of LO phonon vs. wavelength. The red line gives the theoretical calculations of Riffe et al.[76]. The green dots are experimental data obtained in this work. The blue square represents phase value retrieved by Riffe et al. from [127]. Squarse represents the phase obtained with a cosine fit of the data from [127].

We do not have a clear explanation for such an unexpected result. We suspect that the strong wavelength dependent LO phonon phase arises from the Fano resonance, which also strongly changes in the wavelength region of interest. Note that the interference embodied in the Fano lineshape is intrinsically related to the LO phonon excitation, as discussed already in Section 4.1. According to the Fano scenario, LO phonons can be excited through the excitation of LO phonon via the Raman tensor or via the excitation of carriers, which are coupled to LO phonon through the deformation potential interaction. These two excitation pathways are not independent, as supposed by theories of LO phonon excitation, but constitute two independent

pathways that interfere. Therefore, we believe that the unexpected dependence of the LO phonon phase on the excitation wavelength depends on the interference between excitation pathways, which is not yet described by theory.

4.4.4 Summary

The excitation wavelength dependent measurements show that the coherent LO phonon is strongly influenced by the generation mechanisms. The LO phonon spectra display a Fano profile with an asymmetry, i.e., carrier-phonon interaction strength, strongly dependent on the wavelength. The wavelength dependent photoexcited carrier density affects the LO phonon self-energy in the manner discussed in Subchapter 4.2. The LO phonon contribution to the change in reflectivity decreases as the wavelength increases (i.e., the photon energy decreases), and the cosine phase of the phonon decreases with increasing wavelength. The phase change departure from the established theory is a clear indication that the LO phonon generation mechanism in the diamond-type Si cannot be described merely by adding the contributions of the DECP and ISRS mechanisms. Probably both mechanisms participate in the launching of phonons simultaneously, but to describe the phase change we see one has to consider the coupling between these two excitation pathways.

5.0 CARRIER DIFFUSION

In this section we describe numerical calculation performed in order to estimate the optically injected carrier density, carrier diffusion, carrier temperature, and lattice temperature changes in the probed volume of the sample after excitation. The results are expressed as functions of the time delay between the pump and the probe pulses and are used to explain in part the nonlinear time delay dependences of the real and imaginary parts of the LO phonon self-energy in Section 4.2. Recall that the LO phonon self-energy depends on the free carrier density and distribution present in the volume of the material from which the probe beam reflects, and also on the lattice temperature increase while hot carriers lose their excess energy. As detailed Chapter 2, when coherent light is incident on a semiconductor material, high density carrier populations with temperatures much higher than the lattice temperature are excited. Those carriers are subjected concomitantly with many-body interactions, diffusion and recombination. The main electron-hole pair recombination channel in semiconductors on ultrafast time scales and high carrier densities is Auger recombination, other recombination processes having much larger time constants (see Section 2.1.4). Auger recombination constant saturates at a minimum value of 6 ps for carrier densities higher than 2×10^{20} cm^{-3} [38], rendering the carrier recombination minimal during our measurement. For native oxide covered Si the surface recombination and the effects of the band bending can be neglected, as has been shown by the experiments of Li et al. [46], which concluded that the diffusivity measurements results overlap for bulk and surface

measurements and therefore the surface recombination is negligible. The main near-surface carrier depopulation mechanism is diffusion. This may not be the case for chemically modified surfaces, such as H terminated surfaces used by Sabbah et al [41].

The electron-hole pairs created by a pulse in a material are distributed into the bulk according to the penetration depth and time profile of the pulse. A gradient of carrier concentration forms between the highly excited near-surface region and the bulk; upon excitation the carriers start diffusing toward the lower carrier density regions. At carrier densities below those required for screening of the Coulomb interactions between electrons and holes (<~$5x10^{20}$ cm^{-3}) [158], the electron and hole transport is correlated by their mutual attraction. The diffusion is therefore described by an ambipolar diffusion coefficient $D_a = \frac{2 D_e D_h}{D_e + D_h}$, where the diffusion coefficients of both type of carriers (D_e and D_h) are given by the Einstein relation, $D = \frac{\mu k_B}{e} T$, in which μ is the mobility of carriers, e the elementary charge, k_B the Boltzmann constant, and T the absolute temperature. During ambipolar diffusion electrons are slowed down by the less mobile holes. The diffusing carriers create the photo-Dember current in Eq. 4.2. Being important for a range of topics such as transport phenomena, surface photochemistry, etc., the ambipolar diffusion coefficient was subject to many studies [46, 159-161]. Ambipolar diffusion strongly depends on the carrier density under the conditions of the measurements [46, 162]: at low densities (<10^{-15} cm^{-3}), carrier-carrier scattering was shown to decrease the mobility of carriers with increasing carrier density, which implies that diffusivity. At high densities (>10^{-19} cm^{-3}), the band gap narrowing induces also a decrease in the carrier diffusivity [159, 163]; this effect is more pronounced in regions with higher free carrier concentration and slows down the diffusion by inducing carrier confinement, i.e. the carriers tend to remain in the regions with smaller band

gap energy. Moreover, the surface carrier recombination will reduce the mobility, and thus, the diffusivity in the near–surface region. The ambipolar diffusion was found to lower the rate of carrier cooling at high photoexcited carrier densities [164].

Fig. 70 contains a summary of the ambipolar diffusion coefficient of Si vs. carrier density from both theory [159] and experiment [46, 161]. Both calculations and experimental data show similar dependencies of the diffusivity on free carrier density; the calculations of Young and van Driel were done for both Boltzmann theory in which the elementary excitations are considered independent and also including many-body interactions such as band-gap renormalization due to cariers [159]. For intrinsic Si, the ambipolar diffusion coefficient was found to be about 15-20 cm^2/s [161]. In doped Si the diffusivity is constant up to doping amounts of 10^{15} cm^{-3} , after which gently decreases towards a minimum at ~10^{19} cm^{-3} , from which it accelerates steeply for higher carrier densities [159, 165].

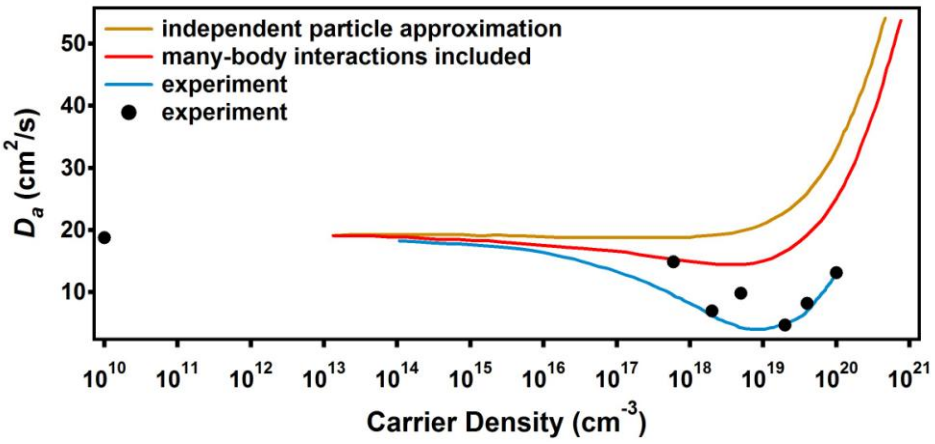

Figure 70: Literature values of the ambipolar diffusion coefficient of Si; theoretical calculations(red, orange) by Young [159], experimental (blue) by Sjodin [158], summary (black filled circles) from Li [46].

5.1 DIFFUSION EQUATION

The carrier generation occurs essentially instantaneously within an ultrashort laser pulse. Neglecting the generation source term and neglecting surface recombination [46], the simpler description of the carrier density N evolution after excitation is given by the inhomogeneous equation:

$$\frac{dN(x,y,z;t)}{dt} = -\frac{N}{\tau} - BN^2 - \gamma N^3 + D_a \nabla^2 N \,, \qquad \text{Eq. 5.1}$$

where τ is the band-edge carrier lifetime, B the radiative recombination coefficient, γ the Auger recombination coefficient and D_a the ambipolar diffusion coefficient. Eq. 5.1 is derived from Boltzmann Equation for carrier transport in semiconductors. In the case of photoexcitation, the number of carrier pairs is equal to either the number of holes or the electrons, $N = N_e = N_h$, because production and annihilation of carriers occurs in pairs.

In our experiments, the excitation is produced in a probing volume defined by the focusing spot of the pulse and the absorbing layer of the material (see Section 3.4, Fig. 28). The spot lateral dimension is much larger than the thickness of the absorbing layer and therefore the radial diffusion of carriers can be neglected. The diffusion process is simply reduced to a 1-D problem, with the space dimension given by the normal to the surface.

In this work, we modeled the carrier density in three different ways: we started with the simplest model of one partial differential equation (PDE) describing the diffusion of carrier density into the bulk (model 1), than improved the model including a second PDE to describe the lattice temperature diffusion into the bulk (model 2), and ended up using a two temperature model in which we considered the carrier density, lattice temperature and carrier temperature, as well as the propagation of the light pulse into the bulk (2-T model).

With model 1 we calculated the carrier density *N* as a function of time and bulk depth *z* evaluating numerically the partial differential equation described by Eq. 5.1 with the initial condition $N(z) = N_0(t)\exp(-\alpha z)$, where α is the absorption coefficient, and parameters τ = 50 ns, $B = 1.1\times10^{-14}\text{cm}^3/\text{s}$, $\gamma = 3.8\times10^{-31}$ cm^6/s, $\alpha = 8\times10^4$, and both a constant ambipolar diffusion $D_a = 4.7 \div 10$ cm^2/s, [46], and the carrier dependent ambipolar diffusion coefficient from Ref. [160]:

$$\frac{1}{D_a(N)} = \frac{1}{D_0} + \frac{N}{A}\ln\left(1+\left(\frac{B}{N}\right)^{\frac{2}{3}}\right), \qquad \text{Eq. 5.2}$$

A typical example of the numerical calculations with model 1 is presented in Fig. 71; for this particular case we used the carrier dependent diffusion coefficient described by Eq. 5.2 and the parameters of Ref. [46].

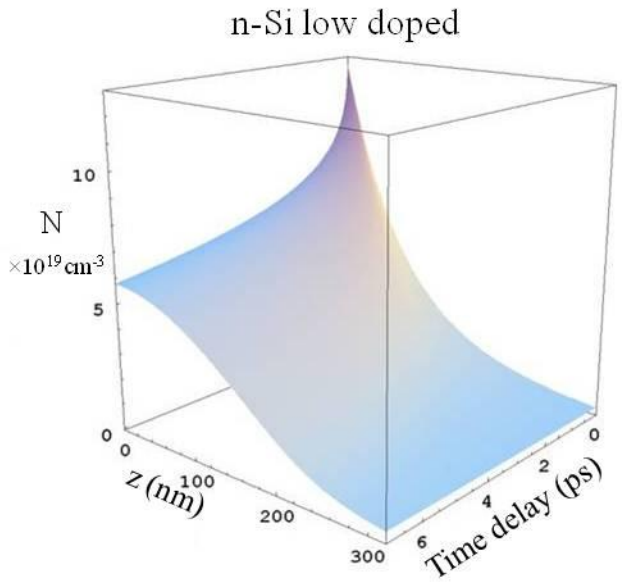

Figure 71: Carrier density vs. time delay and depth (model 1, pump fluence of 2.8 mJ*cm^{-2}).

The above model, however, does not capture the effect of heating of the lattice on charge transport, which we found to influence the LO phonon self-energy we measure in Section 4.2. In

order to refine our model we further solved a system of two coupled partial differential equations that describe the diffusion of carriers and the heat transfer to the lattice. The initial conditions were based on the assumption of a carrier density profile exponentially decaying into the bulk at time zero and no diffusion of carriers out of the surface. The calculated lattice temperature had a maximum at time zero and a quasi-exponential decay at later times, which was in disagreement with both the experimental results previously reported by, for example, Harb et al. [166], and the theoretical and experimental work of, for example, van Driel et al. [30], which found that the lattice temperature builds up on a ps scale with the rate of the temperature increasing as the duration of the excitation pulses decreases [167]. Based on the results we obtained, the first two models did not work in our case because, although for less demanding measurements in terms of time resolution or amplitude of the signal they are suitable both for metals and semiconductors excited with long pulses or CW light, in the case of ultrashort pulses the transfer of the energy from the pulse to the lattice is mediated by carrier excitation, which takes place almost instantly, with the photoexcited distributions storing most of the energy during thermalization. As soon as the carriers thermalize, thermal transfer to the lattice takes place by electron-phonon scattering while carriers undergo diffusion as well. Therefore, in order to further improve the simulation, we need to consider possible decay channels of elementary excitations through electron-phonon coupling, as well as the gradient of the temperature that forms on a ps scale between the surface and the bulk and is affecting the carrier diffusion. The partial differential diffusion equations for the carrier density and lattice heat-transfer were coupled therefore with equations describing the carrier temperature evolution and the attenuation of pump light pulse into the bulk, model known as the two temperature model [167, 168]. We used a system of PDEs based on the equations used by Korfiatis et al.[168]. This model considers the diffusion of free carriers (Eq. 5.3), the heat

conduction through the lattice (Eq. 5.4), the diffusion and relaxation of kinetic energy carried by the carriers (Eq. 5.5) and also the attenuation of the light pulse intensity into the bulk (Eq. 5.6). The equations for this model are:

$$\frac{\partial N(z,t)}{\partial t} = \frac{\partial}{\partial z}\left[D_a(N(z,t)) \frac{\partial N(z,t)}{\partial z} \right] + \frac{\alpha\, I(z,t)}{E_{photon}} - \frac{N(z,t)}{\tau_R}, \qquad \text{Eq. 5.3}$$

$$\rho C_L \frac{\partial T_L(z,t)}{\partial t} = \frac{\partial}{\partial z}\left[K_L \frac{\partial T_L(z,t)}{\partial z} \right] + \frac{3k_B\, N(z,t)\, \rho C_L}{3k_B\, N(z,t) + \rho C_L} \frac{\left(T_C(z,t) - T_L(z,t)\right)}{\tau_E}, \qquad \text{Eq. 5.4}$$

$$\frac{\partial U_C(z,t)}{\partial t} = \frac{\partial}{\partial z}\left[\frac{U_C(z,t)}{N(z,t)} D_a \frac{\partial N(z,t)}{\partial z} \right] + \frac{\left(E_{photon} - E_g\right)}{E_{photon}} \alpha\, I(z,t) -$$

$$- \frac{3k_B\, N(z,t)\, \rho C_L}{3k_B\, N(z,t) + \rho C_L} \frac{\left(T_C(z,t) - T_L(z,t)\right)}{\tau_E}, \qquad \text{Eq. 5.5}$$

$$\frac{\partial I(z,t)}{\partial z} = -\alpha\, I(z,t), \qquad I(t) = I_0 \exp\left(-\left(\frac{t}{\tau_{pulse}} \right)^2 \right). \qquad \text{Eq. 5.6}$$

In the system of equations above, the carrier energy is described by $U_C(z,t) = 3k_B\, N(z,t) T_C(z,t)$; D_a is the ambipolar diffusion coefficient, $\tau_R = \tau_R(N(z,t))$ the bulk Auger recombination decay time, ρ the density of Si, C_L the lattice specific heat, K_L=$K_L(T_L)$ the lattice thermal conductivity, $\tau_E = \tau_E(N(z,t))$ is the energy relaxation time, E_{photon} the pulse photon energy, and we take the band gap energy to be a function of carrier density and lattice temperature, $E_g = f(N, T_L)$. The Gaussian pulse intensity, $I(z,t)$, is absorbed in the bulk due to one-photon absorption, where α is the linear absorption coefficient; τ_{pulse} in Eq. 5.6 is the pulse duration. The right side of Eq. 5.3 contains, in order, the carrier diffusion, the 1-photon absorption and the bulk recombination terms. The right side terms in Eq. 5.4 are the lattice temperature diffusion and the carrier-lattice transfer of energy terms. In Eq. 5.5 the first term

describes the diffusion of carrier temperature into the bulk and the second, the photoexcited carrier energy above the band gap. The boundary conditions chosen specify that inside the bulk the carrier density decays to zero at a suitable depth, and there are no carriers escaping outside the sample surface,

$$N\big|_{z=\infty} = 0, \left.\frac{\partial N}{\partial z}\right|_{z=0} . \qquad \text{Eq. 5.7}$$

If, however, the surface recombination *S* were be considered, then the balance between surface recombination and diffusion of the electrons from the bulk towards the surface has to be accounted for, and the boundary condition on the surface becomes

$$\left(D\frac{\partial N}{\partial z} - SN \right)_{z=0} = 0 . \qquad \text{Eq. 5.8}$$

Eqs. 3-6 describe fairly well the carrier diffusion and lattice temperature increase for our particular case. In the next section the results we obtain are shown in the context of our experimental results.

5.2 COMPARISON WITH EXPERIMENTAL RESULTS

The two-temperature system of partial differential equations discussed above is numerically solved for 6 ps time delay and initial excitation from 10 to 60 mW pump power (pump fluences from 0.56 to 3.36 $mJ \cdot cm^{-2}$), using the parameters listed in Table 4; numerical results are presented in Fig. 73. The choice of ambipolar coefficient is somewhat ambiguous, because reported values for Si are quite uncertain at the carrier densities photoexcited in this work. Theoretically estimated values [159] are not in total agreement with the experimental values

reported [158-161], due to both assumptions and simplifications used in theoretical calculations and limitations of the experimental methods. Due to the extremely short laser pulse duration and high free carrier densities involved, the gradient of carriers between surface and bulk might be even steep enough to permit their diffusion right after excitation at higher diffusion coefficients than the ones reported, although the carrier-carrier scattering and band-gap narrowing was found to decrease the diffusivity at high carrier densities as well [159, 163]. We consider these possible effects [169] by extrapolating the function we constructed from the carrier dependent ambipolar coefficient measured by Sjodin et al. [158] to obtain curves with higher and lower diffusivity at high carrier density. In Fig. 72 are presented several carrier dependent ambipolar diffusion functions that were used in our calculations. The best results we obtained with $D_6(N)$, and also with $D_{Sjodin}(N)$; constant diffusivity $D_1(N)$ and carrier dependent diffusivity with values at high carrier densities that are higher than the ones of $D_{Sjodin}(N)$ or lower than of $D_3(N)$ do not model well our experimental data, overestimating the ambipolar diffusivity, as it can be seen in Fig. 74.

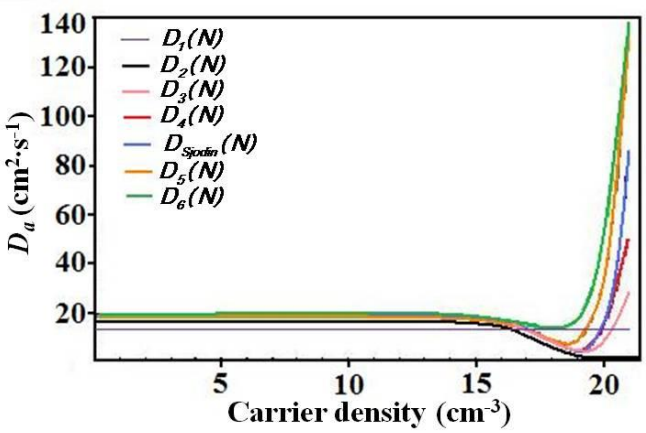

Figure 72: Ambipolar diffusion coefficients with various dependences on carrier density. Experimental values from Ref. [159] (blue), and Ref. [160] (black).

The numerical calculations return time-space profiles of the carrier density *N* (such as in Fig. 71), lattice temperature T_L, and carrier temperature T_C. The space-time profiles are integrated

over the sample volume that is probed (Fig. 28) at the instants corresponding to each data point recorded during the 6 ps scan time of the experiments. As explained in Section 3.4, the probed volume is cylindrical, with height of 35 nm and top and bottom areas of 25 μm^2. In Fig. 73 N, T_L and T_C vs. time delay calculated for the carrier dependent ambipolar diffusion measured by Sjodin et al. [158] show that the photoexcited population of carriers N in the probed volume builds up with a time integral of the pump pulse to a maximum in about 20-25 fs after excitation, and the depopulation rate increases as the intensity of the excitation increases. In 6 ps, for all the pump power values considered, the number of carriers decreases by roughly a half in comparison with the initial density. The lattice temperature T_L builds up during the first picosecond. For higher intensity, T_L reaches a maximum at later times than for lower intensity.

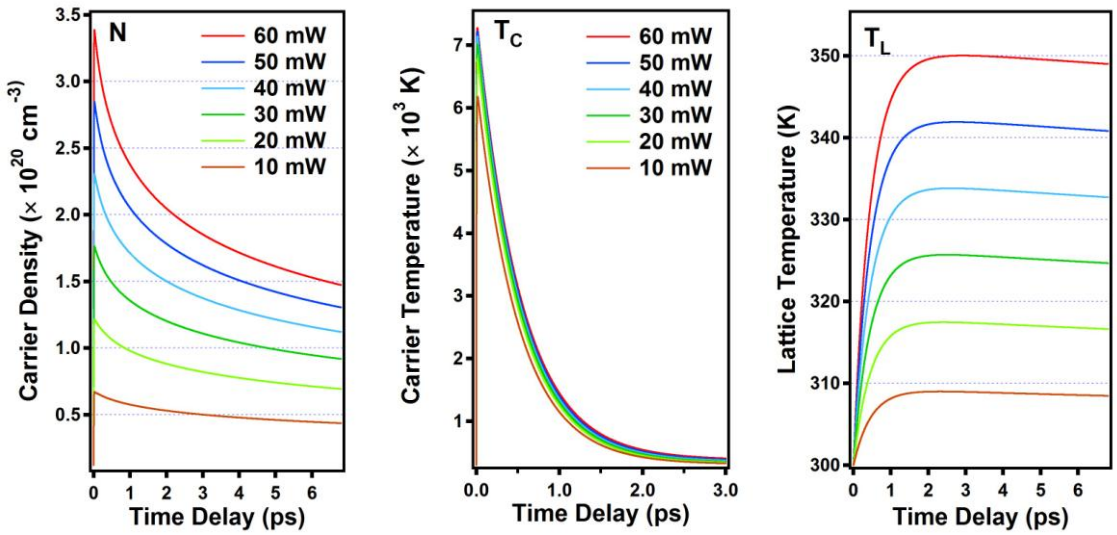

Figure 73: Calculated free carrier density N, lattice temperature T_C and carrier temperature T_L vs. time delay.

Both the carrier temperature and the lattice temperature show somewhat faster decays as the pump power increases. To verify if the calculations are producing sensible results, our experimental LO phonon dephasing rate values seem to be a better choice for comparison than the experimental coherent LO phonon frequencies, because the frequency dependence on the

time delay includes effects beyond those of simple diffusion of the carrier density and lattice temperature under corresponding gradients between surface and bulk. Recall that the dependence of dephasing rate on the free carrier density was shown to be linear with hole density, and weakly dependent on the electron concentration [28]. Also, for the range of lattice temperatures attained in our experiments as calculated with the 2-T model, the temperature dependence of the dephasing time is roughly linear manner [98, 99]. Therefore we expect the dephasing rate of coherent LO phonon to display a roughly linear change with carrier density.

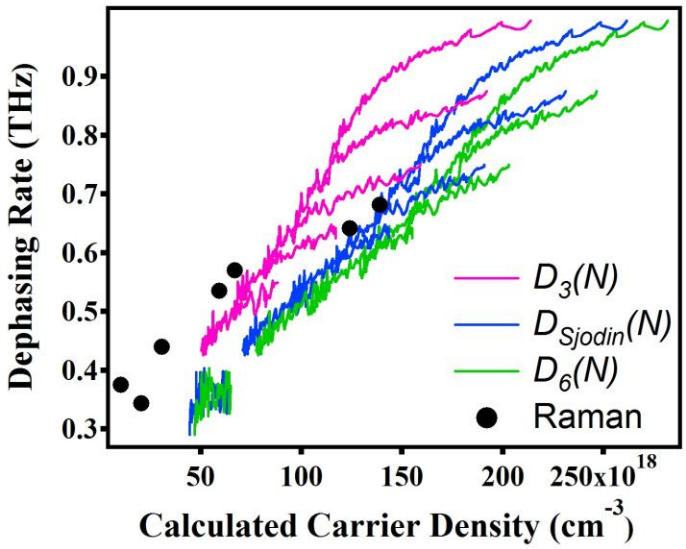

Figure 74: Coherent LO phonon dephasing rates vs. calculated carrier density (n-Si high doped) for several of the carrier dependent diffusivities presented in Fig. 72: $D_{Sjodin}(N)$ [159] (blue), $D_3(N)$ (pink), $D_6(N)$ (green). Raman dephasing times from [28] (black dots).

In Fig. 74 are presented the experimental results for coherent LO phonon dephasing time of n-Si high doped at various intensities of excitation vs. representative results for calculated carrier densities; one can clearly see how the ambipolar diffusion rate affects the calculations: the ambipolar diffusivity is overestimated by the carrier dependent diffusivity of $D_3(N)$ (pink), rendering a highly nonlinear carrier dependence of LO dephasing rate vs. carrier density shows

nonlinear dependence at all pump excitations, and yields increasing dephasing time linearity on the carrier density for decreases diffusivity at high carrier density, for which the dephasing rate show better overlapping at the same carrier densities for different measurements. At excitations of 50 and 60 mW pump powers, however, the dephasing rate vs. carrier density curves are nonlinear for all diffusivity choices we consider; this could be because of still incorrect description of ambipolar diffusion at high carrier densities, or other factors that are not included in the model. The best choice seem to be carrier density dependent $D_6(N)$, which corroborates with increased carrier mobilities for high carrier densities. For even higher diffusivity at high carrier density the calculations return again increasing nonlinear dependence of LO phonon dephasing on the carrier density.

Now let us analyze whether the calculated carrier density profiles can explain the pump fluence and pump-probe time delay dependent LO phonon frequency changes. As explained in Section 4.2, the nonlinear carrier density dependence of coherent LO phonon frequency shift is in part determined by the phonon simultaneously coupling with holes and electrons, with different contributions to the frequency change (Eq. 4.5), and in part by the electronic system k-space distribution, L-valleys electrons having a smaller and shorter contribution than X-valleys electrons (Fig. 53). In Fig. 75 the LO phonon frequency vs. calculated carrier density curves for the three choices of diffusivity we chose to exemplify the calculations with the two temperature (2-T) model (Fig. 7.2, Fig. 7.4) show clearly the nonlinear carrier dependent LO phonon frequency for different excitation intensity diverging for decreasing carrier densities, i.e., later delay times. This nonlinearity is not unexpected, but the divergence is, because if one considers only the carrier density and k-space distribution dependence of the LO phonon frequency, one expects the frequency to converge toward the 15.6 THz Raman value of nonexcited Si at rates

shown by the carrier density calculations (Fig. 73), i.e., the LO phonon frequency at later times should be red-shifted still for all the pump fluencies used (carrier density decays roughly twice during the 6 ps scan for all the pump fluencies used). Certainly, the frequencies should not exceed the LO phonon Raman frequency of 15.6 THz for the unexcited system, as they clearly do. Also, we do expect the frequencies pertaining to measurements for different pumps to have the same values at the same carrier density, which clearly does not happen.

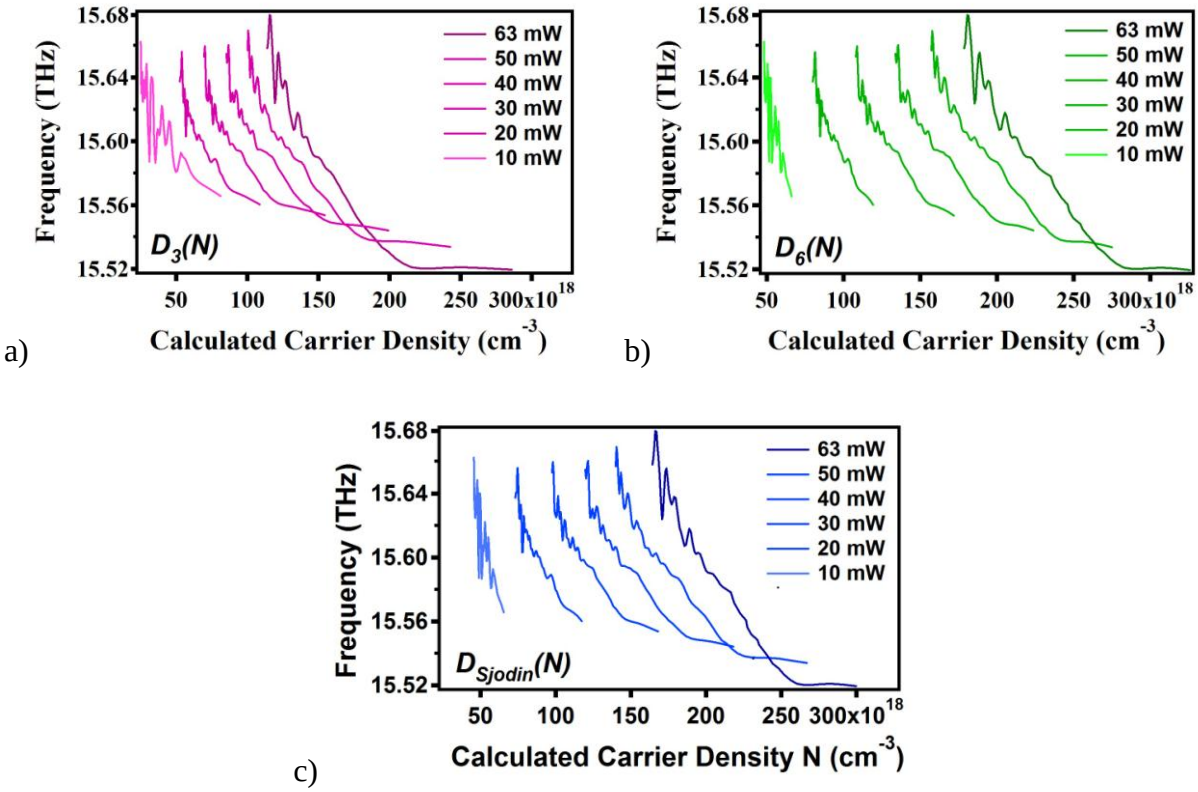

Figure 75: Coherent LO phonon frequency vs. calculated carrier density, for various choices of ambipolar diffusivity (n-Si high doped); a) $D_3(N)$**; b)** $D_{Sjodin}(N)$ **[159]; c)** $D_6(N)$**.**

For all a), b) and c) choices of diffusivity shown in Fig, 72, the frequency exceeds the Raman value of 15.6 THz towards lower carrier density for all pump powers. However, the trend for the frequency shift associated with L-valley carriers (first 500 fs, see Section 4.2.2, Fig. 53) seems to follow consistently the Raman measurements of Cerdeira and Cardona [28]. The LO phonon

frequency deviation from the expected behavior was explained in Section 4.2 by a contraction of the lattice after the L- to X-valley electronic transfer occurs which occur at the acoustic phonon velocity and it would blue-shift the LO phonon frequency, opposing the red-shifting effect of the carrier density. Because this additional effect is beyond the coupled charge-heat transport model, the experimental data cannot be reconciled with the expected evolution in the carrier density following intense pulse excitation. By visual inspection, the experimental values of ambipolar diffusion of Sjodin [159] and the $D_6(N)$ give similar results when applied to the LO phonon frequency, while the ones obtained with diffusivity $D_3(N)$ are quite different; either the extrapolated experimental results of Sjodin or $D_6(N)$ can be used for data comparison.

Summarizing, in this chapter we described a system of partial differential equations with which we numerically calculated the change in the carrier density, and carrier and lattice temperatures for Si under intense 10 fs laser excitation. The model could explain the dependence of the LO phonon dephasing rate dependence on the calculated carrier density using the literature values for ambipolar diffusion rate. The validity of the analysis was surmised by the fact that for different excitation power level measurements, the same rates were observed at the same calculated densities. The same analysis failed to explain the LO phonon frequency change as a function of carrier concentrations. We surmise that the LO phonon frequency is affected by different factors, which lead to a strong blue shift of the frequency on picosecond time scales. We believe that the lattice contraction due to the L- to X-valley electron transfer is responsible for the picosecond time scale behavior of the LO phonon frequency.

Table 4: Parameters used for numerical calculations.

Parameters	Symbol	Values	Units
Energy gap	E_g	1.124 [30, 41]	eV

		$1.16-7.02\times10^{-4}T^2/(T+1108K)-1.5\times10^{-8}N^{1/3}$ [30]	
Volume specific heat	C_v ($\rho\cdot C$)	1.64 [41]	$J\cdot cm^{-3}\cdot K^{-1}$
Mass density	ρ	2.33	$g\cdot cm^{-3}$
Carrier ambipolar diffusivity	D_a	18 [41]; 18 (300K/T) [30] For $D_a(N)$ see Fig.72	$cm^2\cdot s^{-1}$
Lattice thermal diffusivity	T	0.88	$cm^2\cdot s^{-1}$
Lattice thermal conductivity	κ_L	$1585\times T^{-1.23}$ [30]	$W\cdot cm^{-1}\cdot K^{-1}$
Real index of refraction @ 400 nm	n	5.6	
Imaginary index of refraction @ 400 nm	k	0.387	
Absorption coefficient @ 400 nm	α	8×10^4 12.158×10^4 (calculated from k and λ)	cm^{-1}
Static permittivity	ε_0	11.67	
Free electron mass	m_0	9.109×10^{-28}	g
Reflectivity coefficient	R	0.5 (doping dependent)	
Radiative recombination coefficient	B	1.1×10^{-14}[170]	$cm^3\cdot s^{-1}$
Auger recombination coefficient	γ	3.8×10^{-31} [171]	$cm^6\cdot s^{-1}$
Auger recombination time	τ_R	$\frac{1}{\gamma n^2}$, $n\le6.5\times10^{20}$ cm^{-3}; 6, $n>6.5\times10^{20}$ cm^{-3}	ps

Energy relaxation time	τ_E	$\tau_E = \tau_{E0}\left[1+\left(\frac{n}{n_c}\right)^2\right]$, $n_c = 2\times10^{21}$ cm^{-3}; $\tau_{E0} = 0.5$	ps
Band edge carrier lifetime (bulk recombination time)	τ	50 [170]	ns

6.0 SUMMARY

In this thesis we studied the coupling between photoexcited high carrier densities and coherent longitudinal-optical (LO) zone-center (k=0) phonons of Si(001). In section 4.1 we have followed in an ultrafast regime the formation of a "quasiparticle" through the "dressing" of the LO phonon with elementary particles [127], by analyzing the time-frequency maps (CWT) of the transient reflectivity signals measured by electro-optic sampling [127, 133]. The fs resolution of the technique we use enables one to follow in real time the carrier photoexcitation, almost simultaneous LO phonon generation, and their interaction through the deformation potential mechanism, revealing the time evolution of the quasiparticle formed by their interaction. Intra- and inter-band transitions identified on the CWTs before the onset of the coherent LO phonon in the $\Gamma_{25'}$ symmetry and in a similar time scale the electronic response in the Γ_{12} symmetry, contribute to the nonlinear susceptibilities of second- and third-order, $\chi^{(2)}$, respectively $\chi^{(3)}$ which play multiple roles, coupling the pump and the probe fields, modulating the reflectivity of the material and in the same time generating the coherent LO phonon driving force. The transitions involved in the light coupling with matter are near-resonant with the ~3.3 eV band gap of Si for the excitation light of ~3.1 eV of our measurement, and can be both real and virtual. The onset of the "quasiparticle" is marked by destructive interference with the continuum of free electronic states which is revealed as a dip in the time-frequency domain in $\Gamma_{25'}$ symmetry, while in Γ_{12} symmetry the coherent phonons cannot be launched because of the simultaneous excitation

of all four of the tetragonal bonds of Si [8, 67]. The formation of quasiparticle can be distinguished clearly by the correction to the bare LO phonon frequency, which is proportional to the real part of its QM self-energy, at the very moment when the discrete LO phonon state interferes destructively with the continua provided by carrier inter- and intra-band transitions in both valence and conduction bands [28, 124, 138, 139]. The deformation potential interaction acts both ways, coupling the LO phonon discrete state with the continuum of carriers through distortions of the lattice produced by the phonon, which in turn produces intra-and inter-valleys redistribution of carriers, thus lowering the total free energy of the system and forcing the phonons to compensate by gaining the self-energy [28, 124].

The complex self-energy that the LO phonon gains when "dressed" by elementary excitation was studied as a function of time delay between the pump and probe pulses for ~6 ps after excitation (Section 4.2). There are multiple contributions to the LO phonon self-energy change, such as photoexcited carrier density, lattice temperature, and acoustic phonons produced by photostriction while the sample is illuminated. Also both the direct and indirect band gaps of Si are lowered by injected carrier density and lattice temperature increase and the dynamical pressure created by the phonon vibration [22, 28, 34, 172], affecting the carrirs nobilities. Their total contribution to the coherent LO phonon renormalization and their different time scales of onset is revealed by the complicated dependence of LO phonon frequency, respectively quasi-linear dependence of the LO phonon dephasing rate on time delay. There is not a straightforward way to separate these contributions to transient reflectivity measurements, but their effect indicates that the transfer of energy from hot carriers to the lattice is strongly dependent on the carrier density and the dimension of the probed volume of the sample.

One of the topics still under debate is the generation mechanism of the LO phonon of Si. The accepted mechanisms for the coherent phonon generation [67, 74, 173, 174] are the displacive excitation of coherent phonon (DECP) and impulsive stimulated Raman scattering (ISRS). For the photon of ~3.1 eV energy in our experiment, the transitions excited are near-resonant with the ~3.3 eV direct band gap of Si. The ISRS involves virtual transitions and a phonon driving force $F(t) \propto \delta(t)$, and DECP involves real transitions, and a step function-like driving force. The pump and probe polarization angular dependence of the transient reflectivity with respect to the [110] crystalline lattice of Si (Section 4.3) do not allow to separate the ISRS and DECP contributions because they are expected to be described by Raman tensors of the same symmetry. The polarization results exclude any isotropic mechanism that could contribute to the phonon generation. The main method to distinguish between these two excitation mechanisms is to account for the initial phase of the oscillation, which in Si(001) was found by Hase et al. to be ~23° [127] at excitation with 405 nm pump pulse. In the present work we have shown the phase to vary substantially within the small range of wavelengths of 386-403 nm (Section 4.4) in a manner that cannot be explained as transition from ISRS to DECP mechanism that was proposed by Riffe and Sabbah. We attribute this difference to the fact that the LO phonon generation is affected by final state interactions involving electron-phonon coupling via the deformation potential. The final state interaction signifies that the DECP and ISRS mechanisms are not independent but rather are coupled, as evidenced by wavelength dependent Fano line shapes. To further study this topic, the theory of coherent phonon generation needs to be refined and wavelength dependent measurements over a broader range near the E_1 critical point need to be performed.

The studies performed here provide a detailed picture of the coupling of electron and lattice degrees of freedom in Si form the perspective of coherent LO phonons. The detailed understanding obtained in these measurements should complement other techniques such as ultrafast electron and x-ray diffraction, which are currently being used to study the sub-picosecond response of materials under extreme excitation conditions.

All of the interactions between LO phonon and free carrier distributions analyzed in this thesis are shown to affect the optical and electrical properties of Si, which greatly influence the performances of electronic and optoelectronic devices [1-6].

APPENDIX A

ESTIMATION OF THE PHOTOEXCITED CARRIER DENSITY FROM PUMP FLUENCE

To calculate the carrier density excited by the light pulse we follow the steps summarized below:

- Measure the area A of spot size on the sample.
- Evaluate energy per pulse: $E_{pulse} = \frac{P}{repetition\ \ rate}$, where P is the pulse power (W) and repetition rate of the laser pulse (Hz);
- Evaluate the fluence $F = \frac{E_{pulse}}{A}$;
- Evaluate the photon energy $E_{photon} = \frac{h\,c}{\lambda}$;
- Evaluate number of carrier pairs that can be generated by the pulse per area *A:* $\frac{N}{A} = \frac{F}{E_{photon}}$.
- Evaluate the number of carriers generated by the absorbed part of the pulse in the sample (photoexcited carrier density G, assuming 1-photon absorption; quantum

efficiency is unity in this case) $N_{\max} = G = \frac{F}{E_{photon}} \times \alpha \times (1-R)$; α is the absorption coefficient and R is the reflectivity coefficient.

Assuming that electron-hole pair production is dominated by 1-photon absorption and following the procedure described, we proceed now to estimate, as an example, the total carrier density excited by the pump pulse inside the Si bulk (n-type, high doping), N_0, and the carrier density inside the volume probed by the probe pulse, $N_{V,pump}$. The maximum pump fluence is calculated for all the pump powers used in these experiments using an absorption coefficient of 8×10^4 cm^{-1} [85] (see Fig. 76a). The coefficient of reflection was estimated for all samples (Table 2) by measuring the reflected powers corresponding to all incident pump powers (Fig. 76b) and evaluating the slopes of the reflected vs. incident power curves. The coefficient of reflection of n-Si high doped was measured to be 0.42.

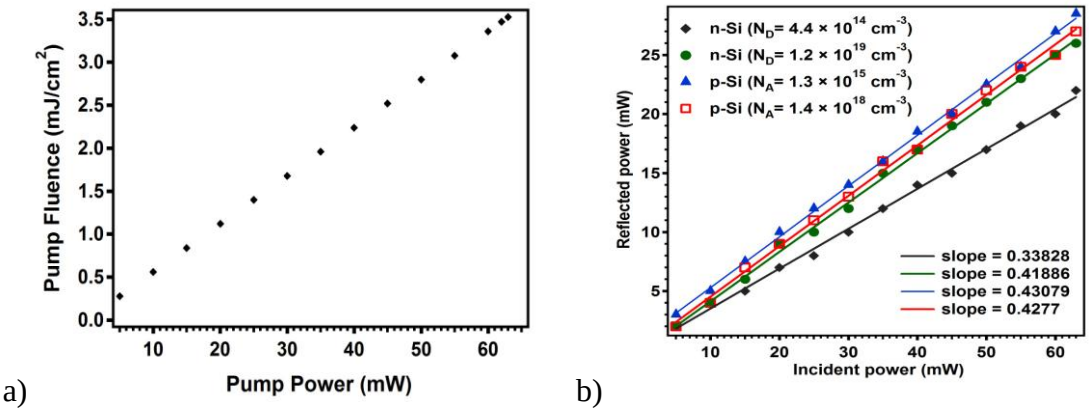

a) b)

Figure 76: a) Pump fluence vs. pump power. b) Pump fluency vs. incident pump power.

When calculating the carrier density excited in the volume of the sample we probe (Fig. 28), we need to integrate the total number of carriers N_0, that the pump pulse excites in the material, over the volume. For this we have to create first the space profile of N_0. In our case the area of

the volume is much smaller than the depth therefore we consider the profile uni-dimensional, with the dimension given by the normal z to the sample surface; therefore the carrier space profile is given by $N(z) = N_0 e^{\frac{z}{\delta}}$, where δ is the pump pulse penetration depth. The probe pulse reflects from a thin layer of thickness $d = \frac{\lambda}{2n}$, where λ is the wavelength of the incident light and n the index of refraction of the material, therefore we integrate the carrier profile $N(z)$ over this thickness to obtain $N_{V,pump}$. The reflection layer thickness and the penetration depth of Si at 400 nm are specified in Section 3.4.

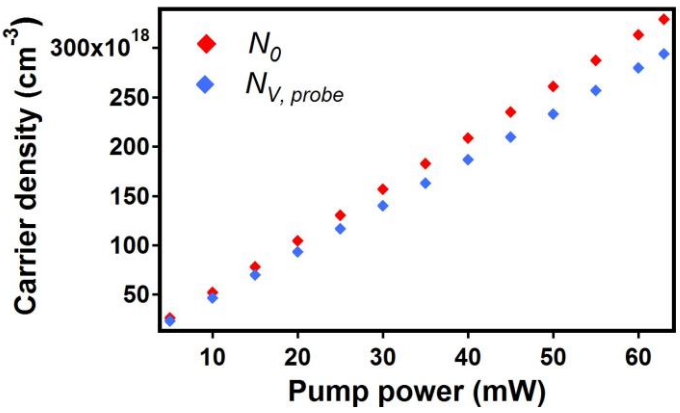

Figure 77: Calculated carrier density excited in bulk, N_0, and probed by probe pulse, $N_{V,pump}$ (n-Si, high doped).

APPENDIX B

LASER USAGE

Our Ti:Sapphire laser has a cooling system hooked at a pump that is outside the room, and function continuously. If the laser is not used for extended periods of time, probably it would be best to shut off the cooling system during this time. If the laser is used on a regular basis, the cooling system should be checked regularly to monitor any change. The Ti:Sapphire crystal heats up when pumped with high-intensity 532 nm light causing a thermal lens, which can change the alignment inside the cavity. Therefore slight realignment is necessary almost before each use.

The steps we follow each time we use the laser are:

1. Check the tower (TW) temperature on the control box. It should be about 19-20°C. Also check if the Ti:Sapphire output beam is blocked.
2. Start the pump laser using the control box power button.
3. Let the system to stabilize for about 10-15 minutes.
4. Tap the left pump mirror support to induce mode-locking.
5. Let another 10-15 minutes to stabilize.

6. Measure the power and adjust the end mirror and the output coupler of the Ti:Sapphire cavity (Fig. 3.1) for maximum power.

7. Unblock the Ti:Sapphire output beam and proceed to use the laser.

8. After finishing the experiments block the output beam of the cavity and shut off the pump-diode from the control box.

If the output power is less than expected (0.75-0.8 W) proceed to align the cavity as explained in Section 3.1. The mirrors should be cleaned once in a while using special tissues and optical grade methanol. Clean with great care and gentleness so the mirrors would not be pushed or scratched; be careful to touch only the crystal if possible, avoiding brushing the tissue against the metal mount, which can have hard particles on it. Never reuse lens tissue. Once each month or rarer mirror cleaning is fine if the cavity is encased into a shielding box. Block the diode-pump beam and clean one mirror at a time, after which realign the mirror, if necessary. The Ti:Sapphire crystal should be cleaned as well, the same way as the mirrors and using the same tools, but with even greater care.

APPENDIX C

DEFORMATION POTENTIALS OF SILICON

In semiconductors, a strain applied along crystallographic directions changes the energy of the electronic band structure and affects the mobility of free carriers. Depending on the direction of application and the nature of the strain or, the energy of the band is changed (hydrostatic strain) or/and its degeneracy is lifted (uniaxial strain). The amount by which the band energy changes is proportional to quantities called deformation potential constants. This effect is explained by the deformation potential theory, which states that strain changes the degeneracy of some valleys, depending on the symmetry, inducing a redistribution of the carriers between the various subvalleys and therefore causing a modification of the carrier's mobility by affecting their effective masses (note: effective mass is proportional to the energy band curvature in k-space) [175]. The deformation potential theory was developed by Bardeen and Shockley [176] in order to relate carrier mobility to the shifts of electronic bands associated with dilations due to acoustical vibrations.

The stress applied to a cubic semiconductor also affects the zone-center ($q = 0$) optical phonons as well [56, 101], splitting or/and shifting them by amounts which depend on the deformation potential constants.

In this section we present a list of deformation potentials and formal expressions of the critical points energy shifts they produce when strains are applied along different symmetry axis of Si. This list is adapted from Robert Hull [177].

Si is elastic over a certain range of deformation. For an elastic solid the stress tensor is related to the strain tensor through the linear relationship $\sigma_{ij} = c_{ijkl}\varepsilon_{kl}$, where c_{ijkl} is a tensor containing the elastic stiffness constants. Due to its cubic symmetry, the fourth rank elastic constants tensor of Si has the form of

$$c_{ijkl} = \begin{bmatrix} C_{11} & C_{12} & C_{12} & 0 & 0 & 0 \\ C_{12} & C_{11} & C_{12} & 0 & 0 & 0 \\ C_{12} & C_{12} & C_{11} & 0 & 0 & 0 \\ 0 & 0 & 0 & C_{44} & 0 & 0 \\ 0 & 0 & 0 & 0 & C_{44} & 0 \\ 0 & 0 & 0 & 0 & 0 & C_{44} \end{bmatrix},$$

where the elastic constants are defined in Table 5.

Note that the elastic constants are temperature dependent, but their change is small for Si, i.e., $C_{11} = \frac{-75\times10^{-6}}{T(K)}$ [178].

Table 5: Elastic stiffness constants and compliances of Si.

Elastic constant	Experimental value
C_{11}	1.657×10^{12} dyn/cm^2 [179]; 1.601×10^{12} dyn/cm^2 [180]
C_{12}	0.639×10^{12} dyn/cm^2 [179]; 0.578×10^{12} dyn/cm^2 [180]
C_{44}	0.7956×10^{12} dyn/cm^2 [179] ; 0.8×10^{12} dyn/cm^2 [180]
S_{11}	7.48×10^{-7} cm^2/kg[181]
S_{12}	-2.1×10^{-7} cm^2/kg[181]
S_{44}	12.22×10^{-7} cm^2/kg[181]

The strain tensors for strain applied in [001], [111] and [110] directions are given by

$$\varepsilon_{[001]} = \begin{pmatrix} \varepsilon_{xx} & 0 & 0 \\ 0 & \varepsilon_{xx} & 0 \\ 0 & 0 & \varepsilon_{zz} \end{pmatrix};\ \varepsilon_{[111]} = \begin{pmatrix} \varepsilon_{xx} & \varepsilon_{xy} & \varepsilon_{xy} \\ \varepsilon_{xy} & \varepsilon_{xx} & \varepsilon_{xy} \\ \varepsilon_{xy} & \varepsilon_{xy} & \varepsilon_{xx} \end{pmatrix};\ \varepsilon_{[110]} = \begin{pmatrix} \varepsilon_{xx} & \varepsilon_{xy} & 0 \\ \varepsilon_{xy} & \varepsilon_{xx} & 0 \\ 0 & 0 & \varepsilon_{zz} \end{pmatrix}.$$

For uniaxial stress, the strain matrix elements depend on the direction and magnitude of the applied pressure X, with the proportionality constant given by the compliances [177]:

pressure along [001]: $\varepsilon_{xx} = S_{12}X$ and $\varepsilon_{zz} = S_{11}X$;

pressure along [111]: $\varepsilon_{xx} = \frac{1}{3}(S_{11} + 2S_{12})X$ and $\varepsilon_{xy} = \frac{1}{6}S_{44}X$;

pressure along [110]: $\varepsilon_{xx} = \frac{1}{2}(S_{11} + 2S_{12})X$, $\varepsilon_{xy} = \frac{1}{6}S_{44}X$ and $\varepsilon_{zz} = S_{12}X$.

Compliance constants S_{ij} are given in terms of elastic stiffness constants by:

$$S_{11} = \frac{C_{11} + C_{12}}{(C_{11} - C_{12})(C_{11} + 2C_{12})};\ S_{12} = \frac{-C_{12}}{(C_{11} - C_{12})(C_{11} + 2C_{12})};\ S_{44} = \frac{1}{C_{44}}$$

The band energies change by different amounts for different bands and for different directions in which the strain is applied to the material. Note that the sign of the change depends on whether the strain compresses or dilates the lattice.

In the next part of this appendix we compiled expressions for the shifts of VBM and CBM of Si, for strain applied along the principal crystallographic directions pertinent to our work. The numerical values and the different notations used in literature for all the deformation potential constants involved in the mathematical expressions of the shifts are listed in **Error! Reference source not found.**.

.

Valence band maxima shift in the presence of strain:

The VBM of Si is triply degenerated in the absence of spin-orbit coupling and strain. In the presence of spin-orbit coupling the heavy- and light-hole states are displaced by a quantity $\Delta_0/3$ (**Error! Reference source not found.**), and the split-off state is displaced by (-2 $\Delta_0/3$), with respect to Γ point. In the presence of strain additional shifts are induced, and the total band edge shifts are:

$$\Delta E_{hh} = \delta E_h - \frac{1}{6}\Delta_0 + \frac{1}{4}\delta E + \frac{1}{2}\sqrt{\Delta_0^2 + \Delta_0(\delta E) + \frac{9}{4}(\delta E)^2}\ ,\ \Delta E_{lh} = \delta E_h + \frac{1}{3}\Delta_0 - \frac{1}{4}\delta E\ ,$$

$$\Delta E_{so} = \delta E_h - \frac{1}{6}\Delta_0 + \frac{1}{4}\delta E - \frac{1}{2}\sqrt{\Delta_0^2 + \Delta_0(\delta E) + \frac{9}{4}(\delta E)^2}\ ,$$

where $\delta E_h = a^v Tr[\varepsilon]$ is the hydrostatic component of the shift, a^v is the hydrostatic deformation potential of the VB, $\boldsymbol{\varepsilon}$ is the strain tensor, $\delta E = \begin{cases} 2b(\varepsilon_{zz} - \varepsilon_{xx}), & for\ X\ parallel\ to\ [001] \\ 2\sqrt{3}d\varepsilon_{xy}, & for\ X\ parallel\ to\ [111] \end{cases}$, and d^v and b^v are the deformation potentials for the uniaxial trigonal distortion, respectively the uniaxial tetragonal distortion of the cubic lattice.

Conduction band minima shift in the presence of strain

1) Strain along [001]

For this direction of the strain, the Δ valleys split into a doublet along z-direction and a quadruply-degenerate valleys in the x- and y-directions. The corresponding shifts have contributions from both the hydrostatic and uniaxial parts of the strain:

$$\delta E_{x,y}^{\Delta} = \left(\Xi_d^{\Delta} + \frac{1}{3}\Xi_u^{\Delta}\right)Tr[\varepsilon] - \frac{1}{3}\Xi_u^{\Delta}(\varepsilon_{zz} - \varepsilon_{xx}),\ \delta E_z^{\Delta} = \left(\Xi_d^{\Delta} + \frac{1}{3}\Xi_u^{\Delta}\right)Tr[\varepsilon] + \frac{2}{3}\Xi_u^{\Delta}(\varepsilon_{zz} - \varepsilon_{xx}).$$

The quantities $\Xi_d^{\Delta} + \frac{1}{3}\Xi_u^{\Delta}$ and Ξ_u^{Δ} represents the hydrostatic, respectively the uniaxial parts of the deformation potential constants for the CBM shift.

1) Strain along [111]

In this case only the hydrostatic part of the strain contributes. All Δ valleys shift by the same amount:

$$\delta E^{\Delta} = \left(\Xi_d^{\Delta} + \frac{1}{3}\Xi_u^{\Delta} \right) Tr[\varepsilon].$$

The total contribution of the strain to the indirect band-gap of Si is given by the deformation potential constant a_g.

Λ valley minima shift in the presence of strain

The Λ valley minima correspond to the critical points E_1 and $E_1 + \Delta_1$.

1) Strain parallel to [001] direction:

$$\delta E_{\pm} = \delta E_h + \frac{1}{2}\Delta_1 \pm \frac{1}{2}\sqrt{\Delta_1^2 + 4(\delta E_S)^2}$$

where $\delta E_h = \frac{1}{\sqrt{3}} D_1^1 Tr[\varepsilon]$; $\delta E_s = \sqrt{\frac{2}{3}} D_3^3 (\varepsilon_{zz} - \varepsilon_{xx})$.

The "+" sign corresponds to $E_1 + \Delta_1$ transition, the "–" sign corresponds to E_1 transition, Δ_1 (0.044 eV) is the spin-orbit splitting constant, D_1^1 is the deformation potential constant describing the hydrostatic shift, D_3^3 is the potential constant describing the intraband splitting of the valence band.

2) Strain parallel to [111] direction.

In this case the L-valleys are splitted into a singlet ([111]) and a triplet ($[1\bar{1}\,\bar{1}],[\bar{1}\,1\,\bar{1}],[\bar{1}\,\bar{1}\,1]$) shifted with respect to the unstrained crystal band energy by:

$$\delta E_{\pm}^{s} = \delta E_h + \frac{1}{2}\Delta_1 + \frac{\delta E_S^s}{2} \pm \frac{\Delta_1}{2} \text{ and } \delta E_{\pm}^{t} = \delta E_h + \frac{1}{2}\Delta_1 - \frac{\delta E_S^t}{6} \pm \frac{1}{6}\sqrt{9\Delta_1^2 + 16(\delta E_S^t)^2},$$

where $\delta E_S^s = 2\sqrt{3}\, D_1^5 \varepsilon_{xy}$ and $\delta E_S^t = \sqrt{6}\, D_3^5 \varepsilon_{xy}$.

Table 6: Deformation potentials of Si.

Deformation potential	Experimental values [eV]	Theoretical values [eV]
Δ_0 (spin-orbit splitting constant)	0.04 [182]	
a^v [183]	2.46 [183]	
b^v [183]	-2.2±0.1 [184]	-2.35 [185]; -2.21 [186]
d^v [183]	-4.85±0.15 [184]	-5.32 [185]; -4.04 [187]
Ξ_d^{Δ} [177]	2.1 [185]	
$\Xi_d^{\Delta} + \frac{1}{3}\Xi_u^{\Delta}$ [177], $\mathcal{E}_2^*$ [28], $\Xi_{u'}$ [141], b^c [183]	7.55 [28]	8.1-8.4 [28], 9.31 [188], 9.16 [183]
$a_g = \Xi_d^{\Delta} + (1/3)\Xi_u^{\Delta} - a^v$ [177]	1.5±0.3 [184]	1.72 [185]
Ξ_u^{Δ} [177], b^c [183]	8.6±0.4 [184], 7.25 [28]	
D_1^1	-9.8±1.3 [189]; -8±1 [24];	-8.5 [190], -9.31 [188]
D_3^3	4.7±0.5 [189]; 5±1 [24], 4.36±0.62 [188]	-2.3 [190], 4.3 [188]
D_1^5 (interband contribution)[177]	6.5±1.4 [189]; 10±2 [24], 7.83±0.55 [188]	12 [190], 7.05 [188]
D_3^5 (intraband contribution)[177]	3.0±1.7 [189]; 4±1 [24], 5.04±0.87 [188]	-6.5 [190], 6.28 [188]

APPENDIX D

TIME AXIS CALIBRATION RUTINE

This rutine was developed by Kunie Ishioka (NIMS, Tsukuba, Japan) and Albert P. Heberle, Universty of Pittsburgh, Pittsburgh, USA,

```
Macro Load()
        Silent 1;PauseUpdate
        LoadWave/H/G/D/O/L={0,5,0,0,0}
        string loadedwave=s_wavenames[0,strlen(s_wavenames)-2]
        display $loadedwave
        CurveFit/Q line $loadedwave
        $loadedwave-=W_coef[0]+W_coef[1]*x
EndMacro

macro Xcalibration(wn)
string wn
|Prompt wn, "WaveName?"
```

```
Silent 1;PauseUpdate
string wnc,wncx
variable n1,n2
variable n12
variable/G lamda=6328e-10
variable i,k
if (strlen(wn)==0)
	wn=CsrWave(a)
endif
n1=0
n2=numpnts($wn)
n12=abs(n1-n2)+1
wnc=wn+"_pix"
wncx=wn+"_pos"
Duplicate/O $wn $wnc
k=0
i=0
Do
	if ($wn[i]*$wn[i+1]<=0)
	$wnc[k]=(i+(i+1))/2
	k+=1

	endif
```

```
i+=1
while (i<=n12)
DeletePoints k, n12-k, $wnc
Duplicate/O $wnc $wncx
$wncx=(lamda*x*1e3)/2
|Display $wncx vs $wnc
endmacro
Window Layout0() : Layout
	PauseUpdate; Silent 1
	Layout/C=1/W=(5.25,41.75,506.25,465.5) Graph50(71.25,69.75,538.5,717)/O=1
EndMacro
```

BIBLIOGRAPHY

1. Dong, P., S.F. Preble, and M. Lipson, *All-optical compact silicon comb switch.* Opt. Express, 2007. **15**(15): p. 9600-9605.
2. Lee, B.G., et al., *High-Speed 2×2 Switch for Multiwavelength Silicon-Photonic Networks–On-Chip.* Lightwave Technology, Journal of, 2009. **27**(14): p. 2900-2907.
3. Foster, M.A., et al., *Nonlinear optics in photonic nanowires.* Opt. Express, 2008. **16**(2): p. 1300-1320.
4. Sciuto, A., et al., *Design, fabrication, and testing of an integrated Si-based light modulator.* J. Lightwave Technol., 2003. **21**: p. 228-235.
5. Soref, R.A., *Silicon-based optoelectronics.* Proc. IEEE, 1993. **81**: p. 1687-1706.
6. Liu, A., et al., *A high-speed silicon optical modulator based on a metal-oxide-semiconductor capacitor.* Nature, 2004. **427**(6975): p. 615-618.
7. Kuznetsov, A.V. and C.J. Stanton, *Theory of Coherent Phonon Oscillations in Semiconductors.* Physical Review Letters, 1994. **73**(24): p. 3243.
8. Cho, G.C., W. Kütt, and H. Kurz, *Subpicosecond time-resolved coherent-phonon oscillations in GaAs.* Physical Review Letters, 1990. **65**(6): p. 764.
9. Boschetto, D., et al., *Small Atomic Displacements Recorded in Bismuth by the Optical Reflectivity of Femtosecond Laser-Pulse Excitations.* Physical Review Letters, 2008. **100**(2): p. 027404.
10. Hoffmann, M.C., et al., *THz-pump/THz-probe spectroscopy of semiconductors at high field strengths [Invited]*. J. Opt. Soc. Am. B, 2009. **26**(9): p. A29-A34.
11. Frank, A.H. and P.L. Kristine. *Optical pump-terahertz probe investigation of carrier relaxation in radiation-damaged silicon-on-sapphire*. 2002: SPIE.
12. George, P.A., et al., *Ultrafast Optical-Pump Terahertz-Probe Spectroscopy of the Carrier Relaxation and Recombination Dynamics in Epitaxial Graphene.* Nano Letters, 2008. **8**(12): p. 4248-4251.
13. Yano, R., et al., *Systematic pump-probe terahertz wave emission spectroscopy of a photoconductive antenna fabricated on low-temperature grown GaAs.* Journal of Applied Physics, 2004. **96**(7): p. 3635-3638.
14. Adams, B.W., et al., *Picosecond laser-pump, x-ray probe spectroscopy of GaAs.* Review of Scientific Instruments, 2002. **73**(12): p. 4150-4156.
15. James, M.G., et al. *Ultrafast X-Ray-Pump, Laser-Probe Spectroscopy at LCLS*. in *Quantum Electronics and Laser Science Conference*: Optical Society of America.
16. Ihee, H., et al., *Direct Imaging of Transient Molecular Structures with Ultrafast Diffraction.* Science, 2001. **291**(5503): p. 458-462.

17. Sundaram, S.K. and E. Mazur, *Inducing and probing non-thermal transitions in semiconductors using femtosecond laser pulses.* Nat Mater, 2002. **1**(4): p. 217-224.
18. Stampfli, P. and K.H. Bennemann, *Time dependence of the laser-induced femtosecond lattice instability of Si and GaAs: Role of longitudinal optical distortions.* Physical Review B, 1994. **49**(11): p. 7299.
19. Renucci, J.B., R.N. Tyte, and M. Cardona, *Resonant Raman scattering in silicon.* Physical Review B, 1975. **11**(10): p. 3885.
20. Yu, P. and M. Cardona, *Fundamentals of Semiconductors*. 2005: Springer-Verlag
21. Cardona, M., *Electron-phonon interaction in tetrahedral semiconductors.* Solid State Communications, 2005. **133**(1): p. 3-18.
22. Lautenschlager, P., et al., *Temperature dependence of the dielectric function and interband critical points in silicon.* Physical Review B, 1987. **36**(9): p. 4821.
23. Chelikowsky, J.R. and M.L. Cohen, *Electronic structure of silicon.* Physical Review B, 1974. **10**(12): p. 5095.
24. Pollak, F.H. and G.W. Rubloff, *Piezo-optical Evidence for Lambda Transitions at the 3.4-eV Optical Structure of Silicon.* Physical Review Letters, 1972. **29**(12): p. 789.
25. Soref, R. and B. Bennett, *Electrooptical effects in silicon.* Quantum Electronics, IEEE Journal of, 1987. **23**(1): p. 123-129.
26. Sik, J., J. Hora, and J. Humlicek, *Optical functions of silicon at high temperatures.* Journal of Applied Physics, 1998. **84**(11): p. 6291-6298.
27. Othonos, A., *Probing ultrafast carrier and phonon dynamics in semiconductors.* Journal of Applied Physics, 1998. **83**(4): p. 1789-1830.
28. Cerdeira, F. and M. Cardona, *Effect of Carrier Concentration on the Raman Frequencies of Si and Ge.* Physical Review B, 1972. **5**(4): p. 1440-1454.
29. Baumgartner, M. and G. Abstreiter, *Interaction between electronic and phonon Raman scattering in hole space charge layers on silicon.* Surface Science, 1984. **142**(1-3): p. 357-360.
30. van Driel, H.M., *Kinetics of high-density plasmas generated in Si by 1.06- and 0.53-mum picosecond laser pulses.* Physical Review B, 1987. **35**(15): p. 8166.
31. Sabbah, A.J. and D.M. Riffe, *Femtosecond pump-probe reflectivity study of silicon carrier dynamics.* Physical Review B, 2002. **66**(16): p. 165217.
32. Meyer, J., A.Y. Elezzabi, and M.K.Y. Hughes, *Infrared absorption and momentum relaxation of free carriers in silicon generated by subpicosecond above band gap radiation.* Quantum Electronics, IEEE Journal of, 1995. **31**(4): p. 729-734.
33. Gauster, W.B. and D.H. Habing, *Electronic Volume Effect in Silicon.* Physical Review Letters, 1967. **18**(24): p. 1058.
34. Viña, L. and M. Cardona, *Effect of heavy doping on the optical properties and the band structure of silicon.* Physical Review B, 1984. **29**(12): p. 6739.
35. Yang, G.-Z. and N. Bloembergen, *Effective mass in picosecond laser-produced high-density plasma in silicon* Journal of Quantum Electronics, IEEE, 1986. **22**(1): p. 195-196.
36. Goldman, J.R. and J.A. Prybyla, *Ultrafast dynamics of laser-excited electron distributions in silicon.* Physical Review Letters, 1994. **72**(9): p. 1364.
37. Elci, A., et al., *Ultrafast transient response of solid-state plasmas. I. Germanium, theory, and experiment.* Physical Review B, 1977. **16**(1): p. 191.
38. Yoffa, E.J., *Dynamics of dense laser-induced plasmas.* Physical Review B, 1980. **21**(6): p. 2415.

39. Tanimura, K., *Ultrafast carrier dynamics on Si surfaces studied by time-resolved two-photon photoemission spectroscopy*, in *Ultrafast Surface Dynamics 6*. 2008: Kloster Banz, Germany.
40. Cerdeira, F., T.A. Fjeldly, and M. Cardona, *Effect of Free Carriers on Zone-Center Vibrational Modes in Heavily Doped p-type Si. II. Optical Modes.* Physical Review B, 1973. **8**(10): p. 4734.
41. Sabbah, A., *Ultrafast carrier and coherent phonon dynamics in crystalline silicon. Ph.D dissertation*. 2002, Utah State University.
42. Schlangenotto, H., H. Maeder, and W. Gerlach, *Temperature dependence of the radiative recombination coefficient in silicon.* physica status solidi (a), 1974. **21**(1): p. 357-367.
43. Michaelis, W. and M.H. Pilkuhn, *Radiative Recombination in Silicon p-n Junctions.* physica status solidi (b), 1969. **36**(1): p. 311-319.
44. Trupke, T., et al., *Temperature dependence of the radiative recombination coefficient of intrinsic crystalline silicon.* Journal of Applied Physics, 2003. **94**(8): p. 4930-4937.
45. Haug, A. and W. Schmid, *Recombination mechanism in heavily doped silicon.* Solid-State Electronics, 1982. **25**(7): p. 665-667.
46. Li, C.-M., T. Sjodin, and H.-L. Dai, *Photoexcited carrier diffusion near a Si(111) surface: Non-negligible consequence of carrier-carrier scattering.* Physical Review B, 1997. **56**(23): p. 15252.
47. Zhou, X.Q., et al., *Hot carrier relaxation in InP and GaAs on a subpicosecond time scale.* Solid-State Electronics, 1989. **32**(12): p. 1591-1595.
48. Yoffa, E.J., *Screening of hot-carrier relaxation in highly photoexcited semiconductors.* Physical Review B, 1981. **23**(4): p. 1909.
49. Klenner, M., C. Falter, and W. Ludwig, *Electron-phonon matrix elements and deformation potentials in silicon and germanium in the quasi-ion model.* Annalen der Physik, 1992. **504**(1): p. 24-33.
50. Lietoila, A. and J.F. Gibbons, *Computer modeling of the temperature rise and carrier concentration induced in silicon by nanosecond laser pulses.* Journal of Applied Physics, 1982. **53**(4): p. 3207-3213.
51. Snoke, D., *Essential Concepts of Solid State Physics*. 2008: Addison-Wesley.
52. Hill, W.T. and C.H. Lee, *Light-Matter interaction, Atoms and molecules in external fields and nonlinear optics*. 2007: Wiley.
53. He, G.S. and S.H. Liu, *Physics of nonlinear optics*. 1999: World Scientific.
54. Shen, Y.R., *The Principles of Nonlinear Optics*. 1984: Wiley-Interscience.
55. Bartolo, B.d. and O. Forte, *Frontiers of Optical Spectroscopy: Investigating Extreme Physical Conditions with advanced Optical Techniques*. NATO Science. Vol. 168. 2003: Kluwer Academic Publishers.
56. Anastassakis, E., et al., *Effect of static uniaxial stress on the Raman spectrum of silicon.* Solid State Communications, 1970. **8**(2): p. 133-138.
57. Tóbik, J. and E. Tosatti, *Raman tensor calculation for magnesium phthalocyanine.* Surface Science, 2006. **600**(18): p. 3995-3998.
58. Loechelt, G.H., N.G. Cave, and J. Menendez, *Polarized off-axis Raman spectroscopy: A technique for measuring stress tensors in semiconductors.* Journal of Applied Physics, 1999. **86**(11): p. 6164-6180.
59. Parker, J.H., D.W. Feldman, and M. Ashkin, *Raman Scattering by Silicon and Germanium.* Physical Review, 1967. **155**(3): p. 712.

60. Wolf, I.D., et al., *Micro-Raman study of stress distribution in local isolation structures and correlation with transmission electron microscopy.* Journal of Applied Physics, 1992. **71**(2): p. 898-906.
61. Ganesan, S., A.A. Maradudin, and J. Oitmaa, *A lattice theory of morphic effects in crystals of the diamond structure.* Annals of Physics, 1970. **56**(2): p. 556-594.
62. Weber, W.H. and R. Merlin, *Raman Scattering in Materials Science*. Materials Science. Vol. 42. 2000: Springer-Verlag.
63. Greenberger, D., K. Hentschel, and F. Weinert, *Compensium of Quantum Physics: Concepts, Experiments, History and Philosophy*. 2009: Springer-Verlag.
64. Rossi, F. and T. Kuhn, *Theory of ultrafast phenomena in photoexcited semiconductors.* Reviews of Modern Physics, 2002. **74**(3): p. 895.
65. Yan, Y.-X., E.B. Gamble, Jr., and A.N. Keith, *Impulsive stimulated scattering: General importance in femtosecond laser pulse interactions with matter, and spectroscopic applications.* The Journal of Chemical Physics, 1985. **83**(11): p. 5391-5399.
66. De Silvestri, S., et al., *Femtosecond time-resolved measurements of optic phonon dephasing by impulsive stimulated raman scattering in [alpha]-perylene crystal from 20 to 300 K.* Chemical Physics Letters, 1985. **116**(2-3): p. 146-152.
67. Kutt, W.A., W. Albrecht, and H. Kurz, *Generation of coherent phonons in condensed media.* Quantum Electronics, IEEE Journal of, 1992. **28**(10): p. 2434-2444.
68. Zeiger, H.J., et al., *Theory for displacive excitation of coherent phonons.* Physical Review B, 1992. **45**(2): p. 768.
69. Cheng, T.K., et al., *Impulsive excitation of coherent phonons observed in reflection in bismuth and antimony.* Applied Physics Letters, 1990. **57**(10): p. 1004-1006.
70. Merlin, R., *Generating coherent THz phonons with light pulses.* Solid State Communications, 1997. **102**(2-3): p. 207-220.
71. Chang, Y.-M., L. Xu, and H.W.K. Tom, *Coherent phonon spectroscopy of GaAs surfaces using time-resolved second-harmonic generation.* Chemical Physics, 2000. **251**(1-3): p. 283-308.
72. Kazutaka, G.N., et al., *Femtosecond time-resolved x-ray diffraction from optical coherent phonons in CdTe(111) crystal.* Applied Physics Letters, 2008. **93**(6): p. 061905.
73. Thomsen, C., et al., *Surface generation and detection of phonons by picosecond light pulses.* Physical Review B, 1986. **34**(6): p. 4129.
74. Garrett, G.A., et al., *Coherent THz Phonons Driven by Light Pulses and the Sb Problem: What is the Mechanism?* Physical Review Letters, 1996. **77**(17): p. 3661.
75. Stevens, T.E., J. Kuhl, and R. Merlin, *Coherent phonon generation and the two stimulated Raman tensors.* Physical Review B, 2002. **65**(14): p. 144304.
76. Riffe, D.M. and A.J. Sabbah, *Coherent excitation of the optic phonon in Si: Transiently stimulated Raman scattering with a finite-lifetime electronic excitation.* Physical Review B, 2007. **76**(8): p. 085207.
77. Dumke, W.P., *On laser annealing and lattice melting.* Physics Letters A, 1980. **78**(5-6): p. 477-480.
78. Pines, D., *Elementary excitations in Solids*. 1963: W.A. Benjamin, Inc.
79. Contreras, G., et al., *Effect of free carriers on the Raman frequency of ultraheavily doped n-Si.* Solid State Communications, 1984. **49**(4): p. 303-305.
80. Telford, M., *Stretching silicon's lifespan.* III-Vs Review, 2004. **17**(7): p. 36-39.

81. Kurz, H., *Femtosecond spectroscopy of hot carrier relaxation in bulk semiconductors.* Semiconductor Science and Technology, 1992. **7**(3B): p. B124.
82. Landsberg, P.T., et al., *A Model for Band-Gap Shrinkage in Semiconductors with Application to Silicon.* physica status solidi (b), 1985. **130**(1): p. 255-266.
83. Wagner, J. and J. A. del Alamo, *Band-gap narrowing in heavily doped silicon: A comparison of optical and electrical data.* Journal of Applied Physics, 1988. **63**(2): p. 425-429.
84. Oschlies, A., R.W. Godby, and R.J. Needs, *GW self-energy calculations of carrier-induced band-gap narrowing in n-type silicon.* Physical Review B, 1995. **51**(3): p. 1527.
85. Jellison, G.E., et al., *Optical Properties of Heavily Doped Silicon between 1.5 and 4.1 eV.* Physical Review Letters, 1981. **46**(21): p. 1414.
86. Shockley, W. and J. Bardeen, *Energy Bands and Mobilities in Monatomic Semiconductors.* Physical Review, 1950. **77**(3): p. 407.
87. Fan, H.Y., *Temperature Dependence of the Energy Gap in Monatomic Semiconductors.* Physical Review, 1950. **78**(6): p. 808.
88. Bludau, W., A. Onton, and W. Heinke, *Temperature dependence of the band gap of silicon.* Journal of Applied Physics, 1974. **45**(4): p. 1846-1848.
89. Lautenschlager, P., P.B. Allen, and M. Cardona, *Temperature dependence of band gaps in Si and Ge.* Physical Review B, 1985. **31**(4): p. 2163.
90. Green, M.A., *Intrinsic concentration, effective densities of states, and effective mass in silicon.* Journal of Applied Physics, 1990. **67**(6): p. 2944-2954.
91. Varshni, Y.P., *Temperature dependence of the energy gap in semiconductors.* Physica, 1967. **34**(1): p. 149-154.
92. Cardona, M., *Renormalization of the Optical Response of Semiconductors by Electron–Phonon Interaction.* physica status solidi (a), 2001. **188**(4): p. 1209-1232.
93. Tao, K. and et al., *The temperature dependence of the interband critical points in silicon within a fractional-dimensional space approach.* Journal of Physics: Condensed Matter, 2004. **16**(18): p. 3041.
94. Keyes, R.W., *Bonding and Antibonding Potentials in Group-IV Semiconductors.* Physical Review Letters, 1975. **34**(21): p. 1334.
95. Hensel, J.C. and G. Feher, *Cyclotron Resonance Experiments in Uniaxially Stressed Silicon: Valence Band Inverse Mass Parameters and Deformation Potentials.* Physical Review, 1963. **129**(3): p. 1041.
96. Horn, F.H., *Densitometric and Electrical Investigation of Boron in Silicon.* Physical Review, 1955. **97**(6): p. 1521.
97. Celloti, G. and e. al, *Lattice parameter study of silicon uniformly doped with boron and phosphorus.* J. Mat. Scien., 1974. **9**: p. 821.
98. Balkanski, M., R.F. Wallis, and E. Haro, *Anharmonic effects in light scattering due to optical phonons in silicon.* Physical Review B, 1983. **28**(4): p. 1928.
99. Huang, X., et al., *Temperature dependence of Raman scattering in Si crystals with heavy B and/or Ge doping.* Materials Science in Semiconductor Processing, 2006. **9**(1-3): p. 257-260.
100. Sui, Z. and I.P. Herman, *Effect of strain on phonons in Si, Ge, and Si/Ge heterostructures.* Physical Review B, 1993. **48**(24): p. 17938.
101. Cerdeira, F., et al., *Stress-Induced Shifts of First-Order Raman Frequencies of Diamond- and Zinc-Blende-Type Semiconductors.* Physical Review B, 1972. **5**(2): p. 580.

102. Cardona, M., *Semiconductors under Uniaxial Strain.* physica status solidi (b), 1996. **198**(1): p. 5-21.
103. Wright, O.B. and V.E. Gusev, *Acoustic generation in crystalline silicon with femtosecond optical pulses.* Applied Physics Letters, 1995. **66**(10): p. 1190-1192.
104. Figielski, T., *Photostriction Effect in Germanium.* physica status solidi (b), 1961. **1**(4): p. 306-316.
105. Gauster, W.B., *Electronic Dilation in Germanium and Silicon.* Physical Review, 1969. **187**(3): p. 1035.
106. Buschert, J.R. and R. Colella, *Photostriction effect in silicon observed by time-resolved x-ray diffraction.* Solid State Communications, 1991. **80**(6): p. 419-422.
107. Sutter, D.H., et al., *Semiconductor saturable-absorber mirror assisted Kerr-lens mode-locked Ti:sapphire laser producing pulses in the two-cycle regime.* Opt. Lett., 1999. **24**(9): p. 631-633.
108. Fraser, D.J. and M.H.R. Hutchinson, *A high intensity titanium-doped sapphire laser.* Journal of Modern Optics, 1996. **43**(5): p. 1055 - 1062.
109. *Crystal specification*. [cited; Available from: http://www.chinasupply.net/optical/product/crystals/TiSapphire.pdf.
110. Moulton, P.F., *Spectroscopic and laser characteristics of Ti:Al2O3.* J. Opt. Soc. Am. B, 1986. **3**(1): p. 125-133.
111. Fork, R.L., B.I. Greene, and C.V. Shank, *Generation of optical pulses shorter than 0.1 psec by colliding pulse mode locking.* Applied Physics Letters, 1981. **38**(9): p. 671-672.
112. Naganuma, K. and K. Mogi, *50-fs pulse generation directly from a colliding-pulse mode-locked Ti:sapphire laser using an antiresonant ring mirror.* Opt. Lett., 1991. **16**(10): p. 738-740.
113. Spielmann, C. and e. al., *Ultrabroadband femtosecond lasers.* IEEE J. Quantum Electron. , 1994. **30**: p. 1100.
114. Xu, L., et al., *High-power sub-10-fs Ti:sapphire oscillators.* Applied Physics B: Lasers and Optics, 1997. **65**(2): p. 151-159.
115. Cundiff, S.T., J. Ye, and J.L. Hall, *Optical frequency synthesis based on mode-locked lasers.* Review of Scientific Instruments, 2001. **72**(10): p. 3749-3771.
116. Zhou, J., et al., *Pulse evolution in a broad-bandwidth Ti:sapphire laser.* Opt. Lett., 1994. **19**(15): p. 1149-1151.
117. Kaertner, F.X. *Mode-locked Laser Theory*. 2006 [cited; Available from: http://www.physics.gatech.edu/frog/Mode-locking%20theory%20Kaertner.pdf.
118. Auston, D.H. and C.V. Shank, *Picosecond Ellipsometry of Transient Electron-Hole Plasmas in Germanium.* Physical Review Letters, 1974. **32**(20): p. 1120.
119. Misochko, O.V. and et al., *Coherent A 1 phonons in Te studied with tailored femtosecond pulses.* Journal of Physics: Condensed Matter, 2007. **19**(40): p. 406220.
120. Misochko, O.V., et al., *Effect of intense chirped pulses on the coherent phonon generation in Te.* Applied Physics Letters, 2007. **90**(7): p. 071901.
121. Suzaki, Y. and A. Tachibana, *Measurement of the μm sized radius of Gaussian laser beam using the scanning knife-edge.* Appl. Opt., 1975. **14**(12): p. 2809-2810.
122. Huber, R., et al., *How many-particle interactions develop after ultrafast excitation of an electron-hole plasma.* Nature, 2001. **414**(6861): p. 286-289.
123. Fano, U., *Effects of Configuration Interaction on Intensities and Phase Shifts.* Physical Review, 1961. **124**(6): p. 1866.

124. Cerdeira, F., T.A. Fjeldly, and M. Cardona, *Interaction between electronic and vibronic Raman scattering in heavily doped silicon.* Solid State Communications, 1973. **13**(3): p. 325-328.
125. Misochko, O.V. and et al., *Fano interference for large-amplitude coherent phonons in bismuth.* Journal of Physics: Condensed Matter, 2007. **19**(15): p. 156227.
126. Muneaki, H. and K. Masahiro, *Interaction of coherent phonons with defects and elementary excitations.* Journal of Physics: Condensed Matter. **22**(7): p. 073201.
127. Hase, M., et al., *The birth of a quasiparticle in silicon observed in time-frequency space.* Nature, 2003. **426**(6962): p. 51-54.
128. Othonos, A. and C. Christofides, *Ultrafast dynamics in phosphorus-implanted silicon wafers: The effects of annealing.* Physical Review B, 2002. **66**(8): p. 085206.
129. Johnston, M.B., et al., *Simulation of terahertz generation at semiconductor surfaces.* Physical Review B, 2002. **65**(16): p. 165301.
130. Peter, N.S., I.G. Benjamin, and C. Shun Lien, *Short terahertz pulses from semiconductor surfaces: The importance of bulk difference-frequency mixing.* Applied Physics Letters, 1993. **63**(25): p. 3482-3484.
131. Khurgin, J.B., *Optical rectification and teraherz emission in semiconductors excited above the band gap.* J. Opt. Soc. Am. B, 1994. **11**: p. 2492–2501.
132. Tom, H.W.K., T.F. Heinz, and Y.R. Shen, *Second-Harmonic Reflection from Silicon Surfaces and Its Relation to Structural Symmetry.* Physical Review Letters, 1983. **51**(21): p. 1983.
133. Pfeifer, T., et al., *Generation mechanism for coherent LO phonons in surface-space-charge fields of III-V-compounds.* Applied Physics A: Materials Science & Processing, 1992. **55**(5): p. 482-488.
134. Chuang, S.L., et al., *Optical rectification at semiconductor surfaces.* Physical Review Letters, 1992. **68**(1): p. 102.
135. Bass, M., et al., *Optical Rectification.* Physical Review Letters, 1962. **9**(11): p. 446.
136. Khurgin, J.B., *Optical rectification and terahertz emission in semiconductors excited above the band gap.* J. Opt. Soc. Am. B, 1994. **11**(12): p. 2492-2501.
137. VallenSysteme. [cited; Available from: http://www.vallen.de/wavelet/.
138. Kanehisa, M.A., R.F. Wallis, and M. Balkanski, *Interband electronic Raman scattering in p-silicon.* Physical Review B, 1982. **25**(12): p. 7619.
139. Chandrasekhar, M., J.B. Renucci, and M. Cardona, *Effects of interband excitations on Raman phonons in heavily doped n-Si.* Physical Review B, 1978. **17**(4): p. 1623.
140. Dumitrica, T., et al., *Response of Si and InSb to ultrafast laser pulses.* physica status solidi (b), 2004. **241**(10): p. 2331-2342.
141. Keyes, R.W., *The Electronic Contribution to the Elastic Properties of Germanium.* IBM Journal of Research and Development, 1961. **5**(4): p. 266-278.
142. Hart, T.R., R.L. Aggarwal, and B. Lax, *Temperature Dependence of Raman Scattering in Silicon.* Physical Review B, 1970. **1**(2): p. 638.
143. Gu, M., et al., *Temperature dependence of the elastic and vibronic behavior of Si, Ge, and diamond crystals.* Journal of Applied Physics, 2007. **102**(8): p. 083524.
144. Ishioka, K., et al., *Ultrafast carrier and phonon dynamics in ion-irradiated graphite.* Applied Physics Letters, 2001. **78**(25): p. 3965-3967.
145. Ishioka, K., et al., *Ultrafast electron-phonon decoupling in graphite.* Physical Review B, 2008. **77**(12): p. 121402.

146. Muneaki, H., et al., *Dephasing of coherent phonons by lattice defects in bismuth films.* Applied Physics Letters, 2000. **76**(10): p. 1258-1260.
147. Ishioka, K., et al., *Coherent optical phonons in diamond.* Applied Physics Letters, 2006. **89**(23): p. 231916.
148. Tsen, K.T., *Ultrafast Physical Processes in Semiconductors.* Semiconductors and Semimetals. Vol. 67. 2001: Academic Press.
149. Hase, M., et al., *Dephasing of coherent THz phonons in bismuth studied by femtosecond pump-probe technique.* Applied Surface Science, 2002. **197-198**: p. 710-714.
150. Jouanne, M., et al., *Electron-phonon coupling in highly doped n type silicon.* Solid State Communications, 1975. **16**(8): p. 1047-1049.
151. Cardona, M., F. Cerdeira, and T.A. Fjeldly, *Sign of the Raman tensor of diamond and zinc-blende-type semiconductors.* Physical Review B, 1974. **10**(8): p. 3433.
152. Cheng, T.K., et al., *Mechanism for displacive excitation of coherent phonons in Sb, Bi, Te, and Ti<inf>2</inf>O<inf>3</inf>.* Applied Physics Letters, 1991. **59**(16): p. 1923-1925.
153. Aspnes, D.E. and A.A. Studna, *Dielectric functions and optical parameters of Si, Ge, GaP, GaAs, GaSb, InP, InAs, and InSb from 1.5 to 6.0 eV.* Physical Review B, 1983. **27**(2): p. 985.
154. Herzinger, C.M., et al., *Ellipsometric determination of optical constants for silicon and thermally grown silicon dioxide via a multi-sample, multi-wavelength, multi-angle investigation.* Journal of Applied Physics, 1998. **83**(6): p. 3323-3336.
155. Patrin, A. and M. Tarasik, *Optical-absorption spectrum of silicon containing internal elastic stresses.* Journal of Applied Spectroscopy, 1998. **65**(4): p. 598-603.
156. Yan, Y.-X., J.E.B. Gamble, and K.A. Nelson, *Impulsive stimulated scattering: General importance in femtosecond laser pulse interactions with matter, and spectroscopic applications.* The Journal of Chemical Physics, 1985. **83**(11): p. 5391-5399.
157. Pfeifer, T., et al., *Generation and detection of coherent optical phonons in germanium.* Physical Review Letters, 1992. **69**(22): p. 3248.
158. Sjodin, T., H. Petek, and H.-L. Dai, *Ultrafast Carrier Dynamics in Silicon: A Two-Color Transient Reflection Grating Study on a (111) Surface.* Physical Review Letters, 1998. **81**(25): p. 5664.
159. Young, J.F. and H.M. van Driel, *Ambipolar diffusion of high-density electrons and holes in Ge, Si, and GaAs: Many-body effects.* Physical Review B, 1982. **26**(4): p. 2147.
160. Sabbah, A.J. and D.M. Riffe, *Measurement of silicon surface recombination velocity using ultrafast pump--probe reflectivity in the near infrared.* Journal of Applied Physics, 2000. **88**(11): p. 6954-6956.
161. Li, C.M., et al., *Measuring photocarrier diffusivity near a Si(111) surface by reflective two-color transient grating scattering.* Applied Physics Letters, 1995. **66**(25): p. 3501-3503.
162. Bergner, H. and V. Bruckner, *Dependence of the Ambipolar Diffusion in Silicon on the Carrier Density.* physica status solidi (a), 1983. **79**(1): p. K85-K88.
163. Rosling, M., et al., *The ambipolar diffusion coefficient in silicon: Dependence on excess-carrier concentration and temperature.* Journal of Applied Physics, 1994. **76**(5): p. 2855-2859.
164. Algarte, A.C.S., *Effect of ambipolar diffusion on the hot-carrier relaxation in semiconductors.* Physical Review B, 1991. **43**(3): p. 2408.

165. van Driel, H.M. and J.F. Young, *Many-body effects and the diffusion of high-density electrons and holes in semiconductors.* Journal of Physics C: Solid State Physics, 1982. **15**(3): p. L31.
166. Harb, M., et al., *Carrier Relaxation and Lattice Heating Dynamics in Silicon Revealed by Femtosecond Electron Diffractionâ€* The Journal of Physical Chemistry B, 2006. **110**(50): p. 25308-25313.
167. Chen, J.K., D.Y. Tzou, and J.E. Beraun, *A semiclassical two-temperature model for ultrafast laser heating.* International Journal of Heat and Mass Transfer, 2006. **49**(1-2): p. 307-316.
168. Korfiatis, D.P. and et al., *Conditions for femtosecond laser melting of silicon.* Journal of Physics D: Applied Physics, 2007. **40**(21): p. 6803.
169. Teitel, S.L. and J.W. Wilkins, *Ballistic transport and velocity overshoot in semiconductors. I - Uniform field effects.* IEEE Transactions on Electron Devices, 1983. **ED-30**: p. 150-153.
170. Gerlach, W., H. Schlangenotto, and H. Maeder, *On the radiative recombination rate in silicon.* physica status solidi (a), 1972. **13**(1): p. 277-283.
171. Rowe, M.W., et al., *Picosecond photoelectron spectroscopy of excited states at Si(111) $\sqrt{3}\times\sqrt{3}R30^{o}$-B, Si(111)7×7, Si(100)2×1, and laser-annealed Si(111)1×1 surfaces.* Physical Review B, 1993. **47**(4): p. 2048.
172. Paul, W. and D.M. Warschauer, *Optical properties of semiconductors under hydrostatic pressure--II. Silicon.* Journal of Physics and Chemistry of Solids, 1958. **5**(1-2): p. 102-106.
173. Misochko, O., *Coherent phonons and their properties.* Journal of Experimental and Theoretical Physics, 2001. **92(**2): p. 246-259.
174. Ishioka, K. and O.V. Misochko, *Coherent Lattice Oscillations in Solids and Their Optical Control*, in *Progress in Ultrafast Intense Laser Science Volume V*. 2009, Springer Berlin Heidelberg. p. 23-46.
175. Aspnes, D.E. and M. Cardona, *Strain dependence of effective masses in tetrahedral semiconductors.* Physical Review B, 1978. **17**(2): p. 726.
176. Bardeen, J. and W. Shockley, *Deformation Potentials and Mobilities in Non-Polar Crystals.* Physical Review, 1950. **80**(1): p. 72.
177. Hull, R., *Properties of crystalline Silicon*. 1999, London, UK: INSPEC.
178. Varshni, Y.P., *Temperature Dependence of the Elastic Constants.* Physical Review B, 1970. **2**(10): p. 3952.
179. Brantley, W.A., *Calculated elastic constants for stress problems associated with semiconductor devices.* Journal of Applied Physics, 1973. **44**(1): p. 534-535.
180. Ayers, J.E., *Heteroepitaxy of Semiconductors:Theory, Growth, and Characterization*. 2007: Tylor and Francis Group, LLC.
181. Hensel, J.C., H. Hasegawa, and M. Nakayama, *Cyclotron Resonance in Uniaxially Stressed Silicon. II. Nature of the Covalent Bond.* Physical Review, 1965. **138**(1A): p. A225.
182. Madelung, O. and e. al., *Landolt-Bornstein Numerical Data and Functional Relationships in Science and Technology*. 1982: Springer Berlin.
183. Kasper, E. and D.J. Paul, *Silicon quantum integrated circuits. Silicon-germanium heterostructure devices: basics and realisations*. Nanoscience and Technology. 2005: Springer.

184. Laude, L.D., F.H. Pollak, and M. Cardona, *Effects of Uniaxial Stress on the Indirect Exciton Spectrum of Silicon.* Physical Review B, 1971. **3**(8): p. 2623.
185. Van de Walle, C.G. and R.M. Martin, *Theoretical calculations of heterojunction discontinuities in the Si/Ge system.* Physical Review B, 1986. **34**(8): p. 5621.
186. Tserbak, C. and e. al., *Unified approach to the electronic structure of strained Si/Ge superlattices.* Phys. Rev. B, 1993. **47**: p. 7104–7124.
187. Tserbak, C. and G. Theodorou, *Energy band structure and linear optical properties of Si and Ge strained along the [111] and [110] directions.* Physical Review B, 1995. **52**(16): p. 12232.
188. Etchegoin, P., J. Kircher, and M. Cardona, *Elasto-optical constants of Si.* Physical Review B, 1993. **47**(16): p. 10292.
189. Kondo, K. and A. Moritani, *Symmetry analysis and uniaxial-stress effect on the low-field electroreflectance of Si from 3.0 to 4.0 eV.* Physical Review B, 1976. **14**(4): p. 1577.
190. Theodorou, G. and G. Tsegas, *Piezooptical Properties of Si.* physica status solidi (b), 1998. **207**(2): p. 541-556.